



**EVALUATION OF NANOCOMPOSITES FOR SHIELDING
ELECTROMAGNETIC INTERFERENCE**

THESIS

Kenneth Y. Chong, Lieutenant Commander, USN

AFIT/GAE/ENY/11-S01

**DEPARTMENT OF THE AIR FORCE
AIR UNIVERSITY**

AIR FORCE INSTITUTE OF TECHNOLOGY

Wright-Patterson Air Force Base, Ohio

APPROVED FOR PUBLIC RELEASE; DISTRIBUTION UNLIMITED

The views expressed in this thesis are those of the author and do not reflect the official policy or position of the United States Air Force, Department of Defense, or the United States Government. This material is declared a work of the U.S. Government and is not subject to copyright protection in the United States.

AFIT/GAE/ENY/11-S01

**EVALUATION OF NANOCOMPOSITES FOR SHIELDING
ELECTROMAGNETIC INTERFERENCE**

THESIS

Presented to the Faculty

Department of Aeronautics and Astronautics

Graduate School of Engineering and Management

Air Force Institute of Technology

Air University

Air Education and Training Command

In Partial Fulfillment of the Requirements for the
Degree of Master of Science in Aeronautical Engineering

Kenneth Y. Chong, BS

Lieutenant Commander, USN

September 2011

APPROVED FOR PUBLIC RELEASE; DISTRIBUTION UNLIMITED.

**EVALUATION OF NANOCOMPOSITES FOR SHIELDING
ELECTROMAGNETIC INTERFERENCE**

Kenneth Y. Chong, BS
Lieutenant Commander, USN

Approved:

Dr. Shankar Mall (Chairman)

Date

Dr. Som Soni (Member)

Date

Dr. Vinod Jain (Member)

Date

Space vehicles encounter an unpleasant environment in space with dangers such as extreme temperatures, solar radiation, out-gassing, debris, and micrometeoroids. The cost of launching systems into space is extremely high and stands between \$10,000/lb - \$12,000/lb. As a result, there is an emergent requirement of weight/cost reduction for future space systems that still comply with the rigorous specifications to properly function in space. This study focuses on the potential utilization of nanocomposite materials for satellite structures as a solution to reduce system weight while retaining the desired survivability against electromagnetic interference (EMI).

Four, eight-ply nanocomposite panels were fabricated from Cycom 5575-2 glass with multi-walled carbon nanotube (MWNT) plies. The control panel had eight plies of glass fabric reinforced composite only and will be referred to as *8G*. This enabled the comparison of all properties with and without carbon nanotubes (CNTs). The other three panels had differences in the placement of layers containing CNTs: the first one had four CNT plies on one half with four plies of glass on the opposite half and will be referred to as *4G/4CNT*, the second one had two plies of CNT on the exterior of each side with four plies of glass in the middle and will be referred to as *2CNT/4G/2CNT*, and the third one had alternating CNT/glass fabric plies across the thickness and will be referred to as *(G/CNT)₄*.

These four configurations were measured for their respective EMI shielding properties after experiencing monotonic tension load, thermal cycling, and a combination

of thermal cycling followed by monotonic tension load. EMI measurements were taken in terms of decibels (dB) before and after each thermal cycle or monotonic tension test. Tension tests involved increasing the load incrementally until ultimate failure. Thermal cycling was conducted with a cycle having a total soak time of 20 seconds. The first 10 seconds were at +60 °C and the last 10 seconds were at -60 °C. The total number of thermal cycles was 17,500.

Multiple EMI shielding effectiveness (SE) values were measured on metallic materials for comparison. The average EMI SE of type 2024 aluminum and type 7075 aluminum for the frequency range of 2 GHz – 18 GHz were 112.6 dB and 113.46 dB, respectively. In a previous study, EMI SE values for four distinct nanocomposites containing nickel nanostrands (NS) were measured and their averaged attenuation prior to testing are as follows: Control 1 – 58 dB, Exterior 1 – 73 dB, Exterior 2 – 66 dB, Interlaminar 1 – 64 dB, and Midplane 1 – 55 dB. The stacking sequence of the 8-ply, NS nanocomposites was a quasi-isotropic lay-up of $[0/90/\pm 45]_s$. The Control specimen contained no NS plies, the Exterior specimens had one NS ply on the exterior of the 0° ply for a total of two NS plies, Interlaminar had one NS ply between the 0° and 90 plies and one NS ply between the 45° and -45° plies for a total of four NS plies, and the Midplane specimen had one NS ply directly in the midplane between the -45° and -45° plies. The EMI SE values for all four MWNT nanocomposite configurations were measured prior to testing in the same frequency range and the averaged numbers are as follows: 8G – 0.33 dB, 4G/4CNT – 87.5 dB, 2CNT/4G/2CNT – 87.5 dB, and (G/CNT)₄ – 71.76 dB. The EMI SE performance of the nanocomposites containing MWNTs

exceeded those comprised of NS. This study found that the EMI SE properties for all four MWNT panels experienced varying degrees of reduction in EMI SE after thermal cycling and/or monotonic tension test until fracture. The final EMI SE values for all four MWNT nanocomposite configurations were measured from 8.2 GHz – 12.4 GHz and were taken after testing was completed and the averaged numbers are as follows: 8G – 1.01 dB, 4G/4CNT – 60.98 dB, 2CNT/4G/2CNT – 83.49 dB, and (G/CNT)₄ – 68.45 dB. Please note the difference in frequency ranges between the EMI SE values prior to tests (2 GHz – 18 GHz) and during tests (8.2 GHz – 12.4 GHz). The MWNT nanocomposite lay-up providing the best performance against EMI was the 2CNT/4G/2CNT configuration, which is in agreement with and comparable to the NS Exterior configuration with respect to placement of the nanofibers.

The failure mechanisms were consistent for each MWNT nanocomposite configuration. This occurred through the initial formation of transverse fiber matrix cracks that triggered the delamination of one or more CNT plies, which then led to the progression of transverse strand debonding. Increasing stress caused additional fill strand separation and delamination of multiple plies resulting in ultimate failure, and for all configurations the multi-walled CNTs remained intact.

Acknowledgements

I would like to thank several people who have provided tremendous support while conducting my research for this thesis. Dr. Shankar Mall for cheerfully directing my efforts and offering thought provoking questions to enhance my research. The Air Force Institute of Technology laboratory technicians, Dr. Volodymyr Sabelkin, and Air Force Research Lab personnel who continuously afforded me with the assistance and expertise needed in the laboratories. My beloved wife for having lovingly endured and sacrificed much in order to grant me the time required to complete my thesis. Lastly, to the one who breathes life into me and gives every good gift, Jesus Christ.

Kenneth Y. Chong, Lieutenant Commander, USN

Table of Contents

Page

Abstract	iv
Acknowledgements	vii
Table of Contents	viii
List of Figures	x
List of Tables	xiii
List of Symbols	xiv
List of Abbreviations	xv
I. Introduction	1
1.1 Current Spaceborne Systems	2
1.2 Present Spacecraft Materials.....	4
1.3 Evolution of Composites	5
1.4 Nanocomposites	7
1.5 Thesis Objective	8
1.6 Summary	9
II. Literary Review	10
2.1 Space Environment	10
2.2 Ionizing Radiation and Electromagnetic Interference	12
2.3 EMI Shielding Effectiveness of Nanofibers	14
2.4 Summary	18
III. Methodology	20
3.1 Introduction.....	20
3.2 Specimen Preparation	20
3.3 Focused Beam Tunnel Test Equipment and Procedures	23
3.4 Monotonic Tension Test Equipment and Procedures	25
3.5 Thermal Cycling Test Equipment and Procedures	28
3.6 EMI Test Equipment and Procedures	33
3.7 Test Plan Summary	36

3.8 Error Analysis	37
IV. Analysis and Results	40
4.1 Introduction.....	40
4.2 Focused Beam.....	42
4.3 Monotonic Tension – Group 1	43
4.4 Thermal Cycling followed by Monotonic Tension – Group 2	48
4.5 Monotonic Tension – Group 3	57
4.5 Failure Mechanisms	62
4.6 Glass Feature.....	75
V. Conclusions and Recommendations	78
5.1 Summary	78
5.2 Conclusions.....	79
5.2 Recommendations for Future Work	80
Appendix A. EMI Shielding Theory.....	82
Appendix B. Astroquartz II Glass Properties	84
Bibliography	85
Vita.....	87

List of Figures

	Page
Figure 1. Spaceborne missile surveillance.....	4
Figure 2. 8-ply stacking sequence.....	6
Figure 3. Single-wall carbon nanotube (SWNT)	8
Figure 4. Multi-wall carbon nanotube (MWNT)	8
Figure 5. Computer generated image from NASA on space debris	12
Figure 6. Log DC conductivity (σ) vs mass fraction (p) of SWNTs – long composites measured at room temperature. Inset: log – log plot for σ vs ((p-pc)/pc) for the same composites [Ning et al].....	15
Figure 7. Impact of wall integrity and aspect ratio on the EMI shielding effectiveness of the composites containing 10 wt % SWNTs	15
Figure 8. SEM image of the cross of section SWNTs – composites with 10 wt % loading.....	16
Figure 9. 8-Ply stacking sequence of nanocomposites.	21
Figure 10. Test specimen	22
Figure 11. Test specimen with glass/epoxy tabs.....	23
Figure 12. Focused beam tunnel	26
Figure 13. Material Test System machine	26
Figure 14. MTS machine with specimen inserted	27
Figure 15. Thermal cycles from +60 °C to -60 °C.....	29
Figure 16. ThermoJet test device	30
Figure 17. Test specimens inserted into foam spacers.....	31
Figure 18. Test specimens attached to DUT thermocouple - ThermoJet test device	31
Figure 19. ThermoJet test device control panel	32
Figure 20. Agilent Technologies E8362B PNA Series Network Analyzer	33
Figure 21. Test specimen divided into three sections for EMI measurements	35
Figure 22. Test specimen secured horizontally between Network Analyzer adapters	35
Figure 23. Simplified diagram of grounding the sample	38
Figure 24. Final view of fully prepared test sample	38

Figure 25. Cross-sectional view of four designs: top - 8G, left - 4G/4CNT, right - (G/CNT) ₄ , bottom - 2CNT/4G/2CNT	41
Figure 26. Focused beam test results	43
Figure 27. EMI attenuation data for Group 1	45
Figure 28. EMI attenuation data normalized to initial conditions for Group 1	47
Figure 29. EMI attenuation versus thermal cycles for Group 2.....	49
Figure 30. EMI attenuation versus thermal cycles normalized to initial conditions for Group 2.....	50
Figure 31. Fracture values for Group 1 and Group 2.....	52
Figure 32. EMI attenuation data for Group 2	54
Figure 33. EMI attenuation data normalized to initial conditions for Group 2	56
Figure 34. Fracture values for Groups 1 - 3.....	58
Figure 35. EMI attenuation data for Group 3	59
Figure 36. EMI attenuation data normalized to initial conditions for Group 3	61
Figure 37. Specimens after fracture: top – Group 1, middle – Group 2, bottom – Group 3	63
Figure 38. Fractured 8G specimen: thickness view at 100x	64
Figure 39. Fractured 8G specimen: thickness view at 12x	64
Figure 40. SEM image of 8G: transverse matrix crack and delamination.....	65
Figure 41. Fractured 4G/4CNT specimen: thickness view at 100x	66
Figure 42. Fractured 4G/4CNT specimen: thickness view at 12x.....	67
Figure 43. Principal laminate coordinate system.....	67
Figure 44. SEM image of 4G/4CNT: transverse matrix crack and delamination.....	68
Figure 45. SEM image of 4G/4CNT: intact CNT plies at fracture point.....	68
Figure 46. Fractured 2CNT/4G/2CNT specimen: thickness view at 100x.....	69
Figure 47. Fractured 2CNT/4G/2CNT specimen: thickness view at 12x.....	70
Figure 48. SEM image of 2CNT/4G/2CNT: transverse matrix crack and delamination.....	71
Figure 49. SEM image of 2CNT/4G/2CNT: intact CNT plies at fracture point.....	71
Figure 50. Fractured (G/CNT) ₄ specimen: thickness view at 100x	72
Figure 51. Fractured (G/CNT) ₄ specimen: thickness view at 12x	73
Figure 52. SEM image of (G/CNT) ₄ : transverse matrix crack and delamination.....	74
Figure 53. SEM image of (G/CNT) ₄ : intact CNT plies at fracture point.....	74

Figure 54. Vertical features of intact 8G at 60x.....	75
Figure 55. SEM image of intact 8G features at 100x	76
Figure 56. SEM image of intact 8G features at 300x: boxed region from Figure 57.....	76
Figure 57. SEM image of intact 8G features at 600x: boxed region from Figure 58.....	77

List of Tables

	Page
Table 1. ThermoJet thermal cycles	28
Table 2. Network Analyzer calibration procedure	34
Table 3. Test Matrix.....	37
Table 4. Group 1 - Stress with corresponding EMI attenuation	46
Table 5. Group 2 - Thermal cycles with corresponding EMI attenuation	51
Table 6. Fracture values for Group 1 and Group 2	52
Table 7. Group 2 - % UTS with corresponding EMI attenuation	55
Table 8. Fracture values for Groups 1 - 3	57
Table 9. Group 3 - % UTS with corresponding EMI attenuation	60

List of Symbols

Symbol

σ	carbon nanotube direct current conductivity (S/cm)
p	mass fraction
p_c	percolation threshold

List of Abbreviations

Abbreviation

ACM	Advanced Composite Material
AFIT	Air Force Institute of Technology
AFRL	Air Force Research Laboratory
AFRL/RX	Air Force Research Laboratory Manufacturing and Materials Directorate
CNT	Carbon Nanotube
DC	Direct current
DUT	Device under test
EMI	Electromagnetic Interference
ESD	Electrostatic Discharge
FAA	Federal Aviation Administration
FRP	Fiberglass Reinforced Plastic
GCR	Galactic Cosmic Radiation
GSM	Grams per square meter
LEO	Low Earth Orbit
MPT	MultiPurpose TestWare
MTS	Material Test System
MWNT	Multi-wall Carbon Nanotube
NASA	National Aeronautics and Space Administration
NCTI	Nanocomp Technologies, Inc.
NORAD	North American Aerospace Defense Command
NS	Nickel nanostrand
RET	Reactive Ethylene Terpolymer
SE	Shielding Effectiveness
SEM	Scanning Electron Microscope
SPE	Solar Particle Event
SWNT	Single-wall Carbon Nanotube
UTS	Ultimate Tensile Strength

EVALUATION OF NANOCOMPOSITES FOR SHIELDING ELECTROMAGNETIC INTERFERENCE

Introduction

The United States military and the field of materials science and engineering have great interest in the multifunctionality of nanocomposites. Nanocomposites demonstrate high specific strength, low weight, and high conductivity yielding near limitless applications of this technology. They possess improved mechanical properties over traditional materials used within the aerospace industry such as aluminum and may offer solutions to longstanding design and performance shortfalls. The advantages and characteristics of nanocomposites are still being uncovered and require further examination in order to properly design and develop nanocomposite structures. One area considered for nanocomposite application is spaceborne systems.

Space vehicles are subjected to one of the worst environments known to mankind. Copious hazards continuously threaten a spacecraft's condition and capacity to fulfill its intended design. Aluminum and composite structures such as Kevlar/epoxy and graphite/epoxy have satisfactorily met the design and manufacturing requirements of past and current space vehicles. Nevertheless, there is an increasing and overwhelming demand for lighter, stronger, and more durable materials. Weight reduction and the extension of a system's life span by boosting its ability to withstand such a cruel environment serve to deliver an exceedingly desirable vehicle. Nanocomposites possess the ability to meet and exceed the demand for a more robust material to operate in space.

Nanocomposites are a multiphase material where at least one of the constituent phases has one dimension less than 100 nm. Numerous challenges impede the full utilization of nanocomposites which are controlling the distribution in size and dispersion of the nanosize constituents, tailoring and understanding the role of interfaces between structurally or chemically dissimilar phases on bulk properties, and large scale and controlled processing of multiple nanomaterials [3,IX]. However, the exceptional characteristics of nanocomposites have compelled an ongoing surge of intensive research in order to expedite the ability to suitably employ such a revolutionary material. Specifically, nanocomposite research and development has expanded due to their favorable results for use in combating the damaging effects of electromagnetic interference (EMI) on spacecraft.

This chapter will define performance requirements of current space-based systems and the materials used to construct them. In addition, it will deliver a brief history of the early research and development of traditional composites that led to the development of nanocomposites. A comparison between current spacecraft materials and nanocomposites is made with the advantages of the latter receiving attention for its enhanced capacity to defend against EMI. The final section in this chapter will include the outline and objective of this work.

1.1 Current Spaceborne Systems

Throughout history military campaigns sought this critical, tangible advantage: obtain and preserve elevated terrain over your foe. The ability to perceive enemy activity

from afar in order to perfect strategy and tactics and promptly react to enemy movement has and always shall be a vital factor for ensuring a swift and decisive victory. Space offers this advantage and stands alone in delivering the ultimate vantage point to monitor global activity.

Current spaceborne systems are the result of an evolution of early space strategy/doctrine and science and technology initiatives that sought to exploit the field of view from space. In 1991, U.S. Space Command identified several high-priority space systems needed to implement military space strategy: Space-based wide area surveillance, military satellite communications, and reliable spacecraft that had widespread applications [10,141-151]. Likewise, science and technology ventures stimulated an explosion of growth for spacecraft due to the data collection on sea-surface winds, ocean topography, land topography, global temperatures, wave heights/lengths/directions, atmospheric conditions, and sea ice features [8].

All spacecraft materials must withstand high mechanical stresses, cryogenic temperatures, have thermal stability, resist high strains, repel brittleness at extremely low temperatures, and have the lightest weight possible [12,178]. Current materials in use to satisfy these demanding requirements are ceramics, metals, polymers, and composites. The necessity to reduce weight in order to decrease launch costs is a considerable factor for the large use of honeycomb-structured panels of aluminum alloy [17,26]. Although proven and reliable, remarkable efforts have been taken to search for a lighter, tougher, and more conductive item. Nanocomposites present a viable answer to the pursuit of such a material.



Figure 1. Spaceborne missile surveillance

1.2 Present Spacecraft Materials

Current materials employed to manufacture spacecraft include, but are not limited to, aluminum alloys, polymer matrix composites, and ceramics. Polymer matrix composites have successfully attained the goal of reducing the overall weight of space vehicles, but on their own are incapable of contributing adequate protection against an unfriendly space environment. Ionizing radiation is abundant in space and directly results in the buildup of electrical charge on the surface of spacecraft. This resultant charge leads to uninhibited electrostatic discharge (ESD) and electromagnetic interference (EMI), which causes immense damage to spacecraft structures and

performance. Composite materials introduce a critical capability shortfall because they do not guard against ESD and EMI.

In order to achieve a satisfactory level of defense against EMI, existing composites require a supplementary application of conductive materials during the manufacturing process. Techniques such as conductive elastomers, metal EMI gasketing, EMI cable shielding, conductive coatings and adhesives, shielding laminates and foil tapes, and shielded vents and windows are employed to safeguard against EMI [15]. However, these techniques result in considerable increases to cost, manufacturing timelines, and weight. Thus, new materials and techniques are persistently sought after and researched in order to reduce structural weight while retaining the ability to shield against EMI. Nanocomposites have risen as an exhilarating solution to this diabolical predicament.

1.3 Evolution of Composites

Composite materials refer to materials having strong fibers – continuous or non-continuous – surrounded by a weaker matrix material. The matrix serves to distribute the fibers and also to transmit the load to the fibers [6,3]. Early composite materials were heterogeneous such as Egyptian bricks made from straw and mud circa 1500 BC. In 1938, Owens-Corning created fiberglass, which led to the development of fiberglass reinforced plastics (FRP). From this event a revolution of synthetic materials arose to the eventual birth of advanced composites.

Advanced composite materials (ACM) can be best characterized as materials that are governed primarily by the properties of the reinforcing fibers, which have high

strength and high stiffness characteristics and occupy a high volume fraction of the composite. Due to their low density, unusually high axial or longitudinal specific strength and stiffness values are obtained [17,1]. Examples of fibers used are carbon, aramid, and glass and they typically have widths in the order of microns. ACMs consist of several laminae or plies to generate a single laminate. One can tailor the characteristics of a laminate by choosing the type of fiber, varying the orientation of the fiber, modifying the ply sequence, and altering the matrix resin. Figure 2 reveals an 8-ply stacking sequence with varying fiber orientation. The matrix resin is the continuous phase in which the reinforcing fiber is contained, provides uniform load distribution to the fiber, and safeguards the composite surface against abrasion or environmental corrosion [17,9].

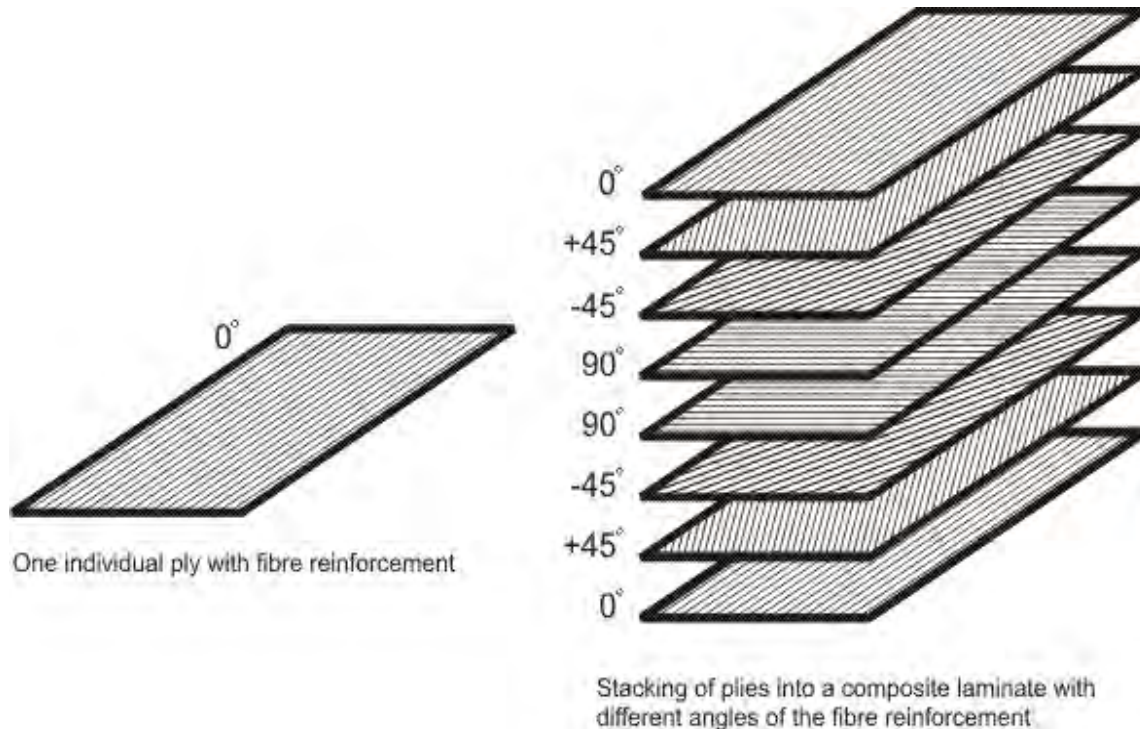


Figure 2. 8-ply stacking sequence

1.4 Nanocomposites

Nanocomposites differ from conventional composites (e.g., reinforced concrete) by having a constituent of dimension less than 100 nm, very low fiber volume fraction, and enhanced thermal, mechanical, optical, electrical, and electrochemical properties. Fiber volume fraction is defined as the ratio of fiber volume to total volume.

Nanomaterials can be metallic, polymeric, ceramic, electronic, or composite, and the most common materials used as matrix are polymers (e.g. epoxy, nylon, polyepoxide, polyetherimide), ceramics (e.g. alumina, glass, porcelain), and metals (e.g. iron, titanium, magnesium) [8,276]. Due to their noble material properties, nanocomposites have incredible potential for inexhaustible application into diverse arenas. This has fashioned considerable research into the characterization of nanocomposites because of the demand to publish and comprehend its full characteristics.

Previous studies have been conducted on the use of carbon nanotubes (CNT) and nickel nanostrands (NS) for various applications. Of particular significance, however, is the manner in which nanocomposites have demonstrated an exceptional capacity to defend spacecraft against EMI. A mentionable item is that no known research has been conducted on the EMI SE of nanocomposites created with Cycom 5575-2 glass and MWNTs, which are the focus of this study. The ceaseless threat of EMI damage to spacecraft along with the manufacturing barriers associated with providing sufficient EMI shielding for structural components has generated a plethora of research into new materials. Nanocomposites possess features such as high strength, high conductivity, low weight, and outstanding EMI shielding properties rendering them a highly desirable material for use as in spacecraft.

1.5 Thesis Objective

The objective of this thesis was to characterize the EMI shielding effectiveness of CNTs and CNT composites undergoing monotonic tension loading and/or thermal cycling. The nanocomposites tested were comprised of plies having multi-walled CNTs (MWNT) and glass fabric plies arranged in four distinctive configurations. For comparison, Figure 3 illustrates a single-wall CNT (SWNT) and Figure 4 depicts a MWNT. The testing process began by preparing each specimen for monotonic tension tests and thermal cycling. Each specimen was subjected to increasing monotonic tension loads until ultimate failure and a total of 17,500 thermal cycles were performed.

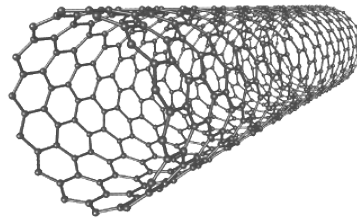


Figure 3. Single-wall carbon nanotube (SWNT)

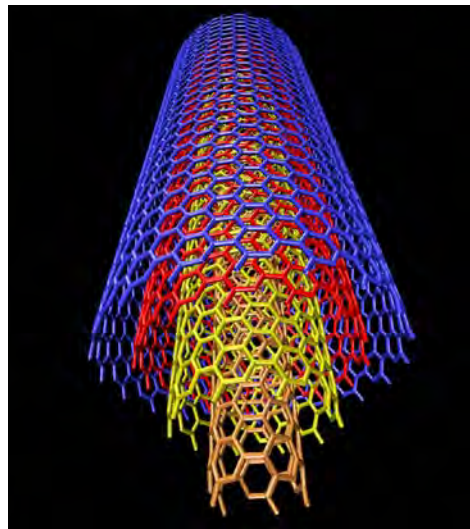


Figure 4. Multi-wall carbon nanotube (MWNT)

1.6 Summary

This thesis presentation is divided into five chapters. Chapter I covers the background of space-based systems along with the present materials used to manufacture space vehicles. The evolution of composites and the unique features of nanocomposites are discussed along with the growing need to further examine their characteristics of EMI SE. Chapter II presents a literature review of the space environment, the four nanocomposite panels tested in this thesis, and how radiation and EMI impact material properties. Chapter III describes all test procedures and equipment. Chapter IV then explicates on all the testing performed by thoroughly analyzing the results. Lastly, chapter V presents the conclusions of this thesis.

Literary Review

The purpose of this chapter is to describe how the space environment adversely impacts spacecraft, provide a report of the four panels tested along with similar work, and explain the behavior of electromagnetic interference (EMI). The chapter will first present the performance requirements of spacecraft to overcome the hazards of space. It will then present the physics of EMI and techniques to mitigate its effects. Lastly, it will state the EMI shielding effectiveness (SE) of nanofibers according to this study and previous studies.

2.1 Space Environment

Space poses numerous threats to spacecraft and represents one of the most challenging environments. Upon leaving earth's atmosphere spacecraft are continuously assaulted from a near total vacuum, microgravity, atomic oxygen, ionizing radiation, micrometeoroids, space debris, and severe thermal gradients [2,150]. In addition, nearly all spacecraft are launched with the intent of never performing a single maintenance action, which intensifies the requirement for engineers to construct vehicles of the highest caliber.

Most materials in a vacuum undergo the process of outgassing which is the release of its native substances as a gas or vapor. Outgassing is particularly important when considering how it affects a vehicle's electronics and sensors, thus degrading its performance and lifespan. Outgassing products raise the local pressure in the vicinity of the spacecraft materials, resulting in a pressure gradient with higher pressures near the material surface and lower pressures away from the spacecraft. The high pressures

resulting from the contaminating gas lower the breakdown voltage and reduce the ability of the region to support high electrical-field stresses. The breakdown characteristics measured for the outgassed mixtures from the materials are predictable allowing engineers to account for and incorporate outgassing into their designs [16].

Microgravity creates fluid containment problems and atomic oxygen severely corrodes the surface of materials in low earth orbit (LEO). The fluid containment issue is directly related to the heat transfer properties of a material. Thermal management is paramount to ensure projected lifetime is achieved with space's high thermal gradients. Atomic oxygen fosters an accelerated oxidation rate and may result in premature structural failure. In addition, when a spacecraft moves through atomic oxygen a flux is generated on material surfaces and energy is produced resulting in changes to a material's surface properties. Space tests indicate that the probability of a chemical reaction of atomic oxygen with carbon is only 13% and the use of protective coatings will significantly reduce this number [4].

Micrometeoroids and space debris greatly affect the condition and ability of spacecraft to perform their designated functions. The amount of cosmic junk floating near earth is due to the lack of foresight and planning of early space policy. The race to space failed to implement mitigation measures in order to prevent the unwanted release of debris into space. Not only does the continued proliferation of space debris endanger the well-being of spacecraft, but more importantly infuses greater risk to the lives of astronauts. Figure 5 depicts the immense amount of space debris currently being tracked by the National Aeronautics and Space Administration (NASA), the Federal Aviation Administration (FAA), and North American Aerospace Defense Command (NORAD).

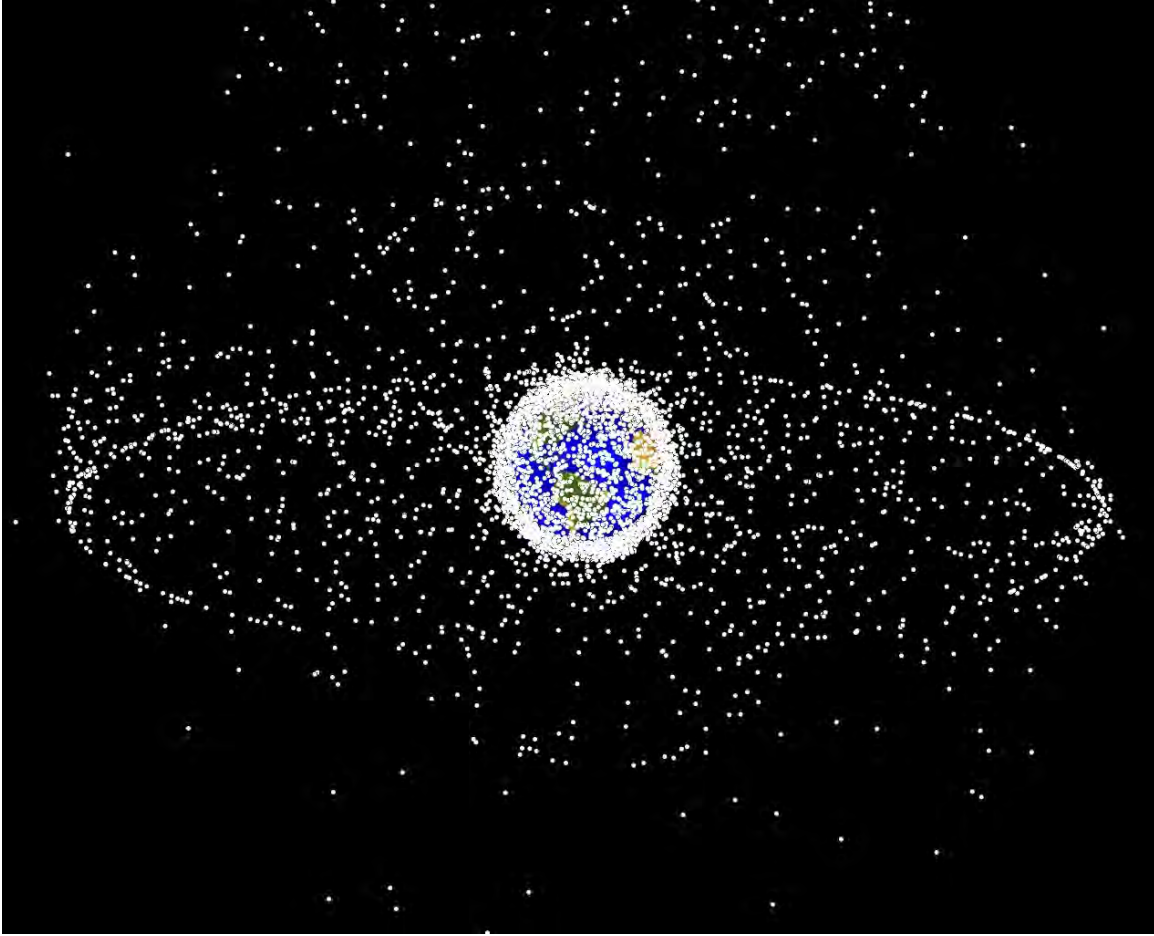


Figure 5. Computer generated image from NASA on space debris

2.2 Ionizing Radiation and Electromagnetic Interference

Space radiation is different from the kinds of radiation we experience here on Earth, such as x-rays or gamma rays. Space radiation is comprised of atoms in which electrons have been stripped away as the atom accelerated in interstellar space to speeds approaching the speed of light and eventually, only the nucleus of the atom remains [11]. This is called ionizing radiation and it possesses the capacity to remove electrons from other atoms giving birth to charged particles. Types of ionizing radiation are protons, neutrons, and gamma rays.

There are three naturally occurring sources of space radiation: trapped radiation, galactic cosmic radiation (GCR), and solar particle events (SPE). The rotation of the Earth's molten iron core creates electric currents that produce magnetic field lines around the Earth, which extends several thousand kilometers out from the surface of the Earth. The Sun emits a constant stream of particles, called the solar wind that varies in intensity with the amount of surface activity on the Sun. Few charged particles of the solar wind penetrate the Earth's magnetic field with the remaining being deflected, however, some become trapped and circulate along the Earth's magnetic lines of force. GCR originates outside the solar system and consists of ionized atoms ranging from a single proton up to a uranium nucleus. The rate of flow (flux) levels of these particles is very low.

However, since they travel very close to the speed of light and because some of them are composed of very heavy elements such as iron, they produce intense ionization as they pass through matter. SPEs are injections of energetic electrons, protons, alpha particles, and heavier particles into interplanetary space. These particles are accelerated to near relativistic speeds by the interplanetary shock waves which precede fast coronal mass ejections and which exist in the vicinity of solar flare sites. They temporarily enhance the radiation in interplanetary space around Earth's magnetosphere, and they may penetrate to low altitudes in the polar regions [11].

Ionizing radiation causes a charge buildup on the surface of spacecraft and this electromagnetic current produces EMI. EMI is a product of electrostatic discharge (ESD) and ESD materializes through the upsurge of a spacecraft's capacitance. EMI is exceptionally detrimental to a spacecraft's electronics and can swiftly render it inoperative for extended periods of time or result in permanent failure.

2.3 EMI Shielding Effectiveness of Nanofibers

Past studies on the shielding effectiveness (SE) of CNTs against EMI have revealed promising results. Ning *et al.* reported on SWNT-polymer composites and the EMI SE was tested in the frequency range of 500 MHz – 1.5 GHz. The EMI SE was found to correlate with the DC conductivity as shown in Figure 6, and reflection dominated this frequency range. The effects of SWNT wall defects and aspect ratio (ratio of length-to-diameter) on EMI SE were also studied and the results are displayed in Figure 7. All three samples tested in Figure 6 had composites containing 10 wt % SWNTs. Figure 8 shows an SEM image of the SWNT composites cross of section with 10 wt % loading. For clarification, long SWNTs exhibited the largest bundle length/diameter aspect ratio, short SWNTs exhibited the smaller aspect ratio, and annealed SWNTs were obtained after annealing short SWNTs at 1110 °C for three hours in a tube furnace. High temperature annealing of SWNTs in an inert gas or vacuum can remove wall defects. This annealing treatment was expected to improve DC conductivity and thus EMI SE, which was observed and graphed in Figure 7. The best performance for EMI SE belonged to long SWNTs and revealed that aspect ratio was more important than removing CNT wall defects for improving EMI SE. All Ning *et al.* results were in agreement with EM theory [13].

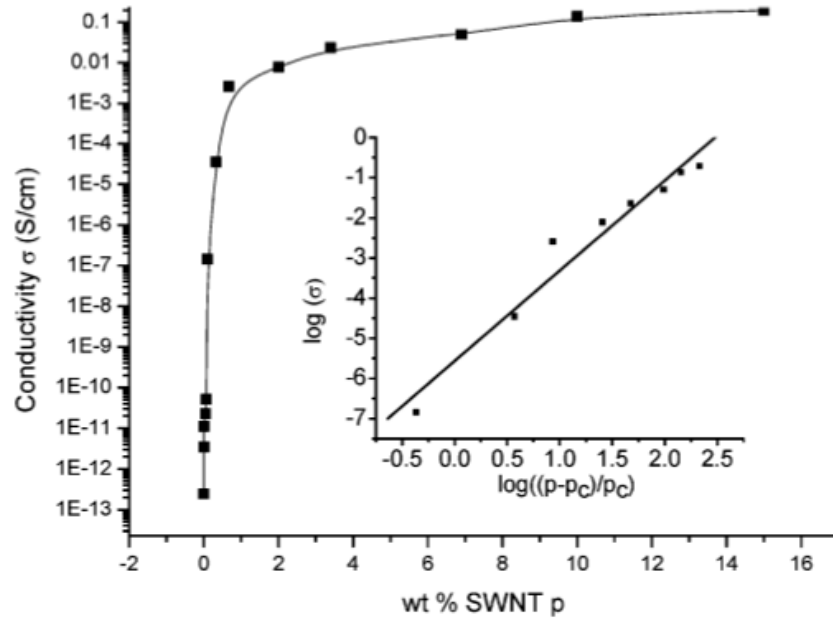


Figure 6. Log DC conductivity (σ) vs mass fraction (p) of SWNTs – long composites measured at room temperature. Inset: log – log plot for σ vs $((p-p_c)/p_c)$ for the same composites [13].

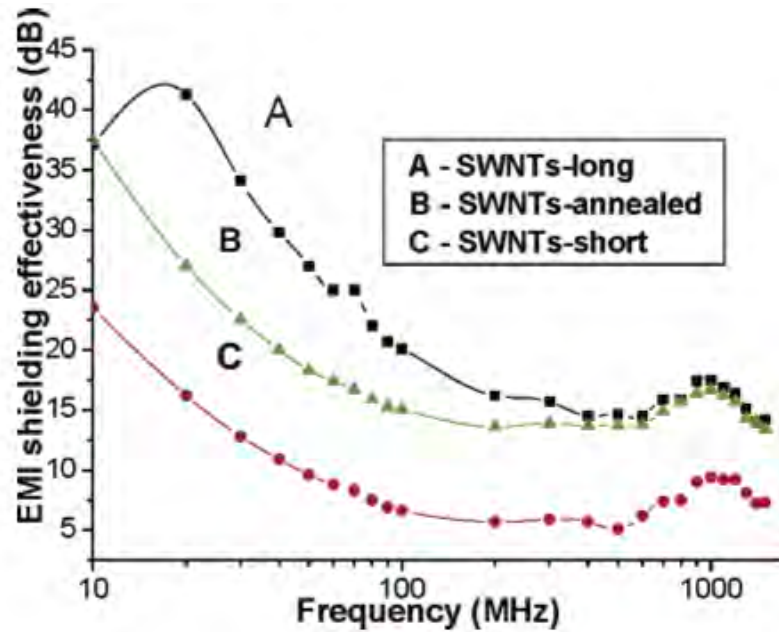


Figure 7. Impact of wall integrity and aspect ratio on the EMI shielding effectiveness of the composites containing 10 wt % SWNTs [13]

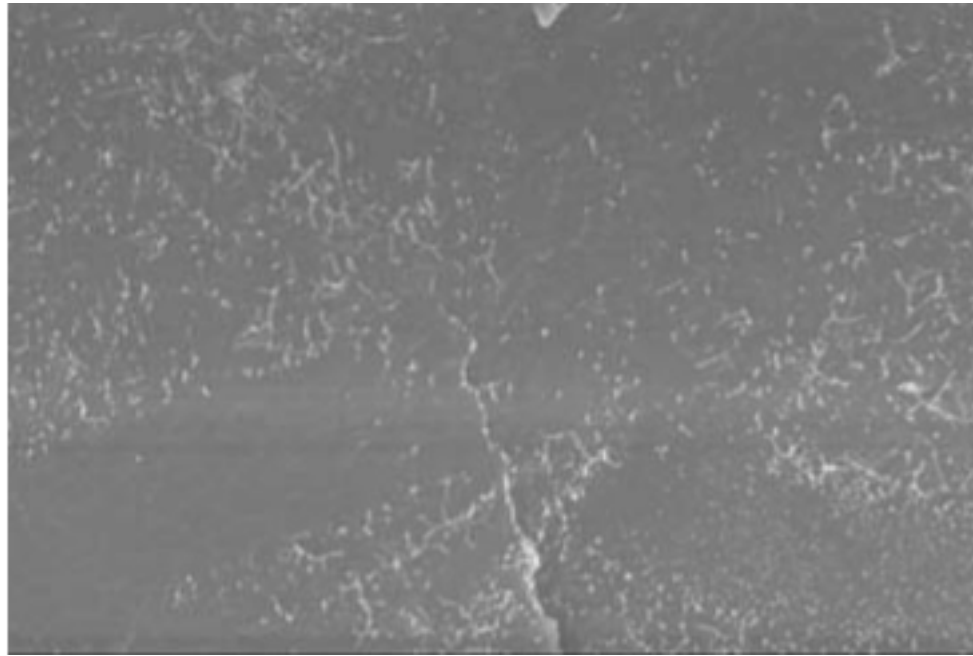


Figure 8. SEM image of the cross of section SWNTs – composites with 10 wt % loading [13]

Yang *et al.* studied EMI shielding characteristics of carbon nanofiber-polystyrene composites containing SWNTs that were investigated in the frequency range of 12.4 –18 GHz (Ku-band). It was observed that the shielding effectiveness of such composites was frequency independent, and increased with increasing carbon nanofiber loading within Ku-band. The experimental data exhibited that the shielding effectiveness of the polymer composite containing 20 wt % carbon nanofibers could reach more than 36 dB in the measured frequency region, indicating such composites can be applied to the potential EMI shielding materials. In addition, the results showed that the contribution of reflection to the EMI shielding effectiveness was much larger than that of absorption,

implying the primary EMI shielding mechanism of such composites was reflection of electromagnetic radiation within Ku-band [20].

Xiang *et al.* studied the EMI shielding properties of MWNT nanocomposites in the frequency range of 8 – 12 GHz (X-band) and 26.5 – 40 GHz (Ka-band). They reported that the EMI SE of the nanocomposites increased with increasing CNT content. The improvement of SE was primarily attributed to enhanced conductivity due to the addition of MWNTs matching the findings of Ning *et al.* They observed that MWNTs have excellent electrical conductivity and high aspect ratio easily leading to the formation of conducting networks within a matrix. The conducting networks interacted with and attenuated the EMI radiation remarkably well [19].

Park *et al.* studied EMI SE using a composite comprised of CNTs integrated with a reactive ethylene terpolymer (RET). Such composites were synthesized through the chemical reaction of the functional groups on the CNT with the epoxy linkage of the RET polymer. The main advantages of these composites include good dispersion with low electrical percolation volume fractions (~ 0.1 volume %), yielding outstanding microwave shielding efficiency for EMI applications. The shielding effectiveness was characterized for both SWNT and MWNT-based composites and was much enhanced in the former. The specific roles of absorption and reflection in determining the total shielding, as a function of the nanotube filling fraction, was also discussed [14].

Harder studied M55J/RS-3 composites combined with nickel nanostrands (NS) and reported negligible change to the EMI shielding properties after placing the specimens under increasing tensile loading up to ultimate failure. Furthermore, the configuration providing the highest level of EMI shielding was the Exterior specimen,

which had an improvement in EMI shielding performance of approximately 25% over the control specimen that lacked NS. The Exterior specimen also outperformed the other three configurations in terms of conductivity, which is in agreement with the findings of Ning *et al.* and Xiang *et al.* [7].

2.4 Summary

Outer space is irrefutably one of the most unforgiving environments to operate within due to its copious and incessant threats. Objects are exposed to a vacuum, microgravity, atomic oxygen, ionizing radiation, micrometeoroids, space debris, and intense thermal gradients. These hazards impose the requirement to have well designed and manufactured vehicles in order to ensure longevity and mission effectiveness. Herculean efforts have been made and are ongoing to discover new materials and methods to improve the quality and capability of future spaceborne systems.

EMI mitigation is absolutely crucial in defending a spacecraft's well-being against its vulnerability to electronic degradation and failure. Ionizing radiation is a formidable menace and is combated through the utilization of highly conductive materials. Fortunately, CNTs possess the capacity to protect against EMI and its destructive effects while offering excellent thermal management and high specific strength.

Past research validates the use of nanofibers as a viable, conductive filler material in safeguarding against EMI. Composites with CNTs as EMI shielding material harvest abundant gains over their traditional counterparts such as lighter weight and superior resistance to corrosion. Nanocomposites hold overwhelming value and matchless

potential for wide applications and more research is required in order to fully comprehend their benefits.

Methodology

Research methodology is described in conjunction with the laboratory equipment and the manner in which they were employed. Details of the focused beam test, monotonic tension test, thermal cycling test, and EMI test equipment and procedures are provided. The type of experimental data recorded is highlighted. The final item discussed is the error analysis associated with the types of testing performed.

3.1 Introduction

Each unique nanocomposite panel is described along with its shorthand notation specific to this thesis. Nanocomp Technologies, Inc. (NCTI) based in Concord, New Hampshire manufactured all four configurations of nanocomposites. The monotonic tension tests and thermal cycling tests and procedures are outlined and were performed at the Air Force Institute of Technology located at Wright-Patterson AFB, Ohio. Focused beam tests and EMI tests and procedures are provided and all measurements were taken at the Air Force Research Laboratory Materials and Manufacturing Directorate (AFRL/RX) located at Wright-Patterson AFB, Ohio.

3.2 Specimen Preparation

Four, 30.48 cm x 30.48 cm (12 in x 12 in) nanocomposite panels were constructed from Cycom 5575-2 glass with multi-walled CNT (MWNT) plies as illustrated in Figure 9. The first configuration was made entirely from Cycom 5575-2 glass with no CNT plies and will be referred to as *8G*. The second configuration had four CNT plies on one-half with four glass plies on the other half and will be referred to as *4G/4CNT*. The third configuration had two plies of CNT on the exterior of each side with four plies of glass in

the middle and will be referred to as *2CNT/4G/2CNT*. The fourth configuration had alternating CNT plies and glass plies across the thickness and will be referred to as *(G/CNT)₄*. Figure 9 shows the stacking sequence for all four designs. Firstly, all four panels were focused beam tested at the Air Force Research Lab Manufacturing and Materials Directorate (AFRL/RX) and then hand carried to the AFIT machine shop where they were cut into 15.24 cm x 2.54 cm (6 in x 1 in) strips by a high-pressure waterjet cutter. Compressing each panel between two plastic sheets with dual sided adhesive tape mitigated edge delamination. The average thickness of the four nanocomposite panels was 1.215 cm. A 15.24 cm x 2.54 cm (6 in x 1 in) test sample is shown in Figure 10 and represents the geometry of all test samples for this thesis.

Glass	Glass	CNT	Glass
Glass	Glass	CNT	CNT
Glass	Glass	Glass	Glass
Glass	Glass	Glass	CNT
Glass	CNT	Glass	Glass
Glass	CNT	Glass	CNT
Glass	CNT	CNT	Glass
Glass	CNT	CNT	CNT

8G
4G/4CNT
2CNT/4G/2CNT
(G/CNT)₄

Figure 9. 8-ply stacking sequence of nanocomposites



Figure 10. Test specimen

Each 15.24 cm x 2.54 cm (6 in x 1 in) test specimen was cleaned immediately after machining to eliminate undesirable fragments. This ensured a clean bond between the specimen and the glass/epoxy tabs. The 2.54 cm x 2.54 cm (1 in x 1in) tabs were affixed to the specimens with M-Bond 200 adhesive. The tabs were essential to protect each specimen from potential surface cracks and premature failure because of the monotonic tension testing performed by gripping the ends of each specimen.

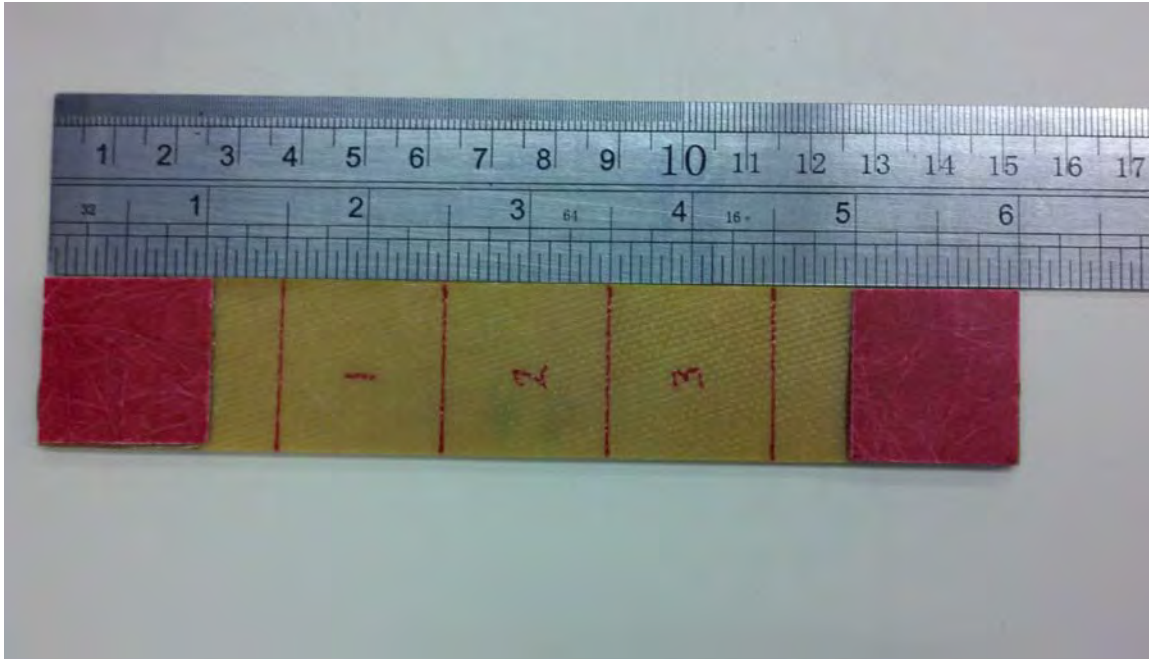


Figure 11. Test specimen with glass/epoxy tabs

3.3 Focused Beam Tunnel Test Equipment and Procedures

Focused beam tests were performed with a custom made Georgia Tech Research Institute device that was capable of testing between the frequency range of 2 GHz – 18 GHz and is displayed in Figure 12. The data collected on all four nanocomposite panels were from 2 GHz – 18 GHz in increments of 10 MHz. An AFRL/RX laboratory technician performed the calibration and data collection on all four panels in the following manner:

1.0 Calibration:

- Attach cable from PNA Port #1 to amplifier INPUT

- Attach cable from Amplifier OUTPUT to Tunnel INPUT (H-Pol or V-Pol depending on the orientation being tested)
- Attach 30dB attenuator to PNA port #2
- Attach cable from Tunnel OUTPUT to 30dB attenuator.
- Ensure that all cables are tightened to proper torque (use the proper size torque wrench found in the Focus Beam Supply drawer).
- Remove any sample from the tunnel sample plate for a RESPONSE calibration
- Verify the set configuration
 - Go to the "Sweep" tab and place the cursor over "Select Number of Points"
 - * 1601 should be selected if not select 1601
 - Go to the "Sweep" tab and select "IF Bandwidth"
 - * If the IF Bandwidth is not set to 10Hz use the dialog box to set the bandwidth to 10 Hz
 - Go to the "Channel" Tab and select "Power" from the drop down menu
 - * Set the power level to -11 dbm from port 1; ensure that there is a checkmark by Power On, Port Power Coupled, and that Auto has a checkmark next to it under Attenuator Control
- Initiate a Single Trace Scan on the PNA. This will be the RESPONSE calibration trace.
 - To initiate the Single Trace go to the "Sweep" tab. Place the cursor over the "Trigger" tab and select Single from the drop down menu
- Activate "Gate" option with gate center = 0ns and gate span = 1ns.
- Store RESPONSE trace using the Memory/Math button
- Select "Data>>Memory"
- Select "Data/Memory"
- The displayed trace should be a flat line at 0dB
- Calibrations are only valid provided that the conditions in the room do not change.
- The focus beam shall be recalibrated when one of the following occurs:
 - $\Delta \text{Time} > 4 \text{ hours}$
 - $\Delta \text{Temp} > 1^\circ$
 - $\Delta \text{Humidity}_{\text{relative}} > 5\%$

1.1 Specimen:

- Insert sample into holder. Tape and/or bolt as necessary to prevent leakage.
- *Follow instructions in the Mounting Specimen, Section 4*

1.2 Testing

1.2.1 Procedure:

- Remove attenuator from port #2 of the PNA and attach RF cable directly to port #2
- Note: The attenuator must be removed to ensure the system will function properly and prevent damage
- Initiate a Single Trace Scan on the PNA.
 - Activate "Gate" option with gate center = 0ns and gate span = 1ns.

- The resulting display will be the sample insertion loss + 30dB due to the in-line attenuator used during RESPONSE calibration.
- Subtract 30dB from displayed trace for final corrected data.
- Repeat Sample procedure for additional specimens.
- Additional Response calibration scans should be performed periodically when one of the following occurs:
 $\Delta \text{Time} > 4 \text{ hours}$
 $\Delta \text{Temp} > 1^\circ$
 $\Delta \text{Humidity}_{\text{relative}} > 5\%$

Note:

- Additional noise floor performance can be gained by reducing the IFBW.
- Gate parameters can be adjusted to observe changes in response.
- Time domain analysis can be performed on the PNA.
- Note that significant periodic nulls in the measured trace may indicate energy leakage around the edge of the sample

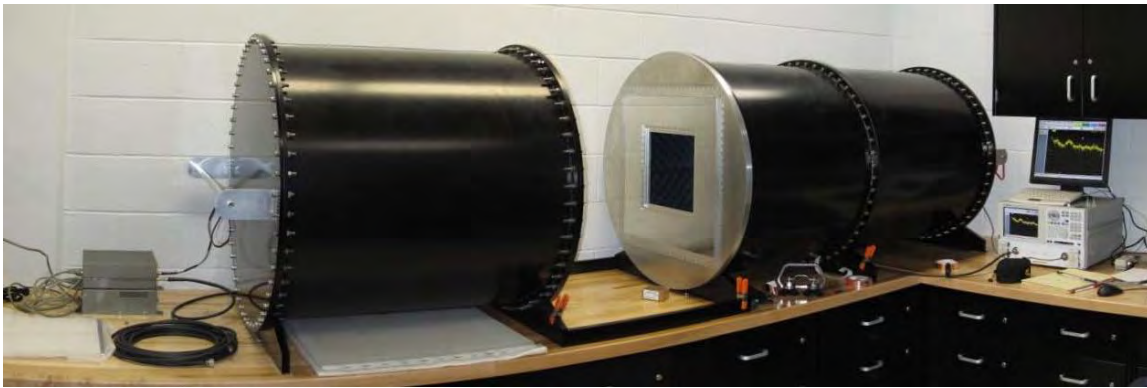


Figure 12. Focused beam tunnel

3.4 Monotonic Tension Test Equipment and Procedures

Monotonic tension tests were performed with an MTS 810 servo-hydraulic test machine that has a maximum load capacity of 22 kips (98 kN) and is displayed in Figure 13. A grip pressure of 8.2 MPa (1.2 ksi) was used for all tests with MTS 647 hydraulic wedge grips installed. The upper and lower grips were positioned to allow for the machine to grip the entire tabbed portions on each specimen. Upon placing the



Figure 13. Material Test System machine

specimens into the grips a vertical alignment procedure was performed with a hand-held, tubular bubble level. This was critical to ensure a pure uniaxial load was applied to each specimen and prevented both the collection of inaccurate data and premature failure.

All monotonic tension tests were conducted at the Air Force Institute of Technology (AFIT) at room temperature and the MTS 810 machine was warmed up prior to testing in accordance with the manufacturer's instructions. The warm up process delivered a programmed cyclic, displacement command to the machine's function

generator utilizing a square wave input at a frequency of 3 Hz and an amplitude of 0.0762 mm (0.003 in). Following completion of the MTS 810 machine's warm up, the lower grip was raised to the required testing position, the specimen was inserted and vertically aligned, and the machine's top and bottom grips were closed with a grip pressure of 8.2 MPa (1.2 ksi) as shown in Figure 14. After both grips were closed the force reading was zeroed through the force control mode prior to initiating all tests.



Figure 14. MTS machine with specimen inserted

The final step performed prior to commencing monotonic tension testing was the adjustment of the force rate on the MultiPurpose TestWare (MPT) software to achieve a stress rate of 750 kPa/sec for all specimens tested. Force rate modification was required due to the slight variations between each specimen's cross-sectional area. After entering the desired force rate, the start button was selected via the MPT software and data

collection began on the force applied (Newtons), time (sec), and displacement (in).

Testing was complete when the applied force ramped down to zero Newtons permitting for the opening of both grips and the removal of the specimen.

3.5 Thermal Cycling Test Equipment and Procedures

Thermal cycling was performed on a ThermoJet ES Precision Temperature Cycling System (Figure 16) that was manufactured by SP Scientific and capable of producing temperatures between -80 °C and 375 °C. All four nanocomposite specimens were subjected to six sets of thermal cycles as outlined in Table 1. A single thermal cycle encompassed a total soak time of 20 seconds: soaking at +60 °C for 10 seconds followed by soaking at -60 °C for 10 seconds. Figure 15 depicts the temperature output of the test section as a function of time for a time interval of 500 seconds.

Table 1. ThermoJet thermal cycles

Test Set	No. of Cycles
1	500
2	1500
3	2500
4	3500
5	4500
6	5000
Total	= 17500

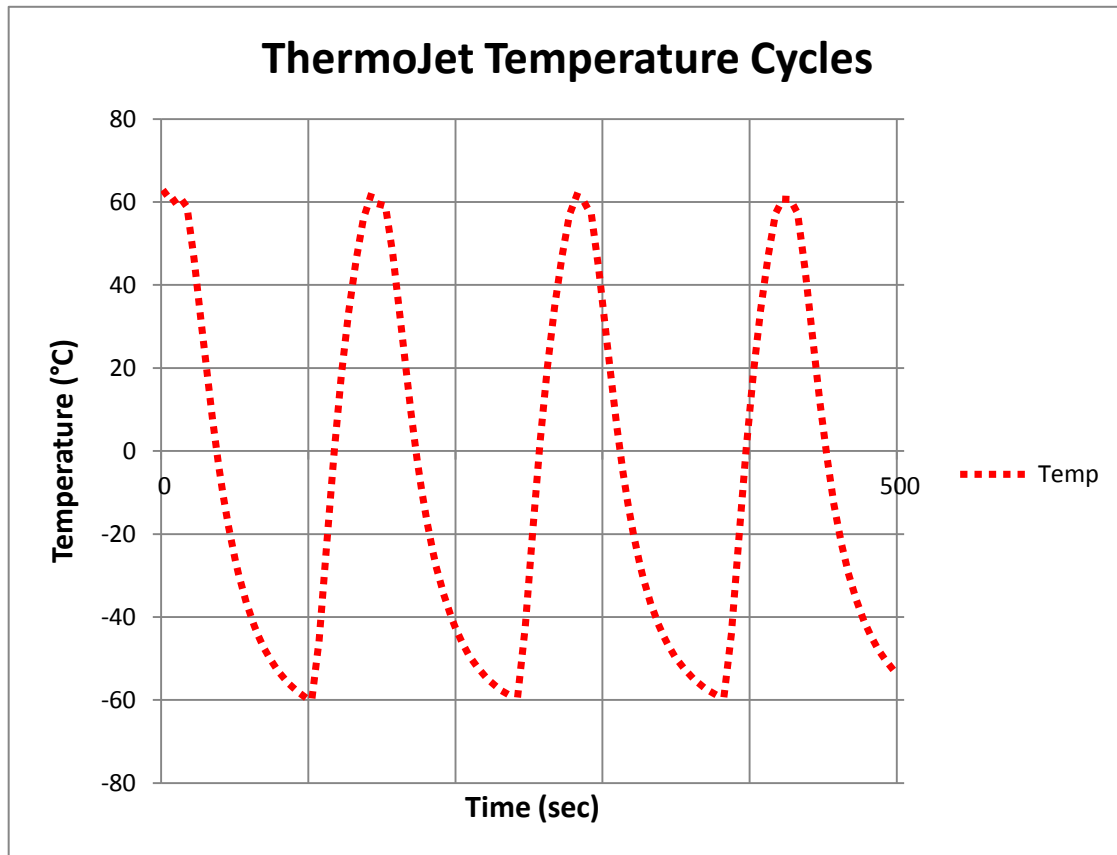


Figure 15. Thermal cycles from +60 °C to -60 °C

Preparation for thermal cycling entailed placing all four strips within foam spacers to provide adequate exposure of each individual specimen's surface area to the test hood's temperature and is displayed in Figure 17. All four specimens were then placed under the test hood and an external Device Under Test (DUT) thermocouple was attached to one of the two inner specimen with a key ring for controlling temperature accuracy at the test device as shown in Figure 18. The desired test parameters were



Figure 16. ThermoJet test device

entered through the control panel attached to the test device with the following selections: 1) “Utilities”, 2) “Control Status”, 3) “DUT Control” – On, and 4) “Max Air Flow” – 20. The remaining inputs under the “Program” submenu were for temperature, rate and soak time and are illustrated in Figure 19. Calibration was not required with the output temperature being factory calibrated with a National Institute of Standards and Technology traceable device. Testing commenced upon the completion of entering all the desired test parameters with the DUT thermocouple attached and selecting “Run” on the “Program” submenu. The workstation connected to the ThermoJet test device recorded the DUT temperature as a function of time and was used to verify proper operation with respect to the selected soak temperatures and number of cycles. After a test set was finished, the DUT thermocouple was detached from its associated specimen and all four specimens were removed from the test hood area.

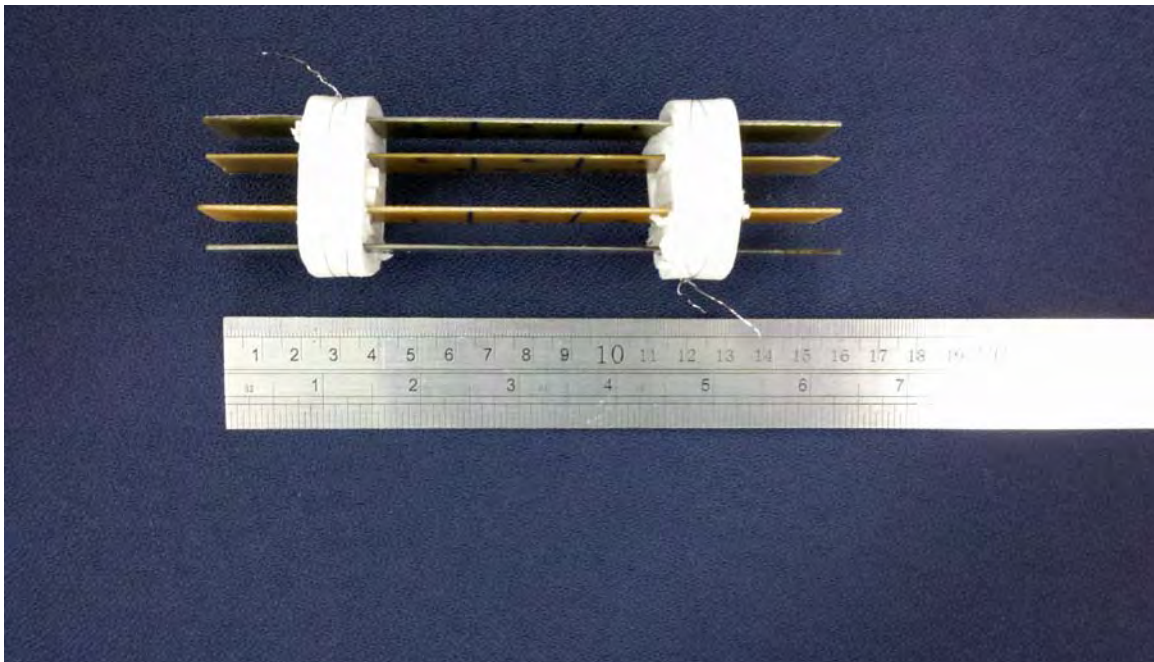


Figure 17. Test specimens inserted into foam spacers

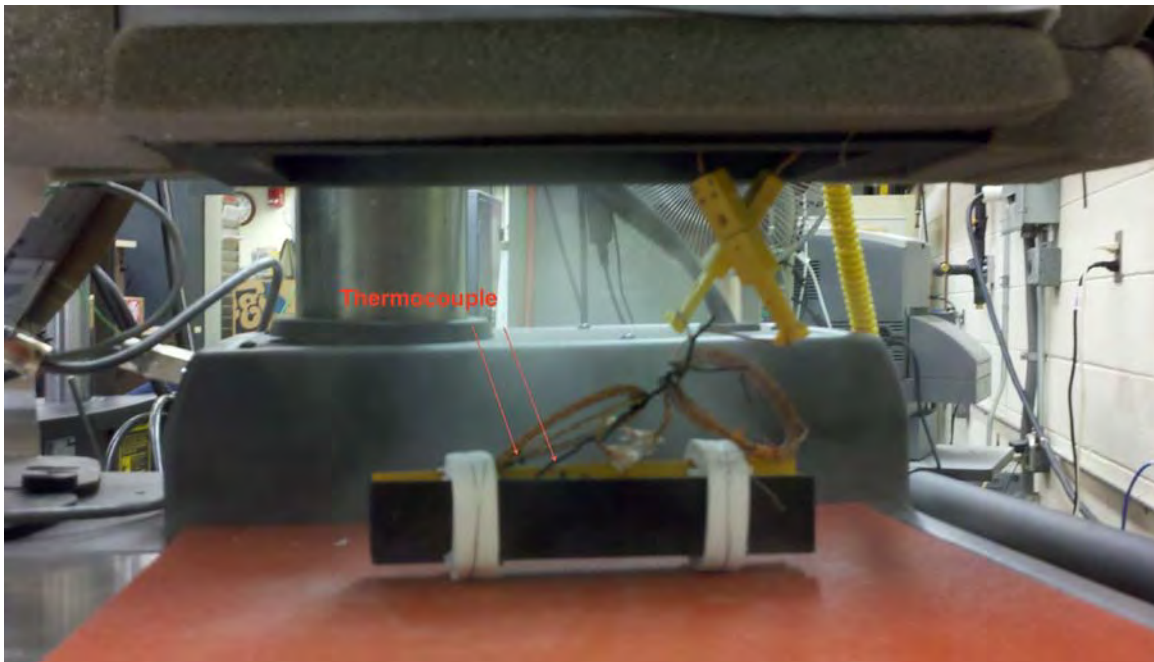


Figure 18. Test specimens attached to DUT thermocouple - ThermoJet test device



Figure 19. ThermoJet test device control panel – Program submenu

3.6 EMI Test Equipment and Procedures

All EMI tests were performed at the AFRL Materials and Manufacturing Directorate (AFRL/RX) at room temperature. EMI measurements were conducted in terms of decibels (dB) with the Agilent Technologies E8362B PNA Series Network Analyzer (Figure 20) before and after each monotonic tension test and/or thermal cycling test. The data collected on the Network Analyzer enables others to observe the behavior of the four nanocomposite configurations tested and determine how tensile loading and thermal cycling affect their EMI SE.

Calibration procedures were executed prior to conducting EMI measurements on the Network Analyzer. Table 2 outlines the calibration steps performed and they were essential to collect accurate data for the frequency range of 8.2 GHz – 12.4 GHz. EMI measurements were taken at the same locations for each specimen, with 201 continuous sweep points, S12 trace, and auto-correction selected. Figure 21 illustrates the three marked sections and how each specimen was secured horizontally between the adapters for measurements as shown in Figure 22. Five measurements were taken in a given section prior to progressing to the next section and this process was repeated until a total of fifteen EMI measurements were recorded for one specimen. EMI measurements recorded attenuation data in units of decibels (dB) with auto-scale selected.

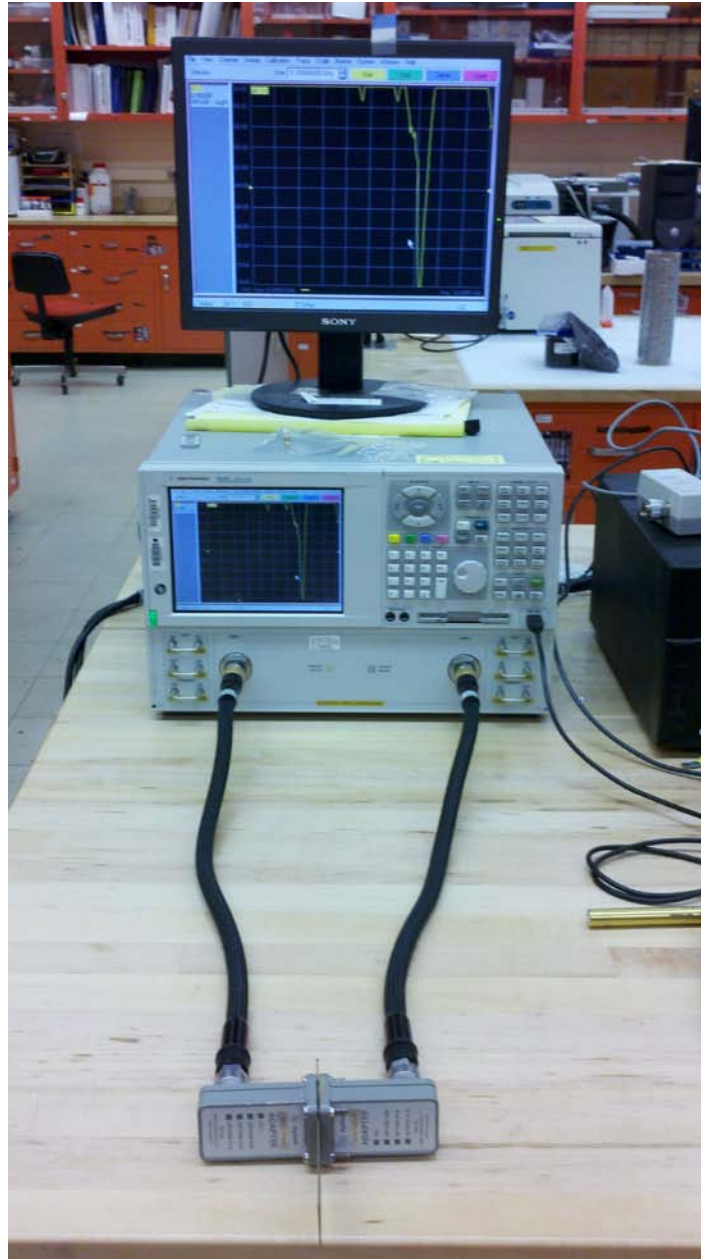


Figure 20. Agilent Technologies E8362B PNA Series Network Analyzer

Table 2. Network Analyzer calibration procedure

1	Select: Network Analyzer software application
2	Select: File, Recall previous test
3	Set Begin and End frequencies: Yellow = 8.2 GHz; Green = 12.4 GHz
4	Select: Calibration Wizard
5	Select: Unguided, TRL, 1-2 Ports, Cal Kit #29 (X-band)
6	Select: Next, Through Standard, Reflect Standard
7	Insert SHORT plate onto adapter (piece without rectangular hole)
8	Select: both SHORT push-buttons
9	Remove SHORT plate
10	Insert LINE plate onto adapter (thickest piece with rectangular hole)
11	Select: LINE push-button, X-Band $\frac{1}{4}$ wavelength line, Next
12	Remove LINE plate
13	Tighten both end adapters with nothing in between
14	Select: THRU, Next, Finish



Figure 21. Test specimen divided into three sections for EMI measurements



Figure 22. Test specimen secured horizontally between Network Analyzer adapters

3.7 Test Plan Summary

The test procedures were developed in order to meet the objective of characterizing the EMI SE of CNTs and CNT composites undergoing monotonic tension testing and/or thermal cycling. The four nanocomposite specimens were each tested by means of monotonic tension, thermal cycling, and a combination of thermal cycling pursued by monotonic tension. EMI measurements were taken before and after monotonic tension testing and/or thermal cycling in order to determine the EMI SE behavior of the four nanocomposites. The first set of four nanocomposites tested is referred to as Group 1 and they experienced monotonic tension testing only with increments of 50 MPa (7.251 ksi) up to ultimate failure. 50 MPa (7.251 ksi) equates to 9.45% of ultimate tensile strength (UTS) for 8G, 12.2% UTS for 4G/4CNT, 13.33% UTS

for 2CNT/4G/2CNT, and 10.14% UTS for (G/CNT)₄. The second set of four nanocomposites tested is referred to as Group 2 and they were initially subjected to thermal cycling tests in accordance with Table 1 in section 3.5. Group 2 then faced monotonic tension tests subsequent to the 17,500 thermal cycles in the following increments for all four specimens: 25% UTS, 50% UTS, 75% UTS, and 95% up to ultimate failure. The third set of four nanocomposites tested is referred to as Group 3 and they underwent monotonic tension testing only in increments of 25% UTS, 50% UTS, 75% UTS, and 95% up to ultimate failure. Table 3 presents a summary of all tests performed for the three sets of four nanocomposites, and note that each group of four was identical with respect to the specimens tested: 8G, 4G/4CNT, 2CNT/4G/2CNT, and (G/CNT)₄.

Table 3. Test Matrix				
Testing Method	Group 1	Group 2	Group 3	
Focused Beam	Yes	Yes	Yes	
Monotonic Tension	Yes	Yes	Yes	
Thermal Cycling	No	Yes	No	
EMI Attenuation	Yes	Yes	Yes	

3.8 Error Analysis

The degree of error introduced by the MTS 810 servo-hydraulic test machine, Agilent Technologies E8362B PNA Series Network Analyzer, and ThermoJet ES Precision Temperature Cycling System were all negligible with respect to the Focused

Beam Tunnel test. The MTS 810 servo-hydraulic test machine has a dynamic load error of 1.0%, the Agilent Technologies E8362B PNA Series Network Analyzer operator's manual states that the calibration procedure and proper settings eliminate measurement errors, and the ThermoJet ES Precision Temperature Cycling System has a temperature setting accuracy of ± 1 °C and a discharge nozzle stability accuracy of ± 0.5 °C.

Each 30.48 cm x 30.48 cm (12 in x 12 in) nanocomposite panel was initially prepared for the focused beam tunnel test by inserting it into copper holding tape as shown in Figure 23 in order to ground the test sample. Next, an aluminum plate was placed beside the test sample to construct a rigid frame to hold the sample in place and additional copper tape was applied to the remaining area for coverage along the entire perimeter of the test sample. Figure 24 represents the final image of a test sample prior to commencing the focused beam test.

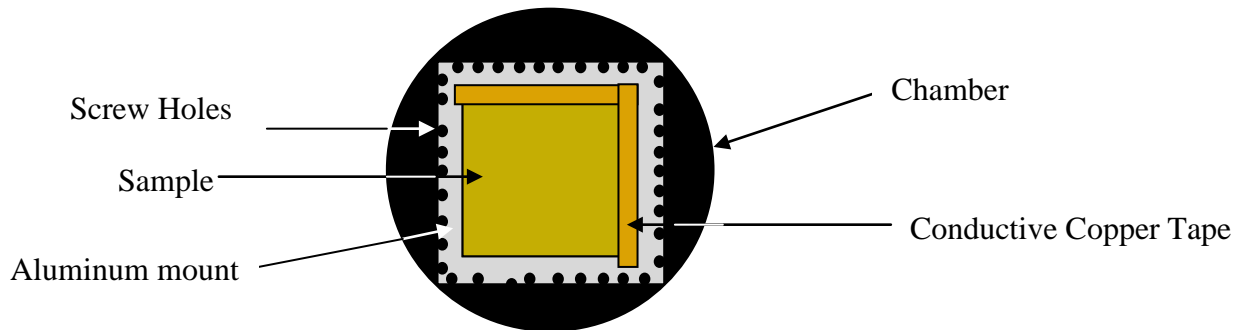


Figure 23. Simplified diagram of grounding the sample

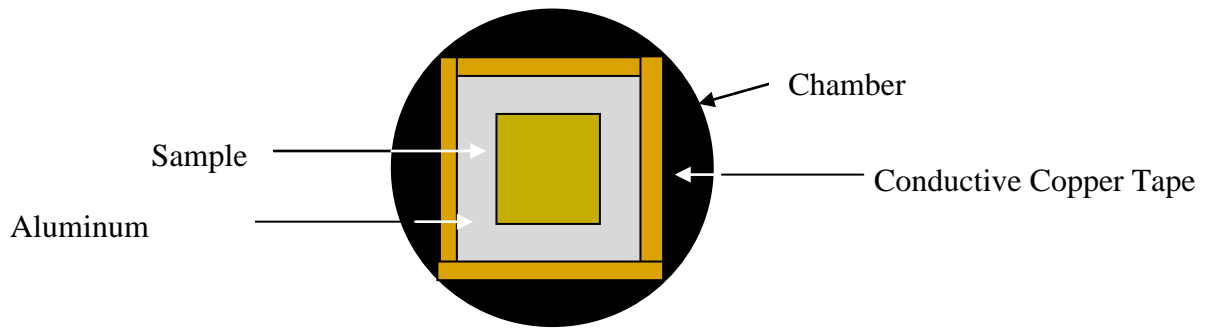


Figure 24. Final view of fully prepared test sample

Thus, a 30.48 cm x 30.48 cm (12 in x 12 in) panel is only tested in a square having dimensions of approximately 17.78 cm x 17.78 cm (7 in x 7 in). The three groups of four nanocomposites tested were collected from the region covered by the aluminum plate and copper tape. These obscured edges were machined in order to provide the test samples and consequently were not measured for their properties of attenuation during the focused beam test. This resulted in a disparity between the EMI SE measurements of the focused beam test to those of the initial measurements taken for each specimen prior to testing. Therefore, when evaluating attenuation levels (dB) only the observed trend in EMI SE performance for a given specimen is of importance, and excludes the ability to compare EMI SE focused beam results to monotonic tension and thermal cycling test results.

Analysis and Results

4.1 Introduction

This chapter presents a complete description of the experimental results collected throughout the course of this research. The four nanocomposite designs were each tested in focused beam, monotonic tension, thermal cycling, a blend of thermal cycling followed by monotonic tension, and EMI shielding effectiveness (SE). These tests allowed for the evaluation of EMI SE performance amongst the four designs. All four, 8-ply test specimens had a 3-harness satin weave, Astroquartz II (S-glass) fabric made from high purity 99.95% SiO₂ quartz crystals with Cycom 5575-2 cyanate ester prepreg resin. The three designs having carbon nanotubes (CNT) utilized multi-walled CNTs (MWNT) with an estimated length of 700 μm , diameter 8 - 15 nm, 90 wt %, and a concentration of 18.3 grams/m² (GSM) of CNTs. The CNT plies were a sheet layer that contained no matrix material and solely MWNTs. The average CNT layer thickness was 84.89 μm , the average glass/epoxy layer thickness containing warp strands was 212.53 μm , the average glass/epoxy layer thickness containing fill strands was 271.25 μm , and the average total thickness was 1.215 mm.

The first design was made entirely from Cycom 5575-2 glass with no CNT plies and will be referred to as *8G*. The second design had four CNT plies on one half with four glass plies on the other half and will be referred to as *4G/4CNT*. The third design had two CNT plies on the exterior of each side with four glass plies in the middle and will be referred to as *2CNT/4G/2CNT*. Lastly, the fourth design had alternating CNT

plies and glass fabric across the thickness and will be referred to as $(G/CNT)_4$. Figure 25 displays the cross-sectional view of all four nanocomposites.

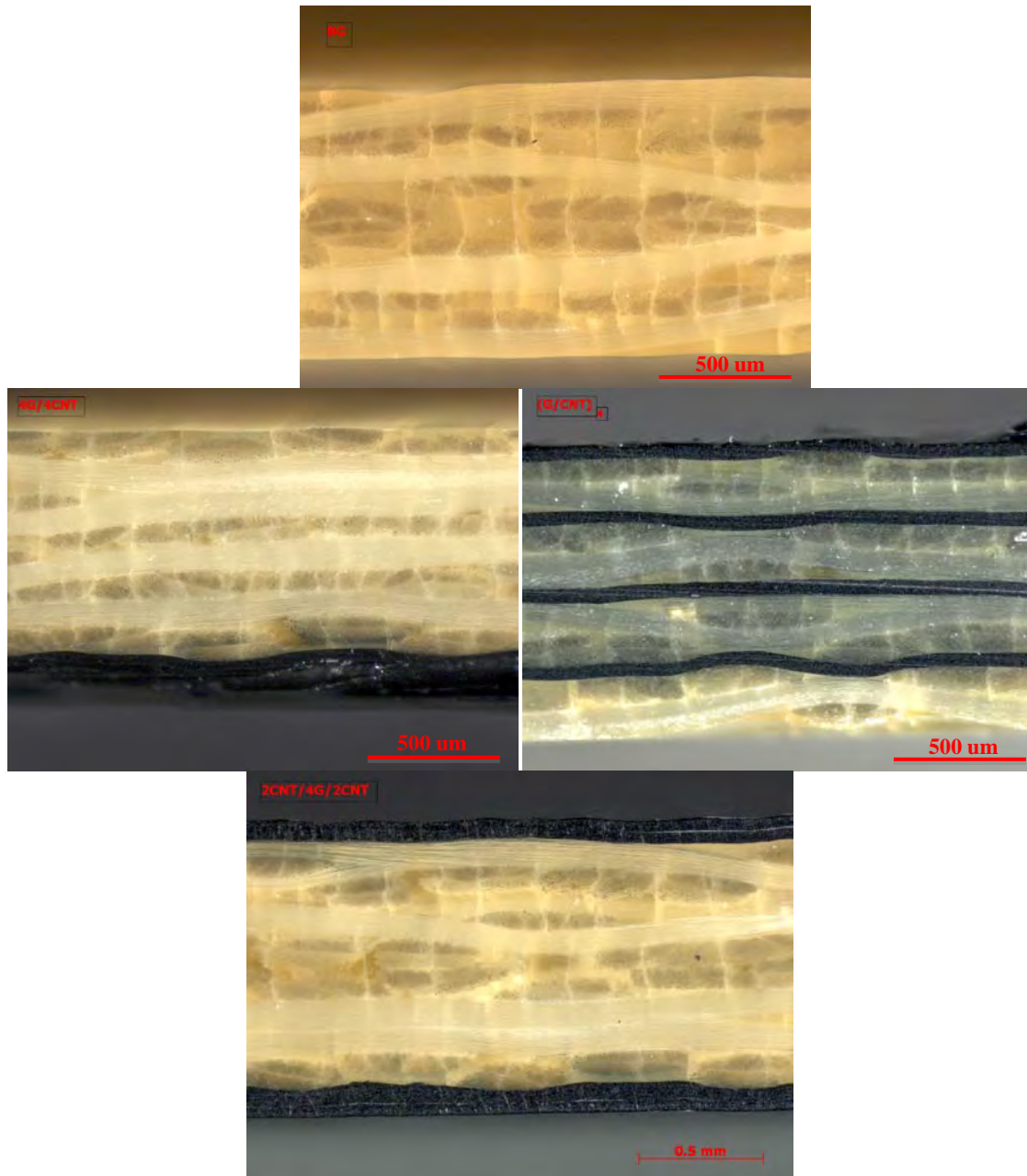


Figure 25. Cross-sectional view of four designs: top - 8G, left - 4G/4CNT, right - $(G/CNT)_4$, bottom - 2CNT/4G/2CNT

All test specimens had EMI SE measurements taken before and after both monotonic tension tests and thermal cycling tests. The values recorded prior to testing provided the baseline necessary to assess the EMI SE behavior of the four designs while exposing them to increasing tensile load and increasing number of thermal cycles.

4.2 Focused Beam

The first test performed on all specimens was the focused beam test in the frequency range of 2 GHz – 18 GHz and in terms of decibels (dB). The focused beam test facilitated the EMI SE comparison between the four tested configurations to two types of aluminum. EMI SE values are directly proportional to a material's degree of conductivity and thus its ability to combat the harmful effects of EMI. An Air Force Research Laboratory (AFRL) technician accomplished all focused beam tests and only one test was performed for each 30.48 cm x 30.48 cm (12 in x 12 in) panel.

The focused beam test results for 2024 aluminum, 7075 aluminum, 8G, 4G/4CNT, 2CNT/4G/2CNT, and (G/CNT)₄ are all shown in Figure 26. The graphed values for each panel are moving average trend lines. Both types of aluminum were comparable with respect to their EMI SE values throughout the entire frequency range and surpassed all four nanocomposite designs in EMI SE performance. The 8G trend line is challenging to view due to its average EMI SE value of 0.33 dB, which is in close proximity to the zero dB line. The 4G/4CNT and 2CNT/4G/2CNT lines were almost equal in EMI SE throughout the tested frequency range of 2 GHz – 18 GHz.

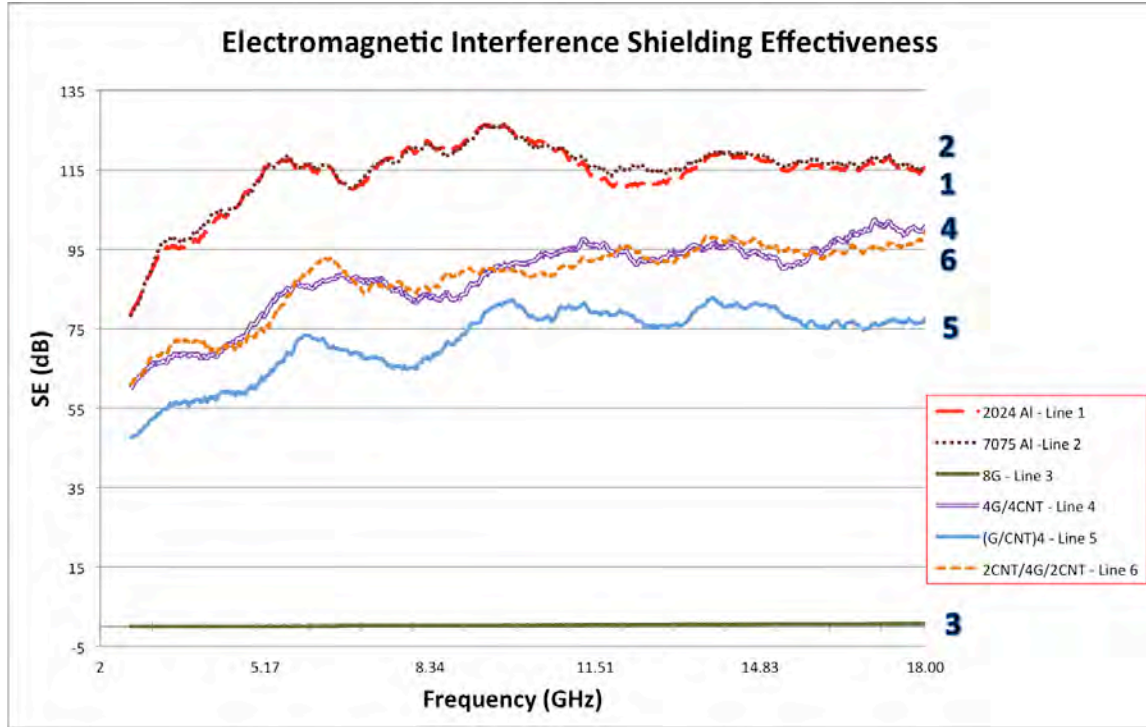


Figure 26. Focused beam test results

As expected, the control sample containing zero CNT plies had the worst EMI SE performance and the two best designs were the 2CNT/4G/2CNT and 4G/4CNT configurations. The (G/CNT)₄ configuration had ~17.98% reduction in EMI SE performance than the 2CNT/4G/2CNT and 4G/4CNT configurations. The average EMI SE values were as follows: 1) 2024 Al – 113.2055 dB, 2) 7075 Al – 113.9891 dB, 3) 4G/4CNT – 87.4971 dB, 4) 2CNT/4G/2CNT – 87.4767 dB, 5) (G/CNT)₄ – 71.7599 dB, and 6) 8G – 0.3276 dB.

4.3 Monotonic Tension – Group 1

The first set of four nanocomposites tested will be referred to as Group 1 and they were subjected solely to monotonic tension tests in increments of 50 MPa (7.251 ksi) up to ultimate failure. 50 MPa (7.251 ksi) equates to 9.45% of ultimate tensile strength

(UTS) for 8G, 12.2% UTS for 4G/4CNT, 13.33% UTS for 2CNT/4G/2CNT, and 10.14% UTS for (G/CNT)₄. 8G fractured on the eleventh loading cycle at a stress value of 543.99 MPa (78.9 ksi). 4G/4CNT fractured on the ninth loading cycle at a stress value of 409.89 MPa (59.45 ksi), 2CNT/4G/2CNT fractured on the eighth loading cycle at a stress value of 373.61 MPa (54.19 ksi), and (G/CNT)₄ fractured on the tenth loading cycle at a stress value of 500 MPa (72.52 ksi).

EMI attenuation levels were measured in terms of decibels (dB) before and after each monotonic tension test. The specimens were measured in the frequency range of 8.2 GHz – 12.4 GHz (X-band) and the average values presented are over the entire frequency range. Figure 27 displays how the EMI attenuation values for all four specimens decreased with increasing tensile load prior to fracture and demonstrates that the 2CNT/4G/2CNT design was superior to the 4G/4CNT and (G/CNT)₄ designs. EMI measurements were also taken after each specimen fractured in the region that remained intact and the results are summarized in Table 4. The reduction in EMI shielding performance from each specimen's initial conditions to post-fracture were 24.43% for 8G, 10.39% for 4G/4CNT, 7.22% for 2CNT/4G/2CNT, and 12.67% for (G/CNT)₄.

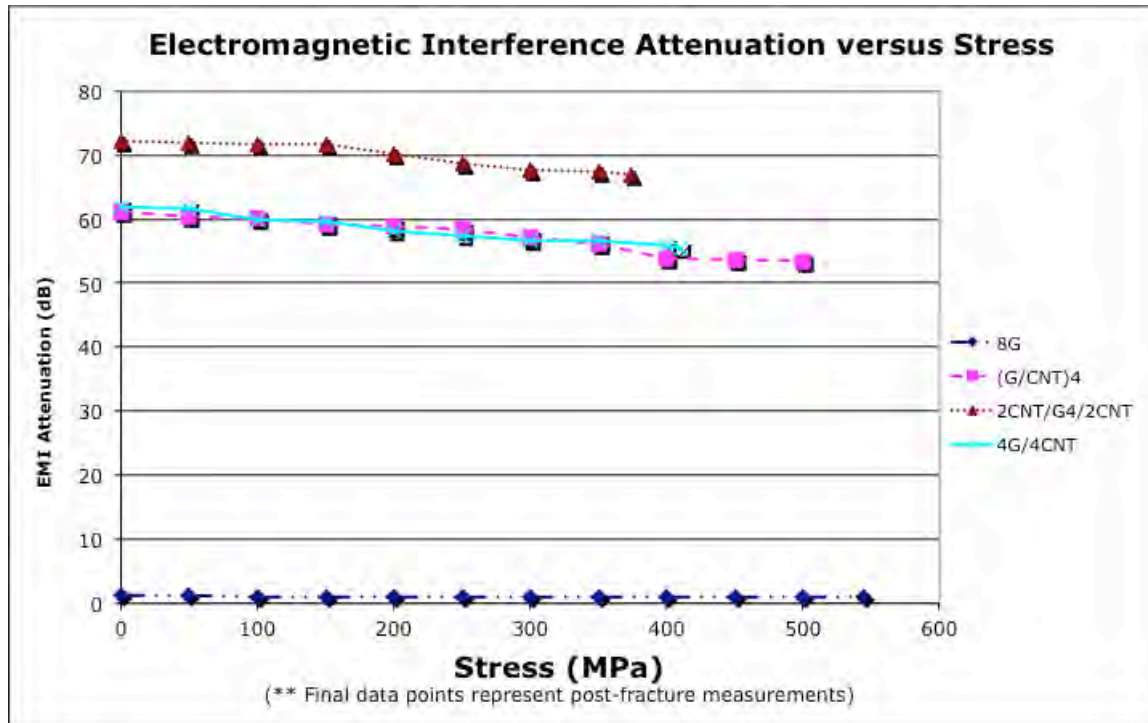
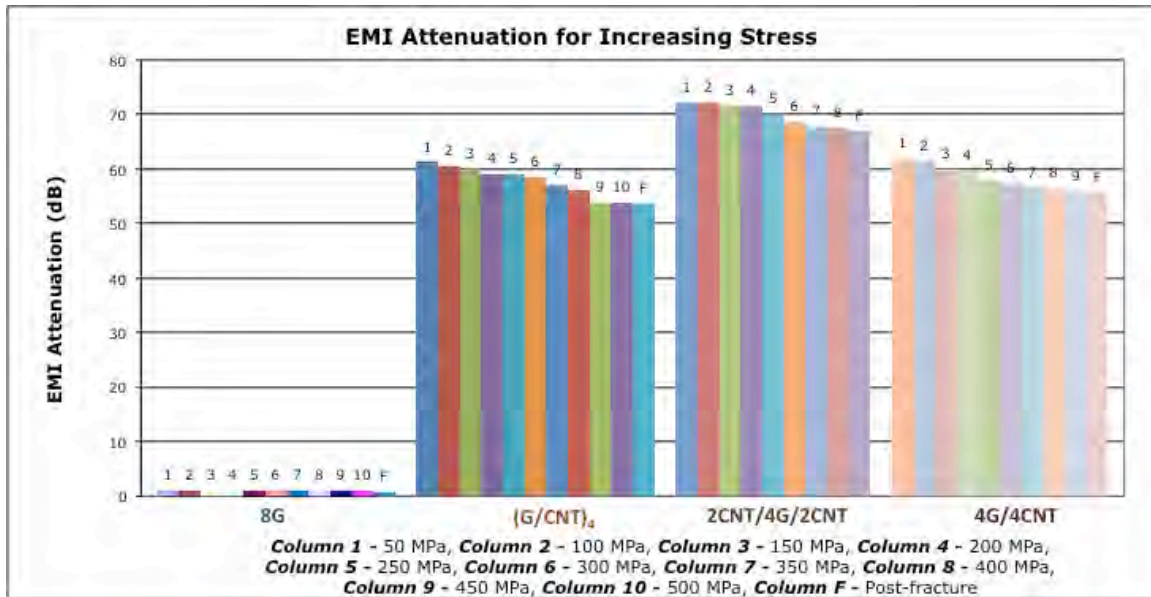


Figure 27. EMI attenuation data for Group 1

Table 4. Group 1 – Stress with corresponding EMI attenuation

Stress	8G	(G/CNT)₄	2CNT/4G/2CNT	4G/4CNT
Initial Cond	1.14316865	61.2451654	72.14762741	61.91586
50 MPa (7.25 ksi)	1.110455475	60.48026133	71.98756064	61.51206
100 MPa (14.5 ksi)	1.106545533	60.02910789	71.66176211	59.9383353
150 MPa (21.75 ksi)	1.07630853	59.16585241	71.54356462	59.72908336
200 MPa (29 ksi)	1.056845133	58.96559034	70.18699633	58.03569814
250 MPa (36.25 ksi)	1.039379345	58.44679459	68.73992672	57.42239066
300 MPa (43.5 ksi)	1.036659711	57.00585707	67.6328891	56.59847003
350 MPa (50.75 ksi)	0.976967332	56.082901	67.35907614	56.52971862
400 MPa (58 ksi)	0.935441971	53.74042815	n/a	55.82797542
450 MPa (65.25 ksi)	0.9254647	53.70886634	n/a	n/a
500 MPa (72.5 ksi)	0.897079684	n/a	n/a	n/a
Post-fracture	0.863857	53.484719	66.937528	55.482285

Figure 28 provides the EMI attenuation data normalized to each specimen's initial conditions and illustrates the degree of EMI shielding performance retained up to fracture. The 2CNT/4G/2CNT design possessed the highest level of EMI attenuation prior to tensile loading and had the smallest degree of dB loss up to and after fracture. However, the 2CNT/4G/2CNT design had the lowest UTS value of 373.61 MPa (54.19 ksi) amid all four configurations. The 8G design had the highest UTS of 543.99 MPa (78.9 ksi) yielding a difference of 170.38 MPa (24.71 ksi) between the highest and lowest UTS values for Group 1.

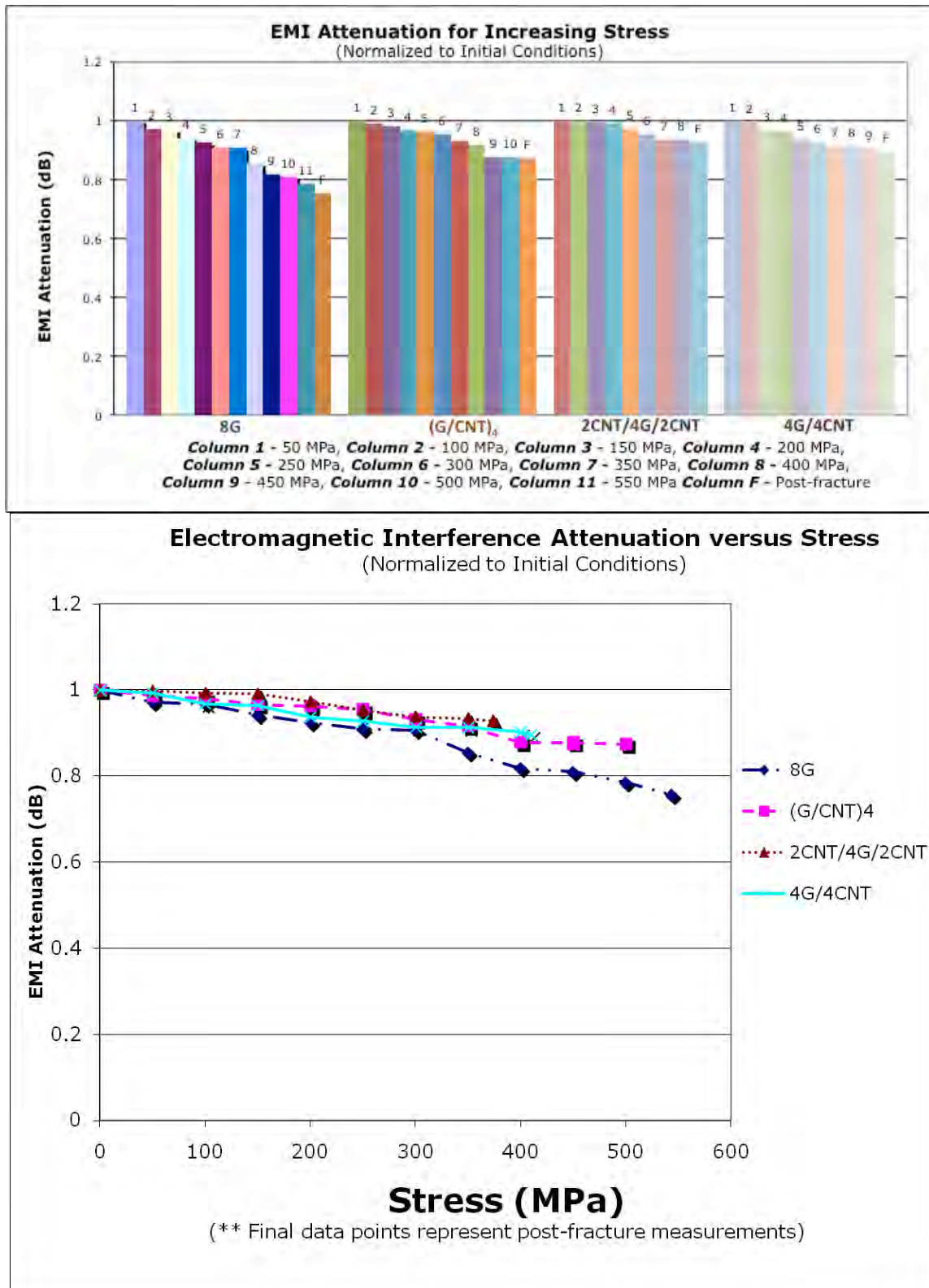


Figure 28. EMI attenuation data normalized to initial conditions for Group 1

4.4 Thermal Cycling followed by Monotonic Tension – Group 2

The second set of four nanocomposites tested will be referred to as Group 2 and they were initially subjected to thermal cycling tests followed by monotonic tension tests. EMI attenuation levels were measured in terms of decibels (dB) before and after each thermal cycling test. The specimens were measured in the frequency range of 8.2 GHz – 12.4 GHz (X-band) and the average values presented are over the entire frequency range. An individual thermal cycle consisted of a 10 second soak at +60 °C directly pursued by a 10 second soak at -60 °C for a total soak time of 20 seconds. Table 1 in section 3.5 discloses the thermal cycling for all four specimens and Figure 29 indicates the EMI shielding performance prior to and during the course of all thermal cycling tests. Figure 30 establishes the position that thermal cycling had a negligible effect on the EMI shielding performance on all four designs, especially for the designs containing CNTs. The bottom graph in Figure 30 illustrates more clearly how the 8G design had a range of nearly 7% in EMI attenuation levels versus the 4% for the 4G/4CNT, 3% for the 2CNT/4G/2CNT, and 3.4% for the (G/CNT)₄ design. The 2CNT/4G/2CNT design had the highest EMI attenuation level and had the smallest range of EMI attenuation values for all four specimens.

The minimal effects of thermal cycling were attributed to Astroquartz II's S-glass having favorable thermal properties such as a near zero thermal linear expansion coefficient of $1.6\text{E-}6 \text{ cm}\cdot^\circ\text{C} / \text{cm}$, thermal conductivity of $1.38 \text{ W/m}\cdot\text{k}$ @ 20 °C, and specific heat of 0.176 @ 72 °C [9]. Experimentally measured thermal conductivities from previous studies of MWNTs were $600\pm100 \text{ W/m}\cdot\text{k}$ for single, high-density

structures to 150 ± 15 W/m·k for bundles of MWNTs [1]. These combined thermal properties resulted in a material that offers thermal stability and great

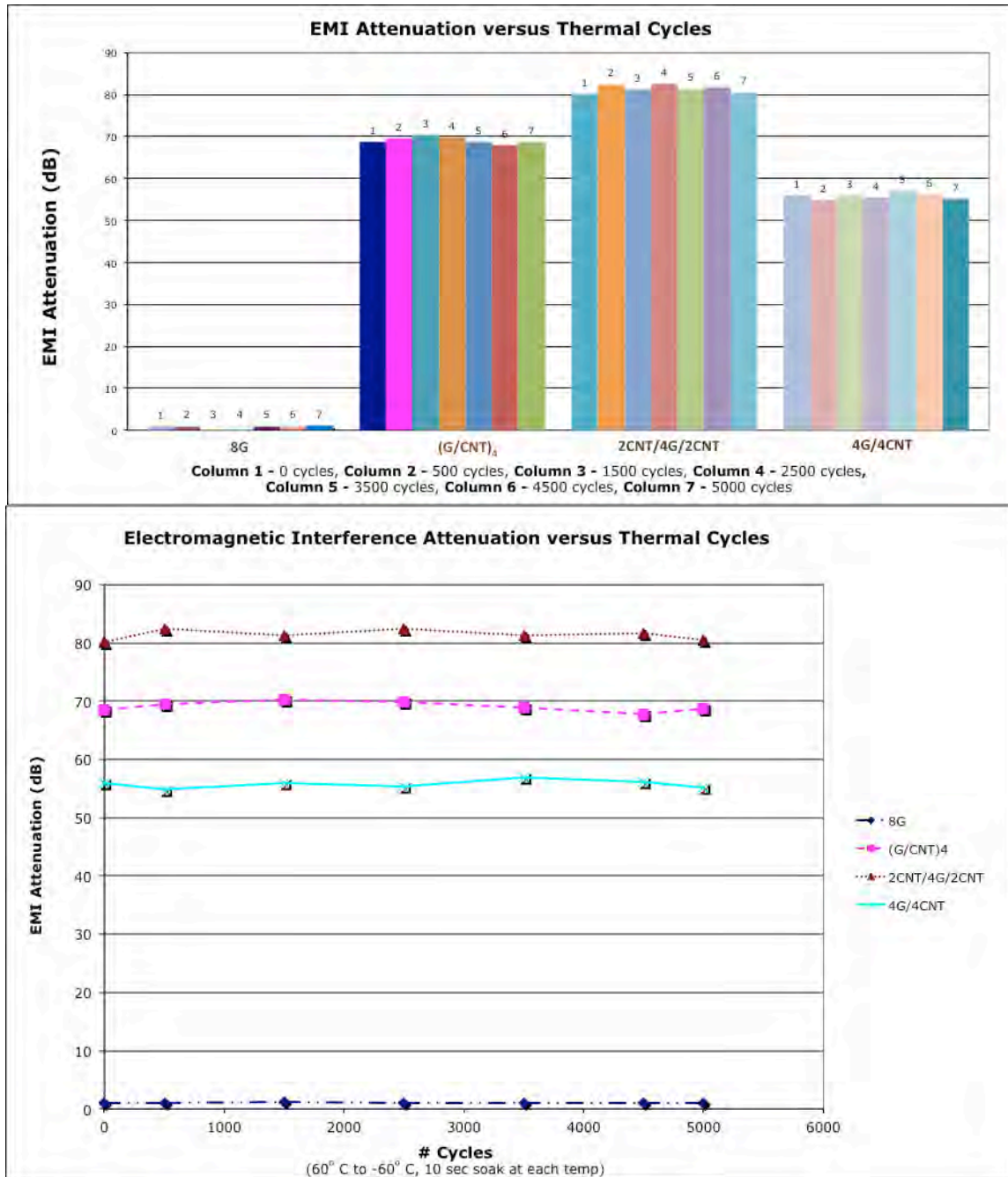


Figure 29. EMI attenuation versus thermal cycles for Group 2

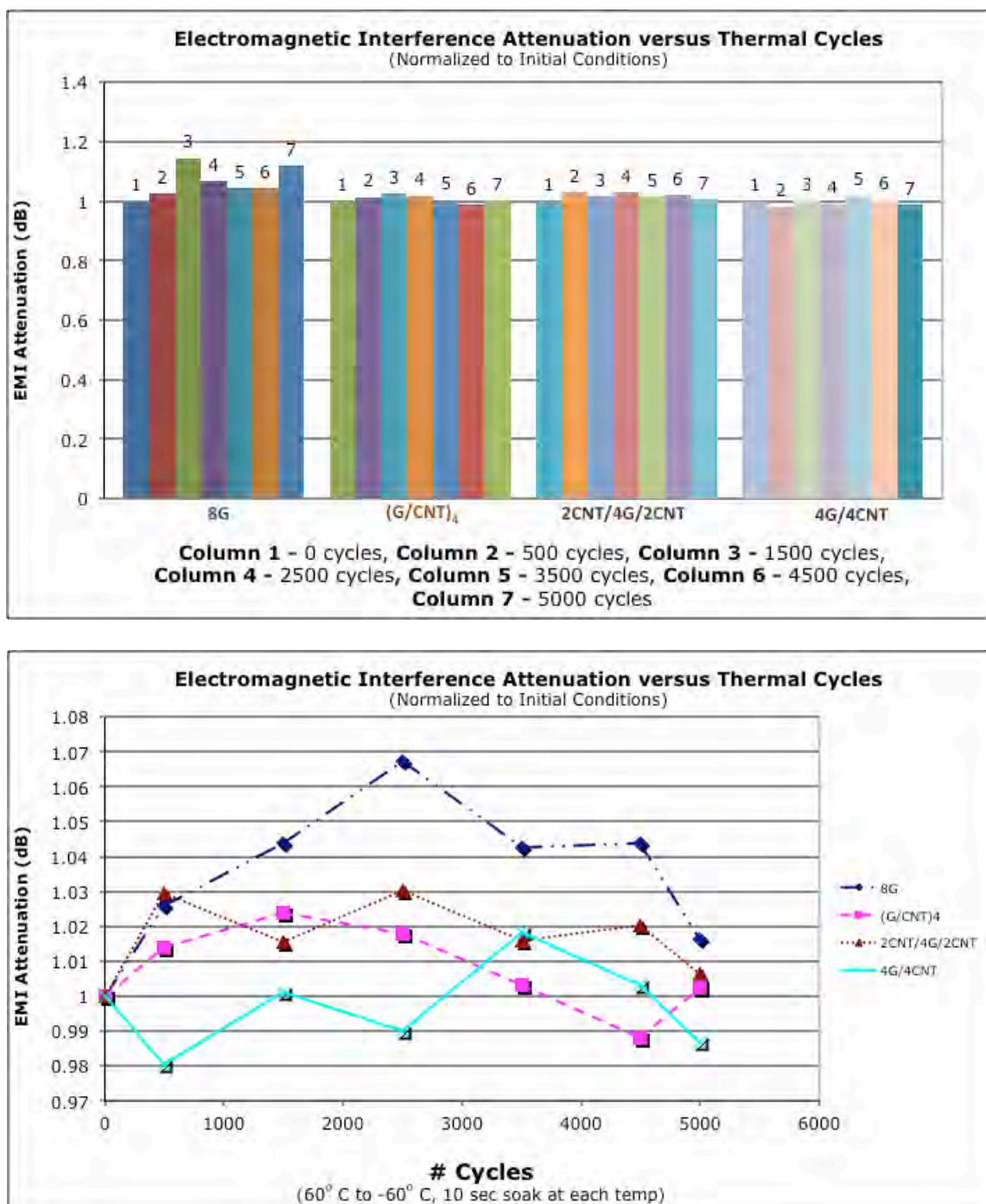


Figure 30. EMI attenuation versus thermal cycles normalized to initial conditions

resistance to thermal shock making it suitable for environments with abrupt thermal variations such as space.

Monotonic tension tests commenced for Group 2 upon finishing the thermal cycling tests. EMI attenuation levels were measured in terms of decibels (dB) before and after each monotonic tension test. The specimens were measured in the frequency range of 8.2 GHz – 12.4 GHz (X-band) and the average values presented are over the entire frequency range. Monotonic tension tests were performed in the following increments for all four specimens: 25% UTS, 50% UTS, 75% UTS, 95% UTS, up to ultimate failure. Percent UTS numbers were derived from the fracture values obtained from Group 1.

Table 5. Group 2 – Thermal cycles with corresponding EMI attenuation

# Cycles	8G	(G/CNT) ₄	2CNT/4G/2CNT	4G/4CNT
0	0.985868251	68.6203127	80.053398	55.978363
500	1.011536812	69.5811814	82.42021306	54.88233229
1500	1.128952096	70.26126635	81.28550517	56.03569578
2500	1.052333143	69.85076837	82.49047083	55.41418434
3500	1.027939389	68.83376183	81.34032533	57.00705341
4500	1.029146897	67.79984434	81.6630815	56.16146253
5000	1.102022637	68.78130185	80.54868645	55.25050152

8G had the highest stress value and fractured at 515.61MPa (74.78 ksi). 4G/4CNT fractured at a stress value of 410.81 MPa (59.58 ksi), 2CNT/4G/2CNT had the lowest stress value and fractured at 377.79 MPa (54.79 ksi), and (G/CNT)₄ fractured at a stress value of 487.21 MPa (70.66 ksi). Table 6 and Figure 31 provide a summary of the fracture values recorded for Group 1 and Group 2.

Table 6. Fracture values for Group 1 and Group 2

Configuration	Group 1	Group 2	% Change
8G	543.99 MPa (78.9 ksi)	515.61MPa (74.78 ksi)	-5.22%
4G/4CNT	409.89 MPa (59.45 ksi)	410.81 MPa (59.58 ksi)	+0.22%
2CNT/4G/2CNT	373.61 MPa (54.19 ksi)	377.79 MPa (54.79 ksi)	+1.12%
(G/CNT)₄	500 MPa (72.52 ksi)	487.21 MPa (70.66 ksi)	-2.56%

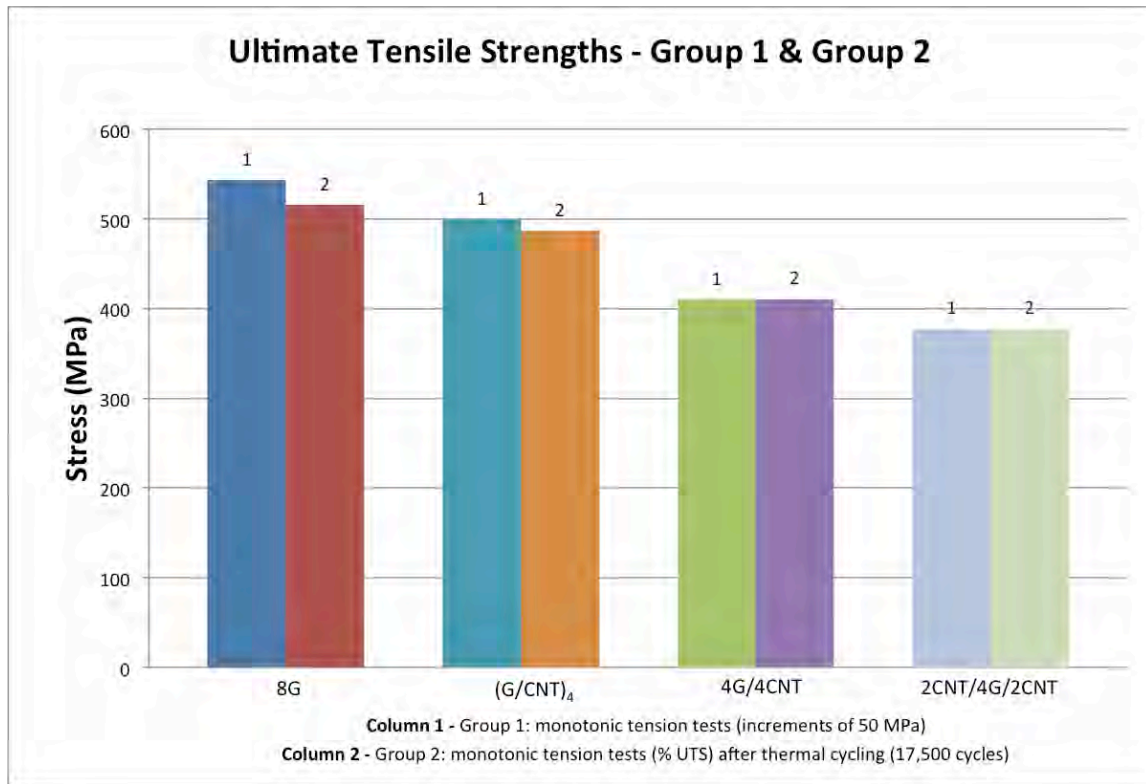


Figure 31. Fracture values for Group 1 and Group 2

Experimental error unavoidably injects itself into this study by the simple, inherent variability between test equipment and materials, however, a well-known problem comes into play when researching the characteristics of nanocomposites. The

inability to uniformly disperse and distribute CNTs in polymer matrices remains a challenging problem and considerably affects the behavior of nanocomposites. This alone could account for any shift in measurements made during the course of this research.

EMI attenuation levels were measured in terms of decibels (dB) before and after each monotonic tension test for Group 2. The specimens were measured in the frequency range of 8.2 GHz – 12.4 GHz (X-band) and the average values presented are over the entire frequency range. Figure 32 displays how the EMI attenuation values for all four specimens decreased with increasing tensile load prior to fracture and demonstrates that the 2CNT/4G/2CNT design was superior to the 4G/4CNT and (G/CNT)₄ designs, which matches the results from Group 1. EMI measurements were also taken after each specimen fractured in the region that remained intact and the results for Group 1 and Group 2 are summarized in Table 7. The reduction in EMI shielding performance from Group 2's initial conditions to post-fracture were 16.44% for 8G, 2.14% for 4G/4CNT, 6.2% for 2CNT/4G/2CNT, and 5.49% for (G/CNT)₄. Figure 33 provides the EMI attenuation data for Group 2 normalized to each specimen's initial conditions and illustrates the degree of EMI shielding performance retained up to fracture. The 2CNT/4G/2CNT design possessed the highest level of EMI attenuation prior to tensile loading. The 2CNT/4G/2CNT design also had the lowest UTS value of 377.79 MPa (54.79 ksi) amid all four configurations. Group 2 results placed the 2CNT/4G/2CNT design as the best performer in EMI SE and with the lowest UTS value, which matches the results from Group 1. The 8G design had the highest UTS of 515.61MPa (74.78 ksi)

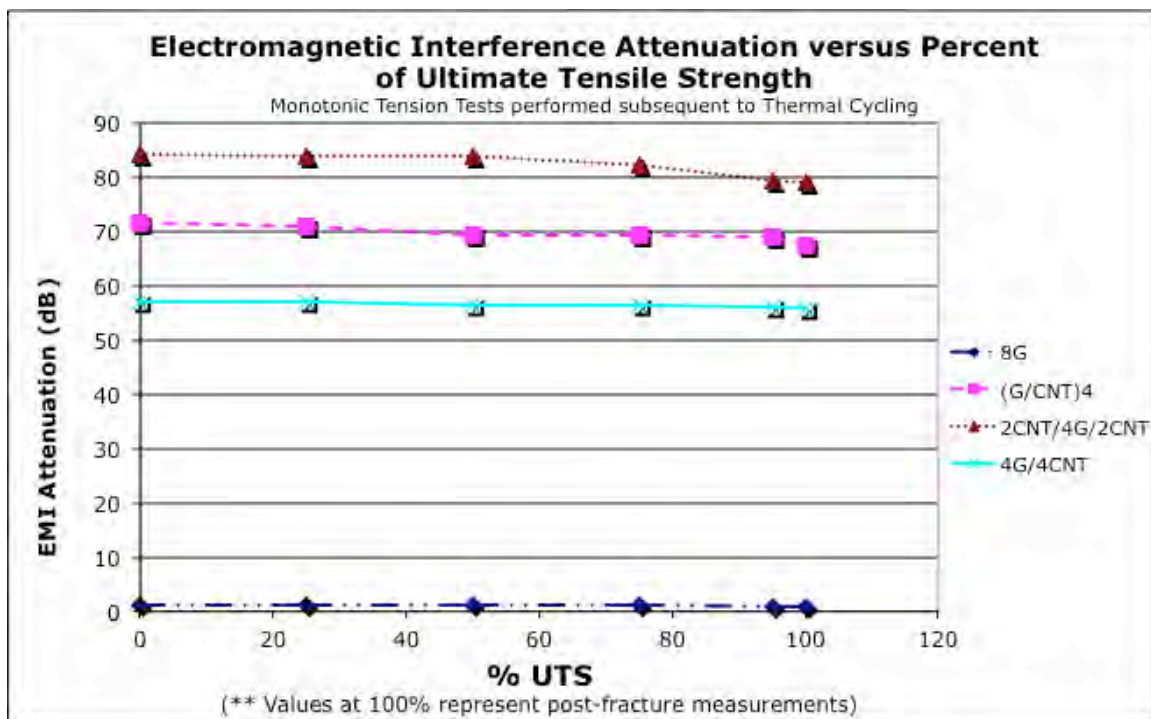
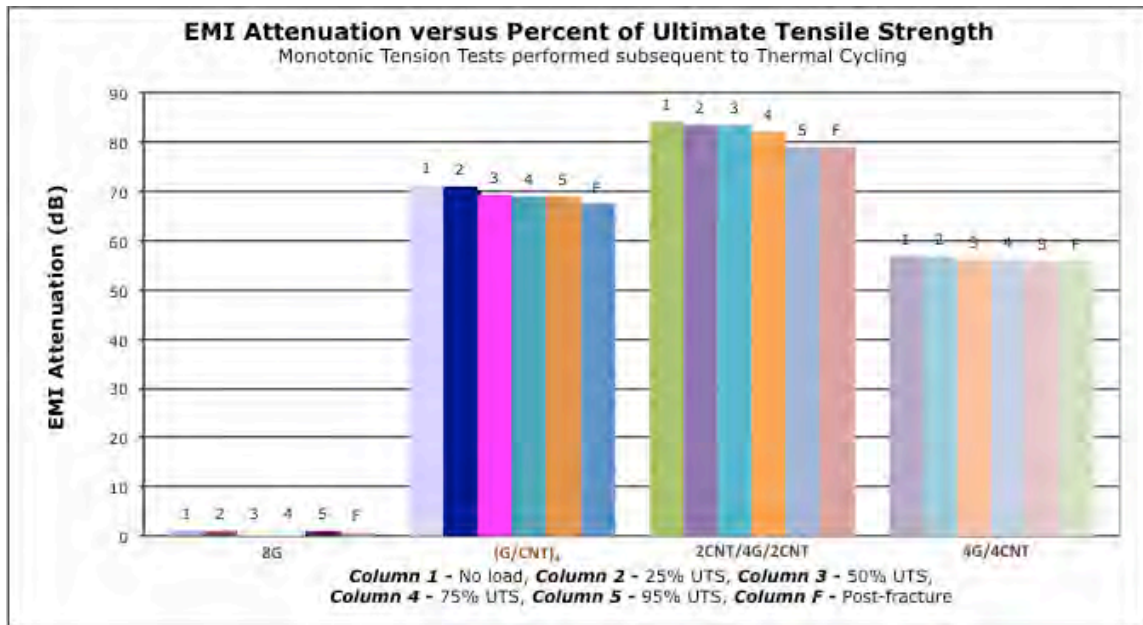


Figure 32. EMI attenuation data for Group 2

yielding a difference of 137.82 MPa (20.08 ksi) between the highest and lowest UTS values for Group 2.

Table 7. Group 2 – % UTS with corresponding EMI attenuation

% UTS	8G	(G/CNT)₄	2CNT/4G/2CNT	4G/4CNT
0	1.093724759	71.38616375	84.153729	57.036253
25	1.079834491	70.96137645	83.7280027	56.85860644
50	1.046781414	69.27484952	83.71974424	56.318614
75	1.043001081	69.19169062	82.30289982	56.23140334
95	0.95063968	69.01855142	79.1517919	55.9327767
Post-fracture	0.913862	67.467092	78.932824	55.813726

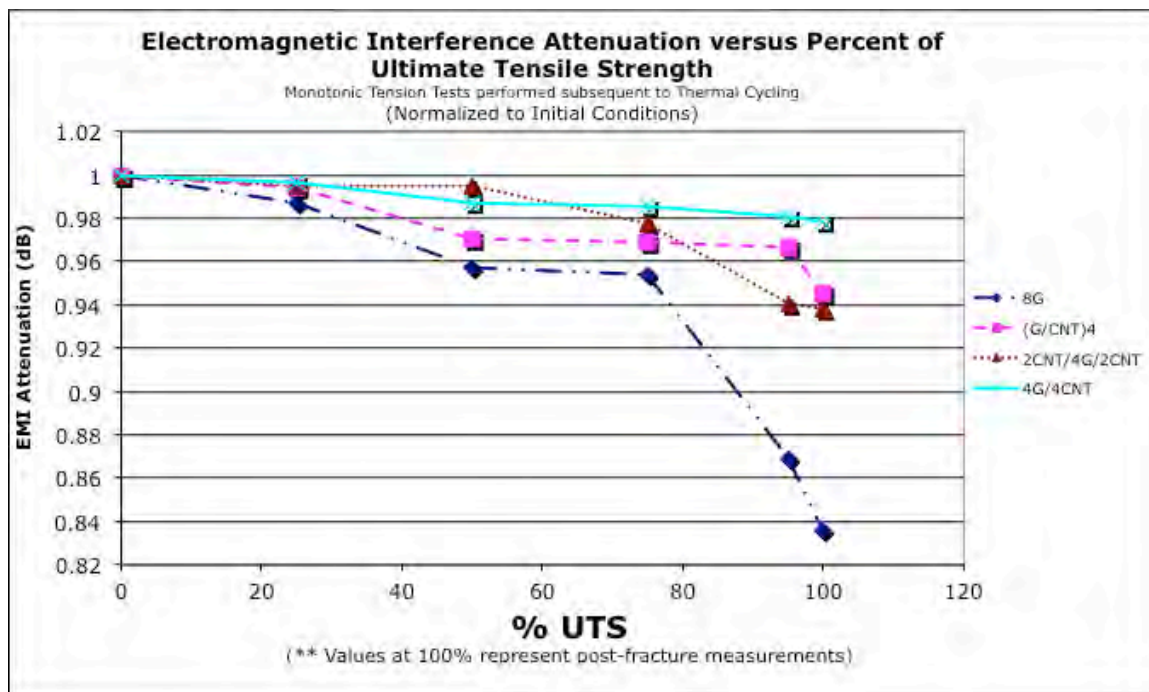
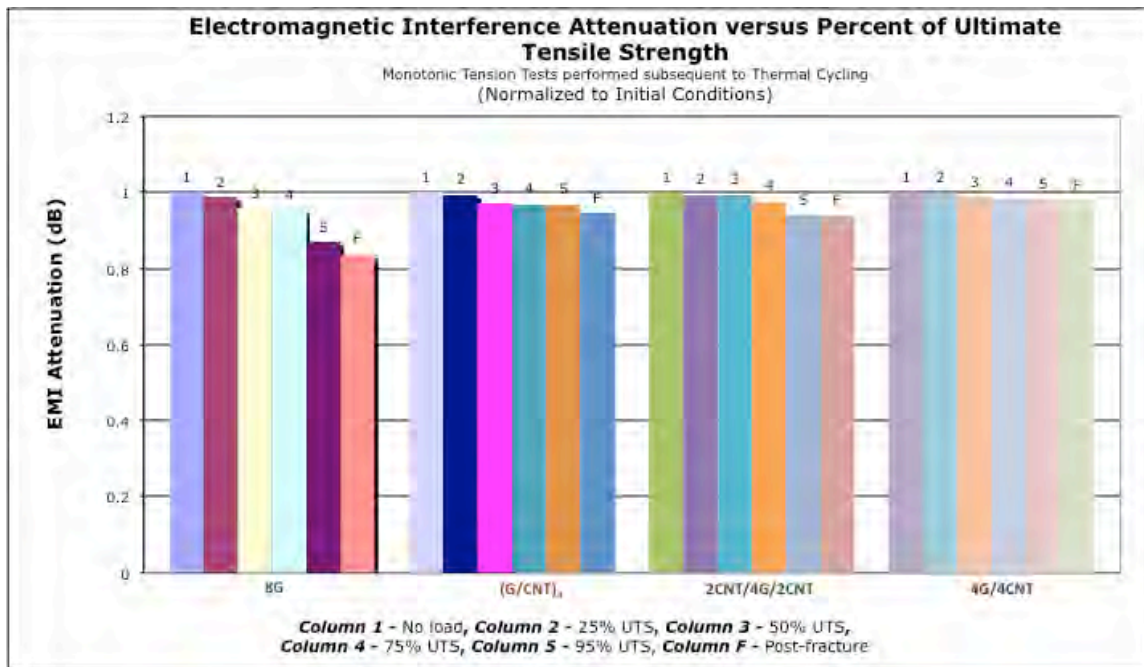


Figure 33. EMI attenuation data normalized to initial conditions for Group 2

4.5 Monotonic Tension – Group 3

The third set of four nanocomposites tested will be referred to as Group 3 and monotonic tension tests were performed in the following increments for all four specimens: 25% UTS, 50% UTS, 75% UTS, 95% UTS, up to ultimate failure. Percent UTS numbers were derived from the averaged fracture values obtained from Group 1 and Group 2.

8G fractured at a stress value of 397.19 MPa (57.61 ksi). 4G/4CNT fractured at a stress value of 376.22 MPa (54.57 ksi), 2CNT/4G/2CNT fractured at a stress value of 363.09 MPa (52.66 ksi), and (G/CNT)₄ fractured at a stress value of 348.32 MPa (50.52 ksi). Table 8 and Figure 34 provide a summary of the fracture values recorded for Groups 1 – 3. The noticeable decrease in UTS values for Group 3's 8G and (G/CNT)₄

Table 8. Fracture values for Groups 1 – 3

Configuration	Group 1	Group 2	Group 3
8G	543.99 MPa (78.9 ksi)	515.61MPa (74.78 ksi)	497.19 MPa (57.61 ksi)
4G/4CNT	409.89 MPa (59.45 ksi)	410.81 MPa (59.58 ksi)	376.22 MPa (54.57 ksi)
2CNT/4G/2CNT	373.61 MPa (54.19 ksi)	377.79 MPa (54.79 ksi)	363.09 MPa (52.66 ksi)
(G/CNT)₄	500 MPa (72.52 ksi)	487.21 MPa (70.66 ksi)	448.32 MPa (50.52 ksi)

configurations were more than likely caused by a modification to the MTS 810 wedge grips. All monotonic tensions tests performed utilized roughened wedge grips, however, both the 8G and (G/CNT)₄ specimens for Group 3 had serrated action wedge grips during the sixth monotonic tension test that went to ultimate failure. Serrated action wedge grips introduce stress inhomogeneities, which further compounds existing damage within a

composite's microvolumes leading to premature failure [5]. Both the 8G and (G/CNT)₄ specimens for Group 3 successfully tested at 95% UTS, but failed to reach 95% UTS during their final tensile loading up to ultimate failure.

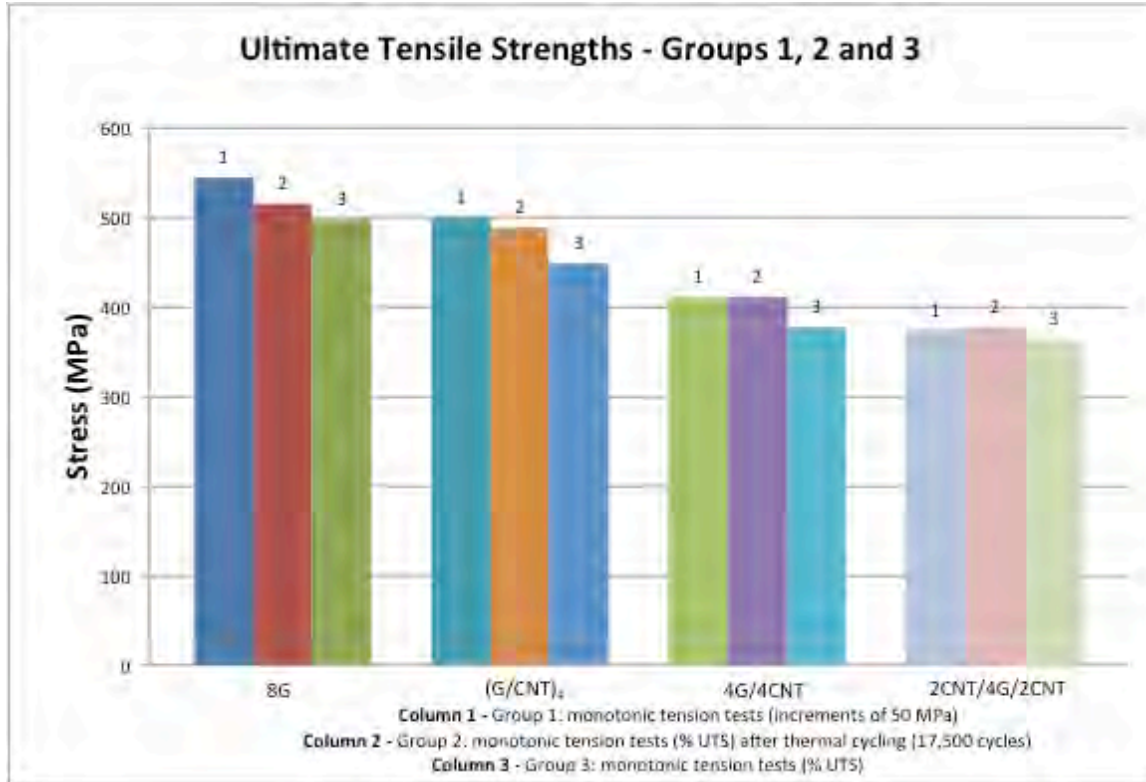


Figure 34. Fracture values for Groups 1 – 3

EMI attenuation levels were measured in terms of decibels (dB) before and after each monotonic tension test. The specimens were measured in the frequency range of 8.2 GHz – 12.4 GHz (X-band) and the average values presented are over the entire frequency range. Figure 35 displays how the EMI attenuation values for all four specimens decreased with increasing tensile load prior to fracture and demonstrates that the 2CNT/4G/2CNT design was superior to the 4G/4CNT and (G/CNT)₄ designs thus matching the results from Group 1 and Group 2. EMI measurements were also taken

after each specimen fractured in the region that remained intact and the results are summarized in Table 9 for Groups 1, 2 and 3. The reduction in EMI shielding

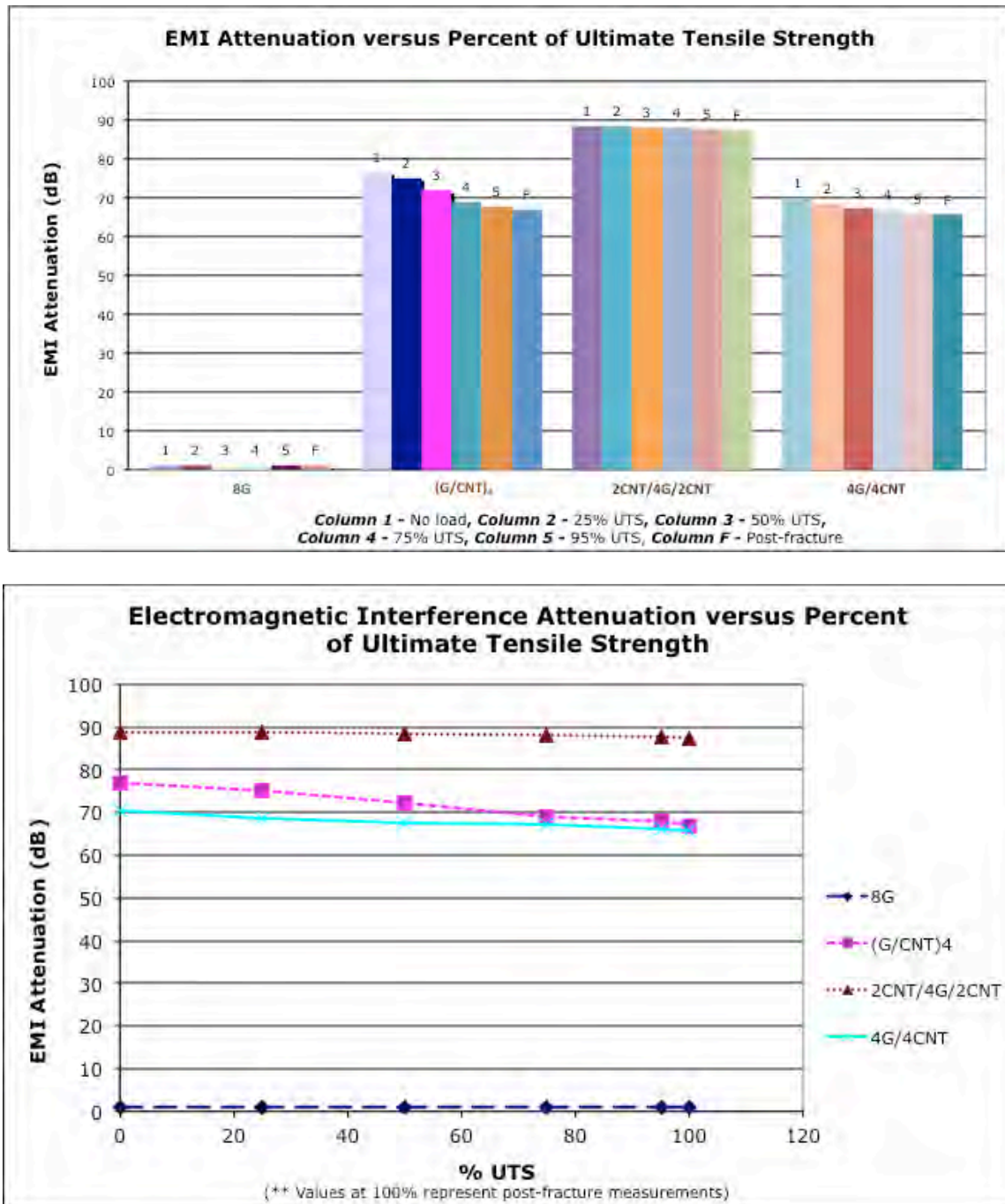


Figure 35. EMI attenuation data for Group 3

Table 9. Group 3 – % UTS with corresponding EMI attenuation

% UTS	8G	(G/CNT) ₄	2CNT/4G/2CNT	4G/4CNT
0	1.119199234	76.861548	88.5682423	70.24256039
25	1.103887972	75.178025	88.56465629	68.62776911
50	1.10182107	72.068247	88.30309166	67.50207646
75	1.078194286	69.130151	88.08599769	67.14916603
95	1.072492751	67.882413	87.8259151	66.02116579
Post-fracture	1.052463	66.935362	87.374283	65.729433

performance from each specimen's initial conditions to post-fracture were 5.96% for 8G, 6.43% for 4G/4CNT, 1.35% for 2CNT/4G/2CNT, and 12.91% for (G/CNT)₄. Figure 36 provides the EMI attenuation data normalized to each specimen's initial conditions and illustrates the degree of EMI shielding performance retained up to fracture. The 2CNT/4G/2CNT design possessed the highest level of EMI attenuation prior to tensile loading and had the smallest degree of dB loss up to and after fracture. However, the 2CNT/4G/2CNT design had the lowest UTS value of 363.09 MPa (52.66 ksi) amid all four configurations.

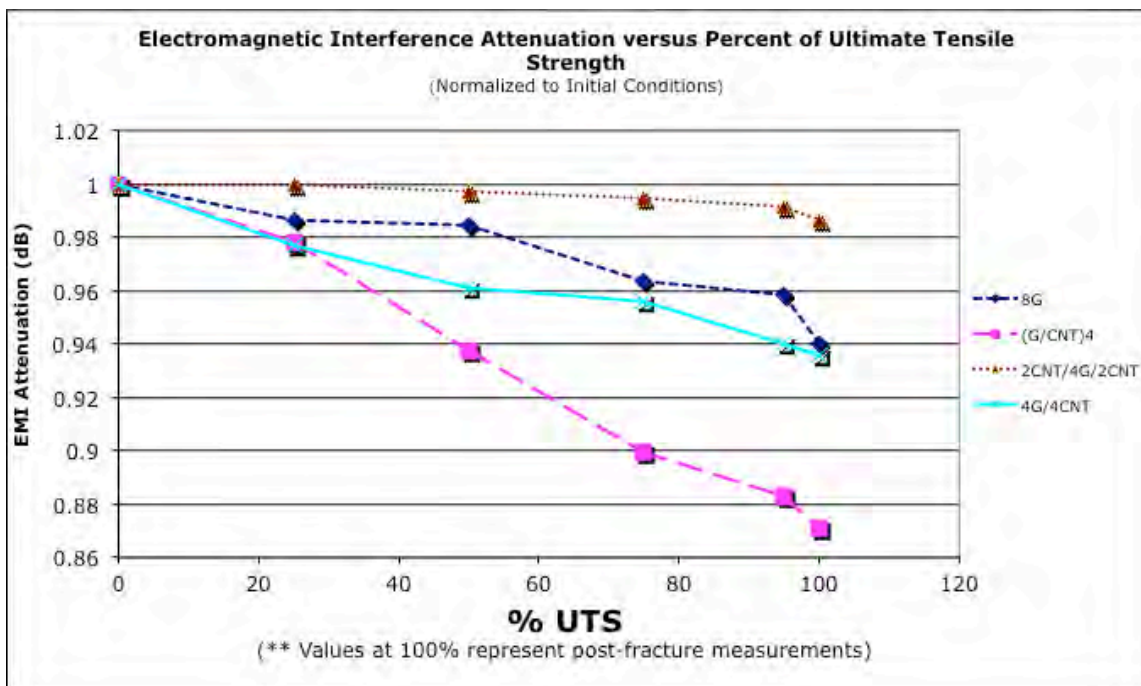
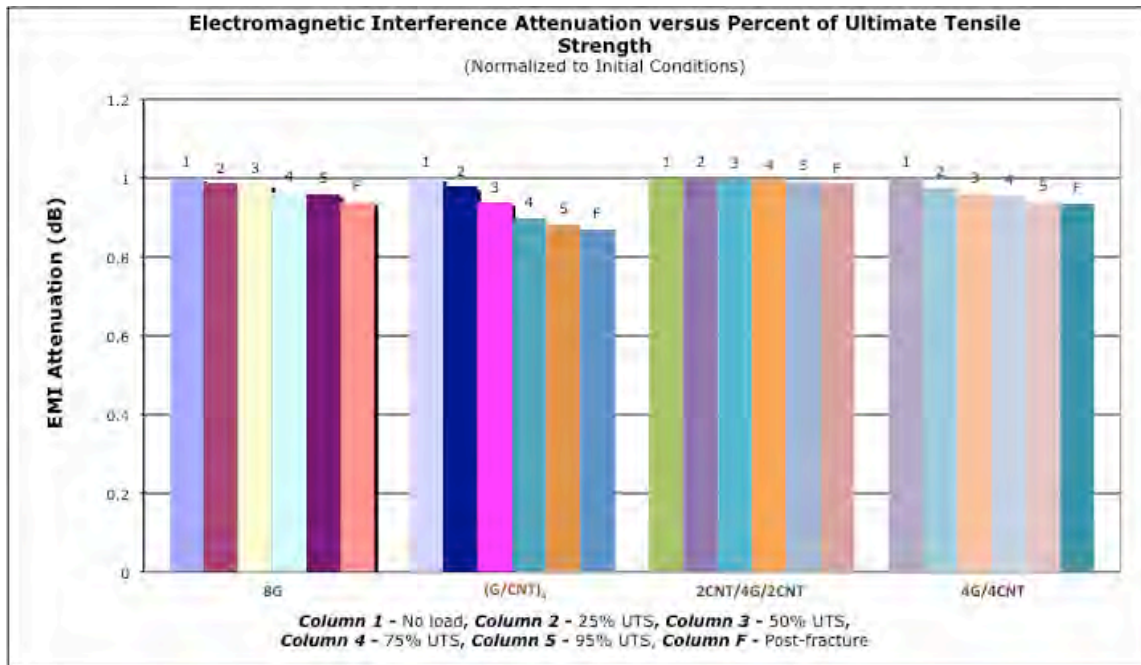


Figure 36. EMI attenuation data normalized to initial conditions for Group 3

4.5 Failure Mechanisms

Failure mechanisms were examined with an optical microscope and a scanning electron microscope (SEM) in order to ascertain the various failure modes among the four nanocomposite designs. Failure modes were analyzed because of placing each specimen under monotonic tensile loading. All twelve specimens exhibited failure in the same region for all three groups. Specifically, on the right half as shown in Figure 37. The glass/epoxy tabs on the right side of Figure 37 were all placed in the lower grip of the MTS machine. This investigation commenced by employing the optical microscope to observe failure mechanisms within the 8G control design. The control specimen was an 8-ply, 3-harness satin weave, Astroquartz II (S-glass) fabric with Cycom 5575-2 cyanate ester prepreg resin, and did not contain CNT plies.

It has long been recognized that transverse matrix cracking is the first damage mode observed in composite laminates under static tensile loading. It does not necessarily result in the immediate catastrophic failure of the laminate, but does trigger the development of other harmful resin-dominated damage modes such as edge and local delaminations. In addition, the transverse matrix cracking causes stiffness reduction and is extremely detrimental to the strength of the laminate. The delaminations can cause fibre-breakage in the primary load bearing plies, which accelerates the progression to ultimate failure [10]. Figures displaying thickness views in this section have a legend located on the left side to illustrate the orientation of the ply in degrees. Figures 38 and 39 validate the aforementioned by providing evidence of failure progression for the control specimen in thickness views at 100x and 12x, respectively.

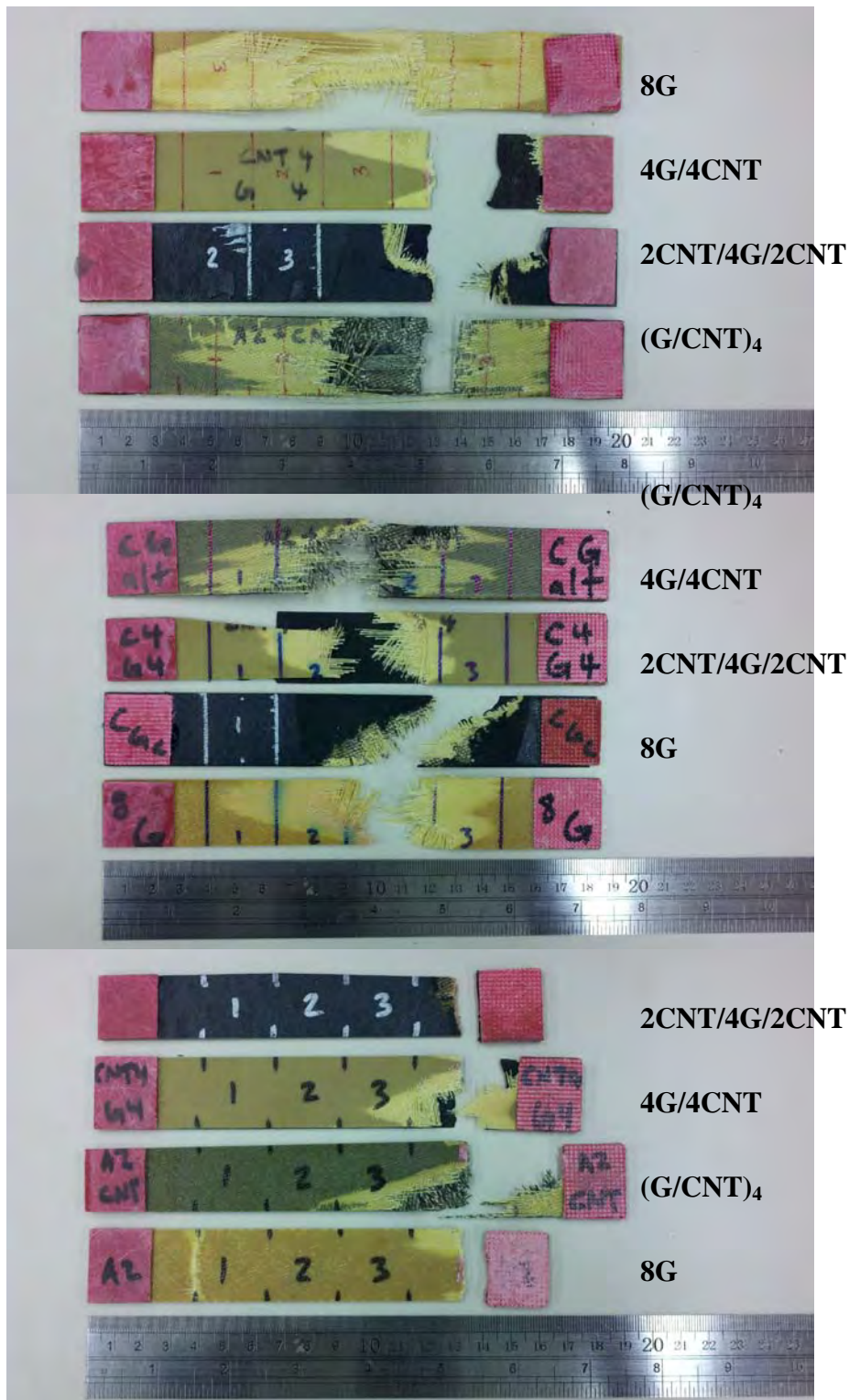


Figure 37. Specimens after fracture: top – Group 1, middle – Group 2, bottom – Group 3

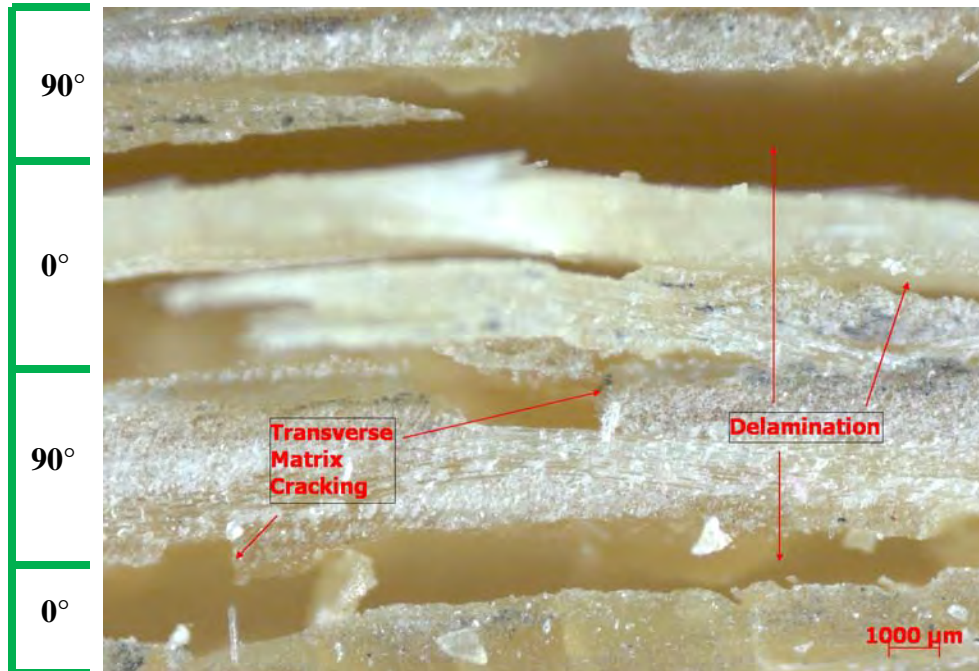


Figure 38. Fractured 8G specimen: thickness view at 100x



Figure 39. Fractured 8G specimen: thickness view at 12x

The origin of failure is the formation of transverse matrix cracks, which instigated delamination and further developed transverse matrix crack formation. This failure progression weakened the specimen leading to ultimate failure. Figure 40 is an SEM image of the 8G specimen giving added evidence to the failure mechanisms previously mentioned.

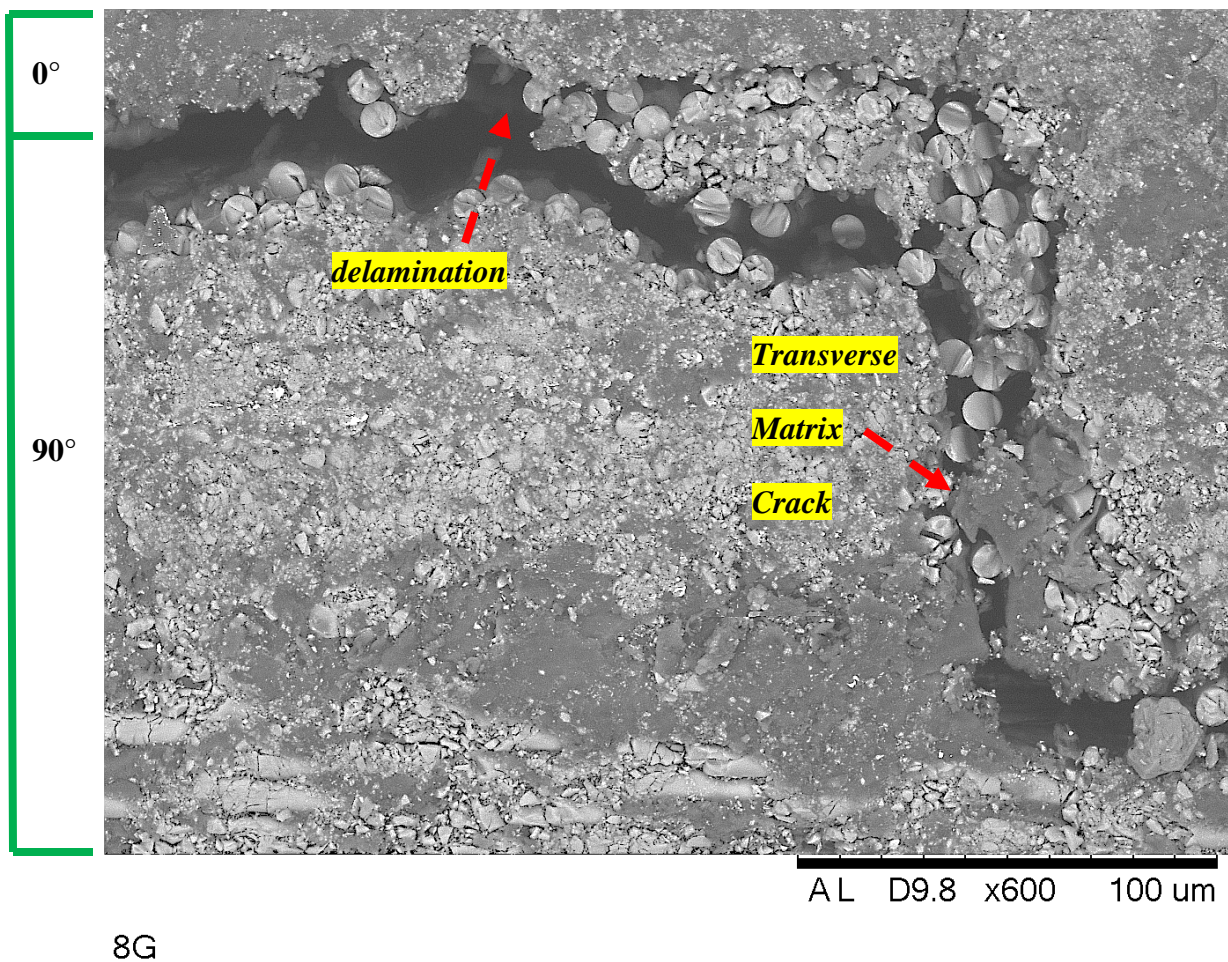


Figure 40. SEM image of 8G: transverse matrix crack and delamination

The second design, 4G/4CNT, had four CNT plies on one side of the specimen with four glass plies on the other half. The CNT plies were a sheet layer that contained no matrix material and solely MWNTs. Figures 41 and 42 show 4G/4CNT thickness views at 100x and 12x, respectively and highlight the same failure progression observed in 8G.

Transverse matrix cracks were created leading to delamination and these promoted further matrix cracking and additional delamination. The CNT plies remained intact after delaminating along the entire length of the specimen. This is an important observation because it provides support of the specimen's ability to effectively shield against EMI after ultimate failure has occurred.

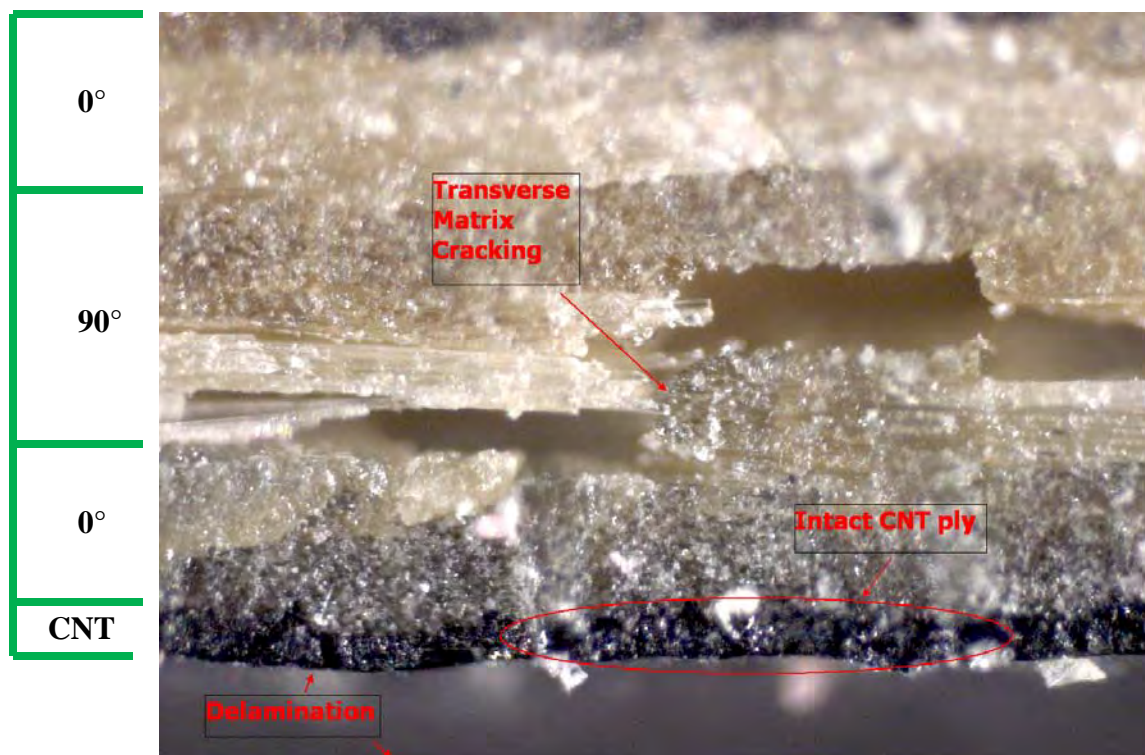


Figure 41. Fractured 4G/4CNT specimen: thickness view at 100x

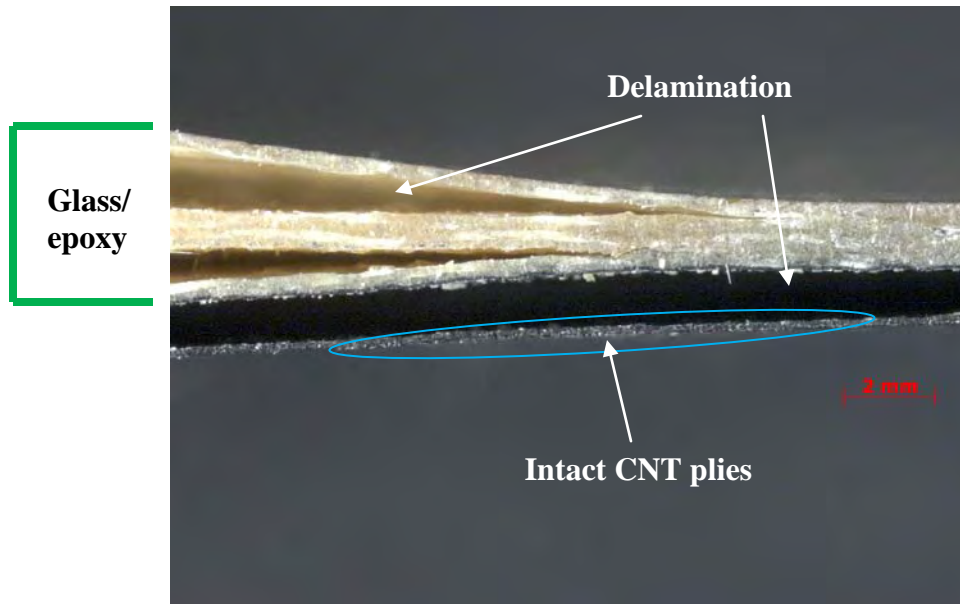


Figure 42. Fractured 4G/4CNT specimen: thickness view at 12x

Figure 43 represents the coordinate system assigned to the nanocomposite specimens with the 1-axis aligned with the longitudinal axis of the laminate. It also describes the orientation of the warp (0°) and fill (90°) strands used to construct the satin weave.

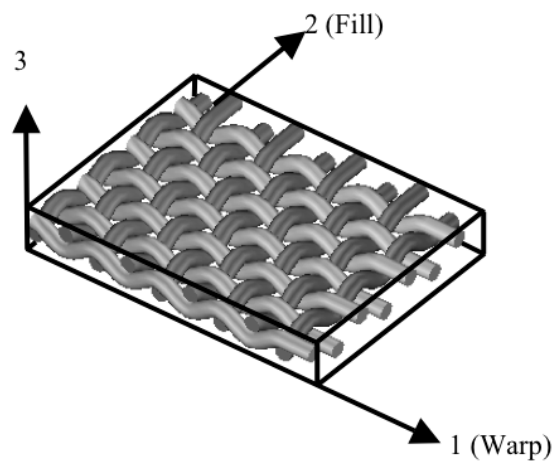


Figure 43. Principal laminate coordinate system

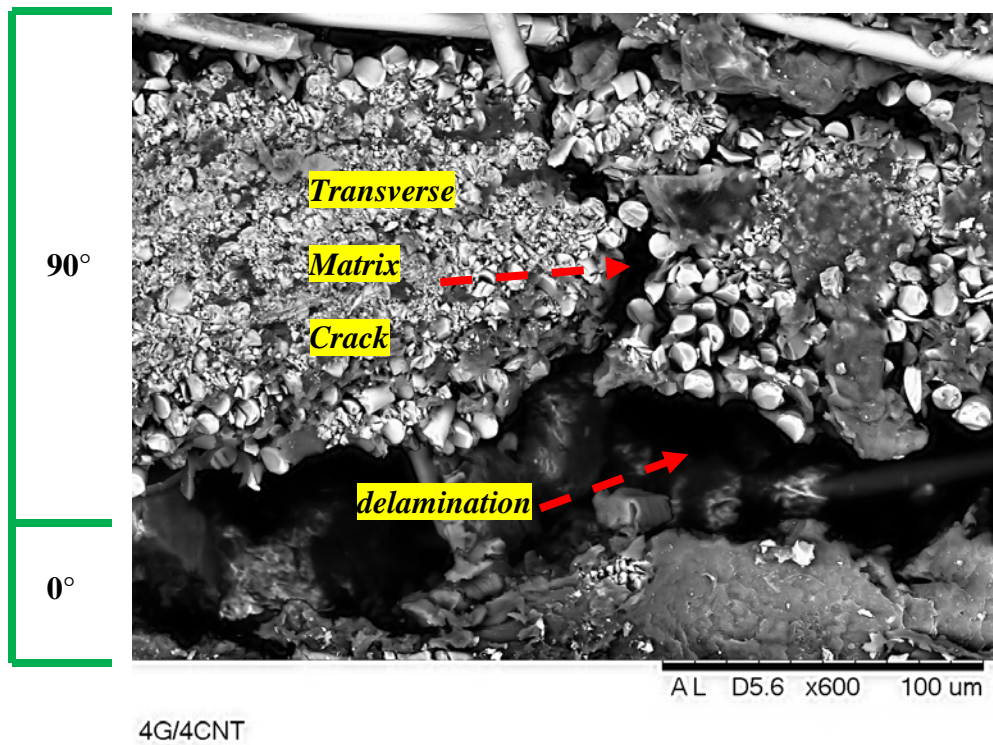


Figure 44. SEM image of 4G/4CNT: transverse matrix crack and delamination

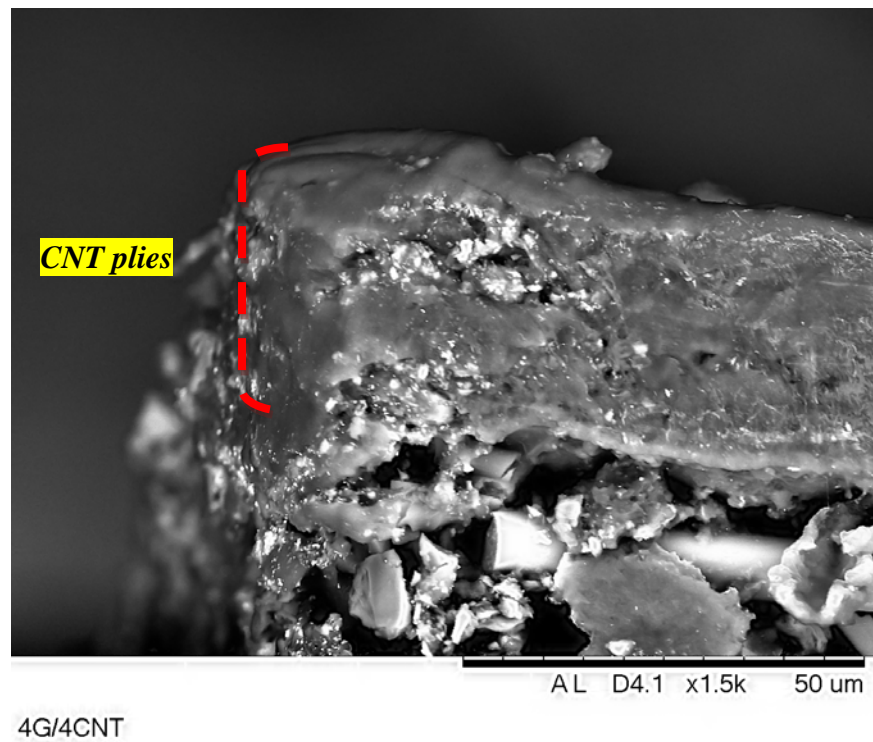


Figure 45. SEM image of 4G/4CNT: intact CNT plies at fracture point

Figures 44 and 45 are SEM images of the 4G/4CNT specimen giving added evidence to the failure mechanisms previously mentioned. The important item to note is that the CNT plies were intact at the point of fracture and the region away from fracture along the entire 1-axis.

The third design, 2CNT/4G/2CNT, had two CNT plies on the exterior of each side with four glass plies in the middle. Figures 46 and 47 present 2CNT/4G/2CNT thickness views at 100x and 12x, respectively and highlight the same failure progression observed in 8G and 4G/4CNT.

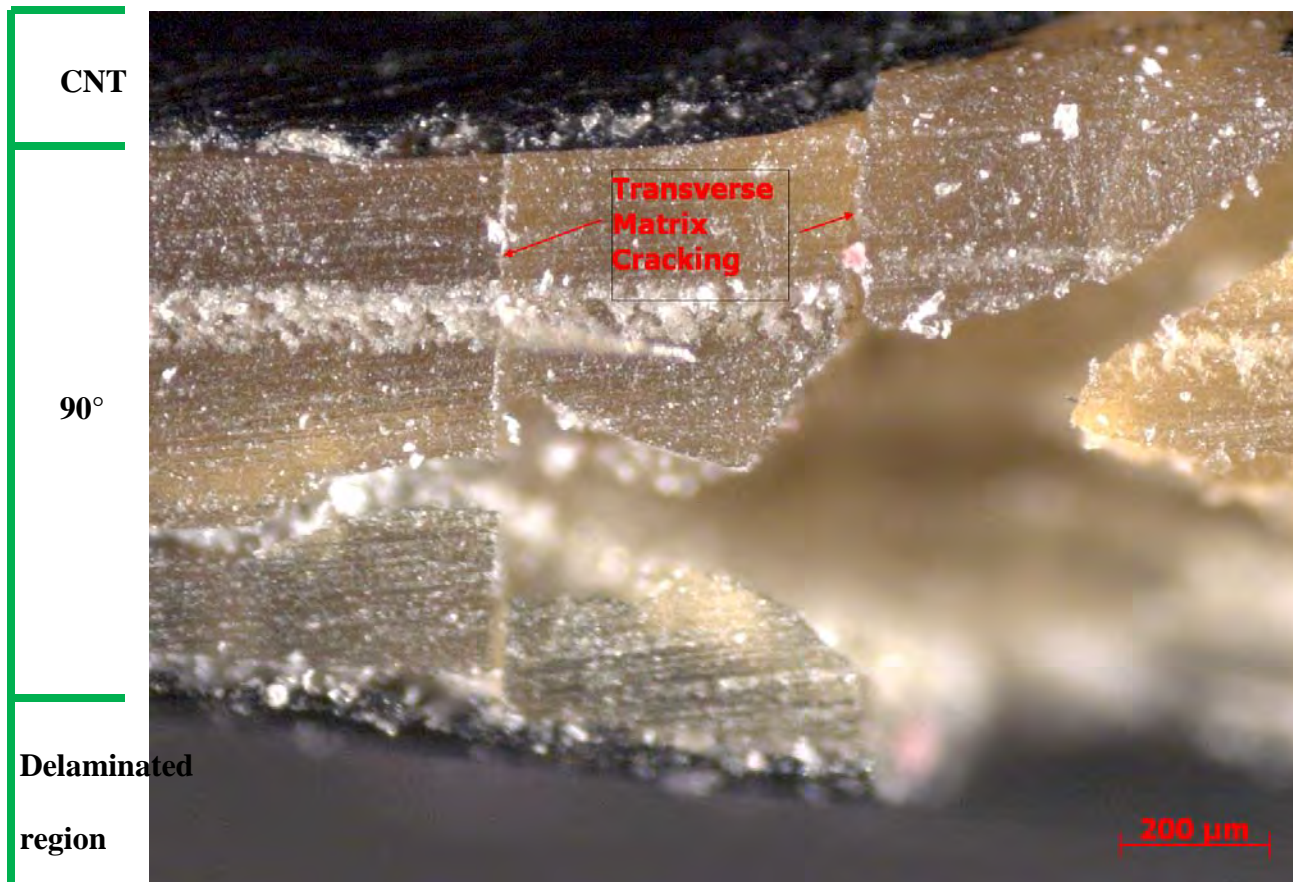


Figure 46. Fractured 2CNT/4G/2CNT specimen: thickness view at 100x

CNT
Glass/
epoxy
CNT

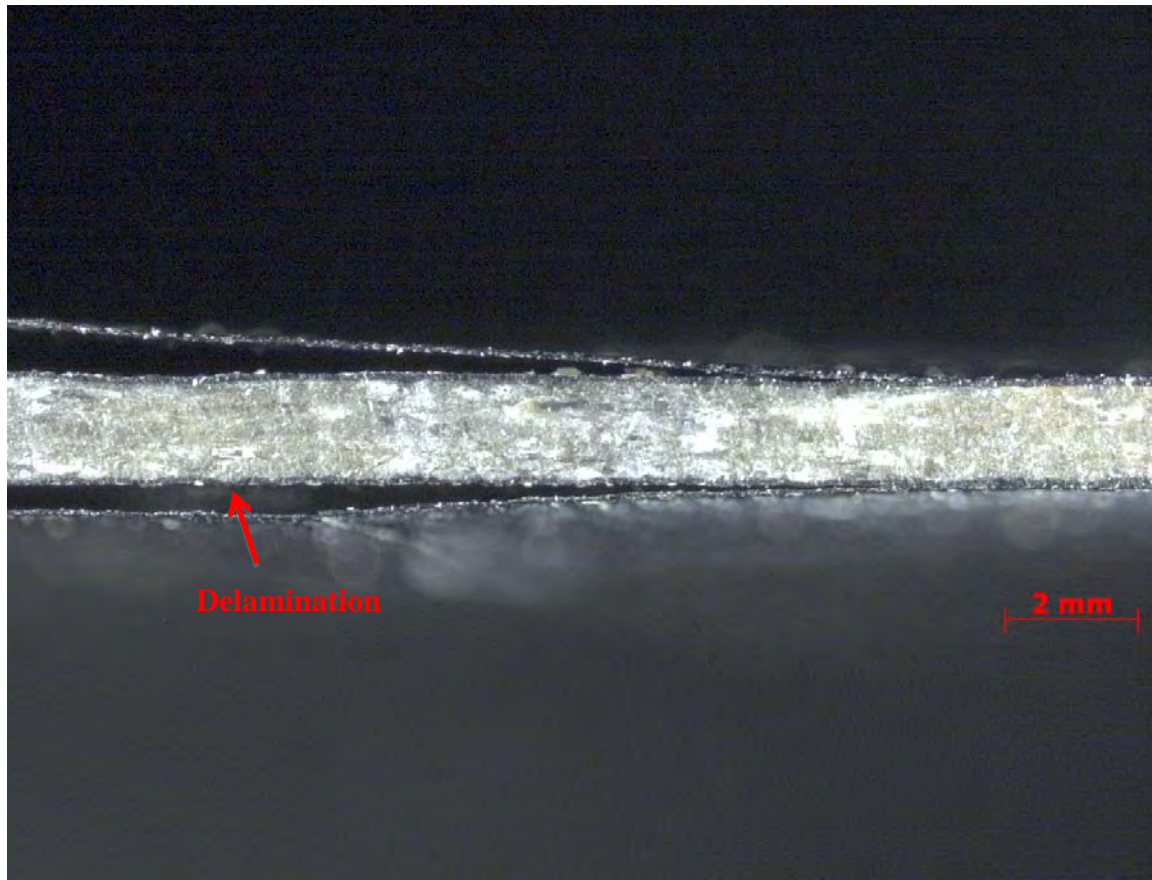


Figure 47. Fractured 2CNT/4G/2CNT specimen: thickness view at 12x

Transverse matrix cracks were created leading to delamination and these promoted further matrix cracking and additional delamination. The CNT plies remained intact after delaminating along the entire 1-axis in the same manner as 4G/4CNT. Figures 48 and 49 are SEM images of the 2CNT/4G/2CNT specimen giving added evidence to the failure mechanisms previously mentioned for 8G and 4G/4CNT. All three designs demonstrated the same failure progression of transverse matrix cracks causing delamination. Increased monotonic tensile loading produced additional transverse matrix cracks, which caused further delamination of multiple CNT plies.

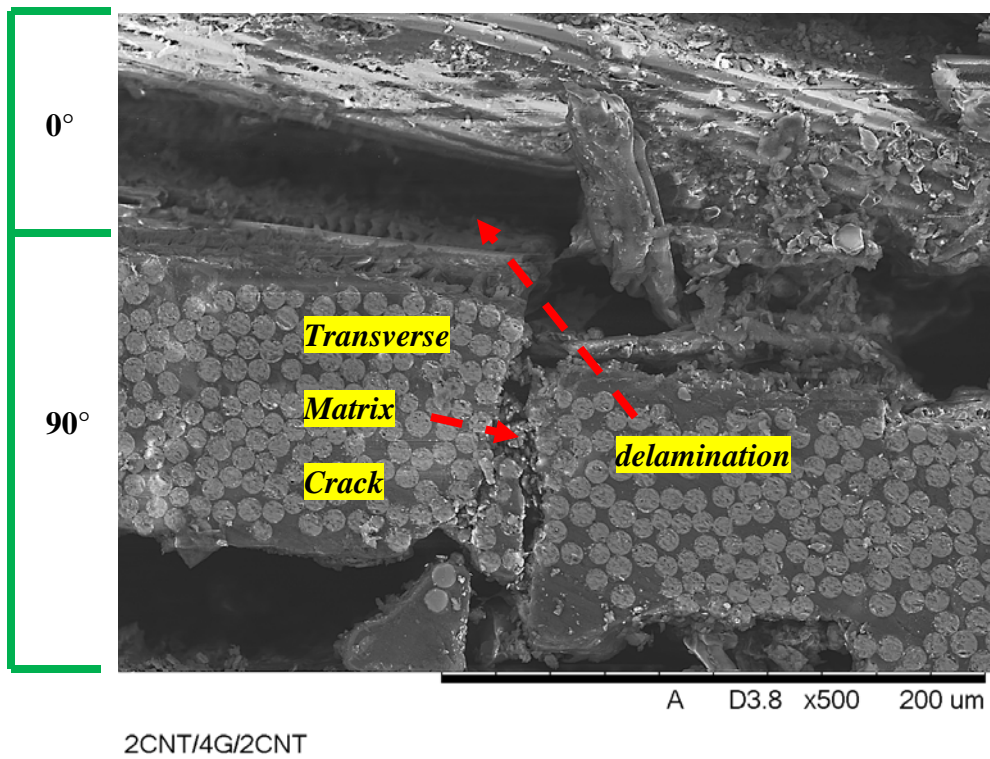


Figure 48. SEM image of 2CNT/4G/2CNT: transverse matrix crack and delamination

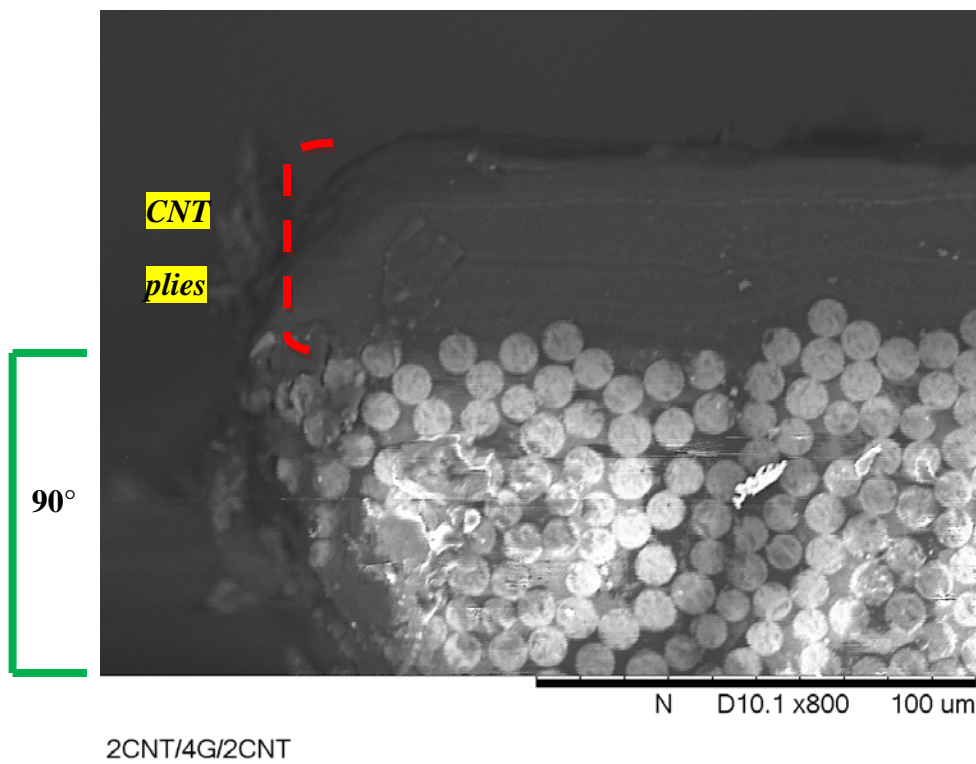


Figure 49. SEM image of 2CNT/4G/2CNT: intact CNT plies at fracture point

Lastly, the fourth design, (G/CNT)₄, had alternating CNT plies and glass fabric plies across the thickness. Figures 50 and 51 illustrate (G/CNT)₄ thickness views at 100x and 12x, respectively and emphasize the same failure progression observed in 8G, 4G/4CNT, and 2CNT/4G/2CNT.

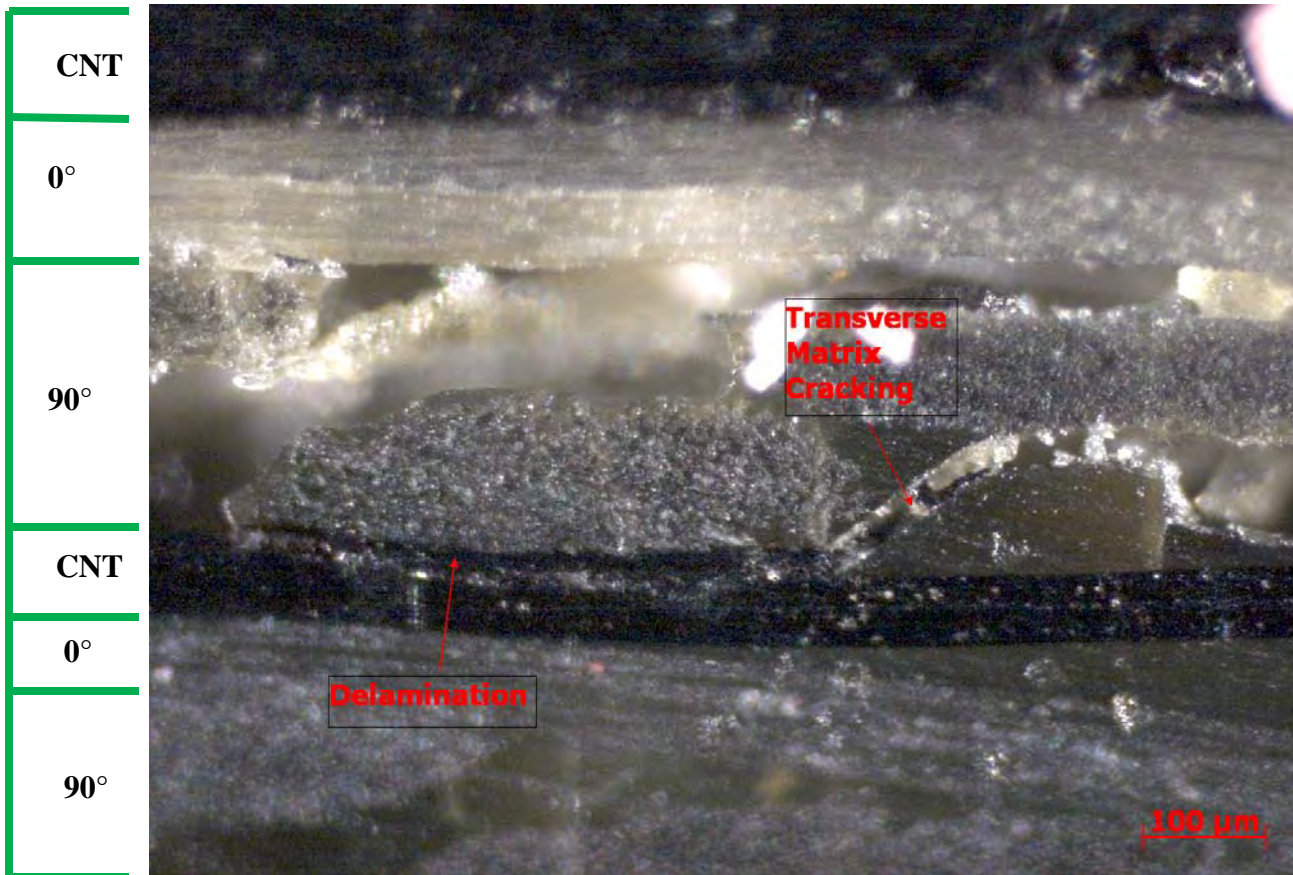


Figure 50. Fractured (G/CNT)₄ specimen: thickness view at 100x

Transverse matrix cracks were created leading to delamination and these promoted further matrix cracking and additional delamination. The CNT plies remained intact after delaminating along the entire 1-axis in the same manner as 4G/4CNT and 2CNT/4G/2CNT. Figures 52 and 53 are SEM images of the (G/CNT)₄ specimen giving added evidence to the failure mechanisms previously mentioned for 8G, 4G/4CNT, and 2CNT/4G/2CNT. All four designs demonstrated the same failure progression of

glass
CNT
glass
CNT
glass
CNT
glass
CNT

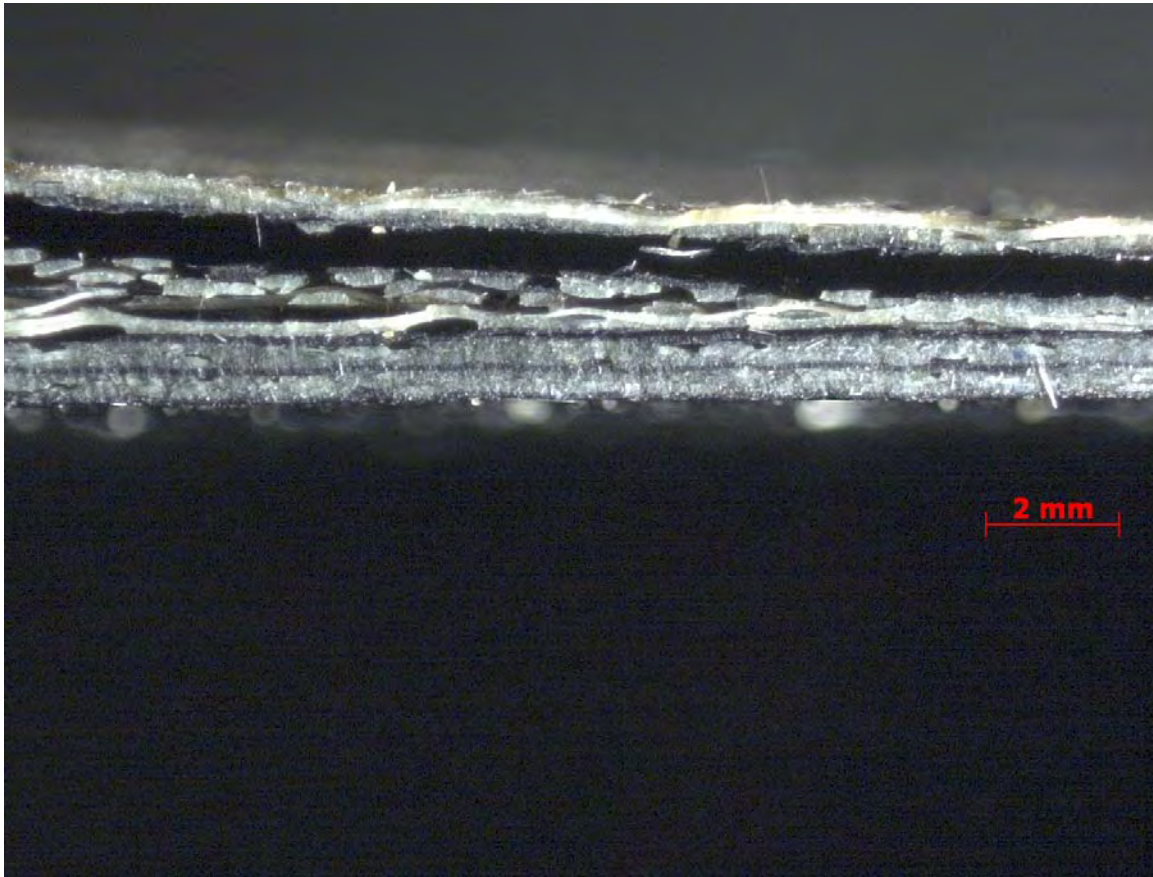


Figure 51. Fractured (G/CNT)₄ specimen: thickness view at 12x

transverse matrix cracks causing delamination. Increased monotonic tensile loading produced additional transverse matrix cracks, which caused further delamination of multiple CNT plies.

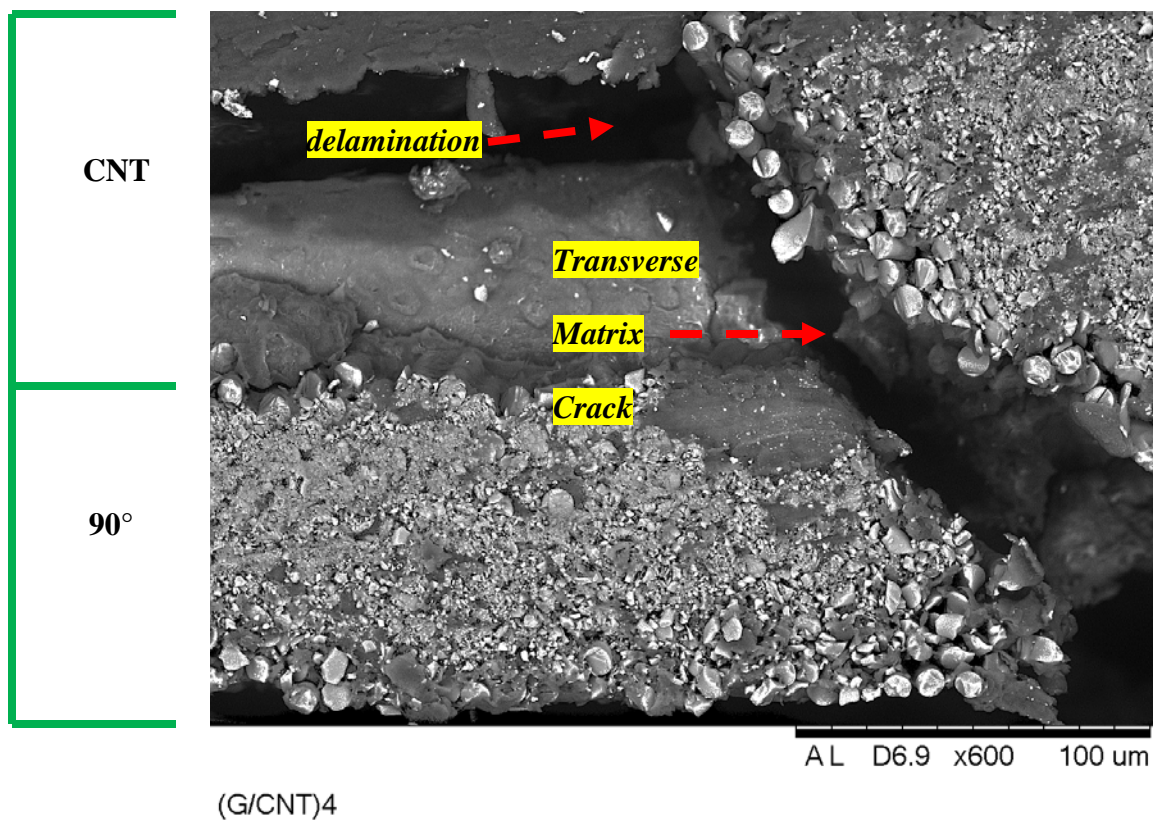


Figure 52. SEM image of (G/CNT)₄: transverse matrix crack and delamination

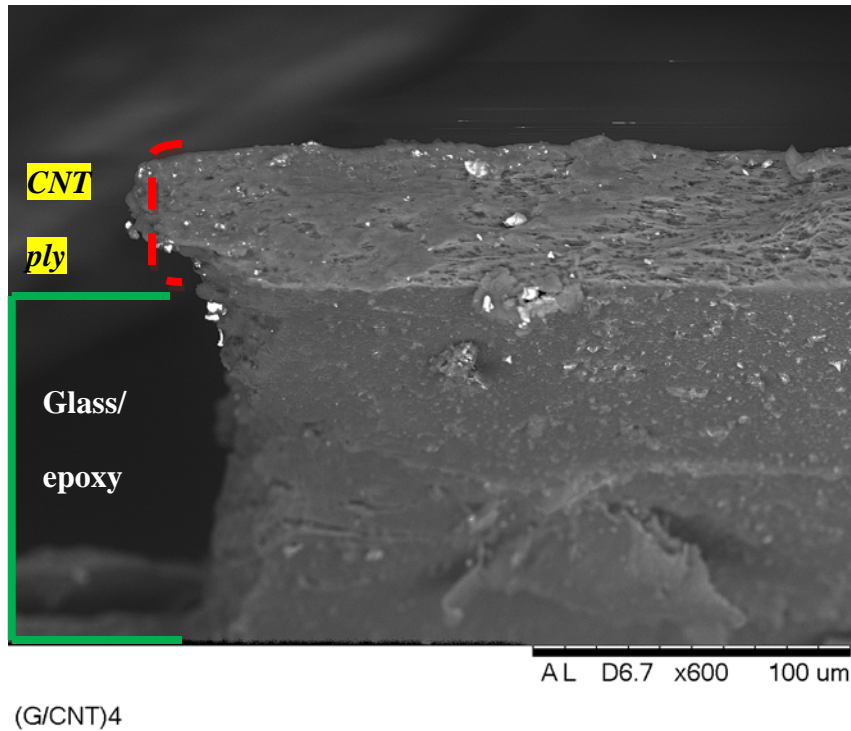


Figure 53. SEM image of (G/CNT)₄: intact CNT plies at fracture point

4.6 Glass Feature

A unique feature is visible when examining the cross-sectional view of the nanocomposites with an optical microscope, which may inadvertently be mistaken for a crack or void. Figure 54 is a cross-sectional view of an 8G specimen where one can witness the numerous transverse lines that were present in all four nanocomposite designs. Figures 55-57 provide verification that these features were not cracks or voids

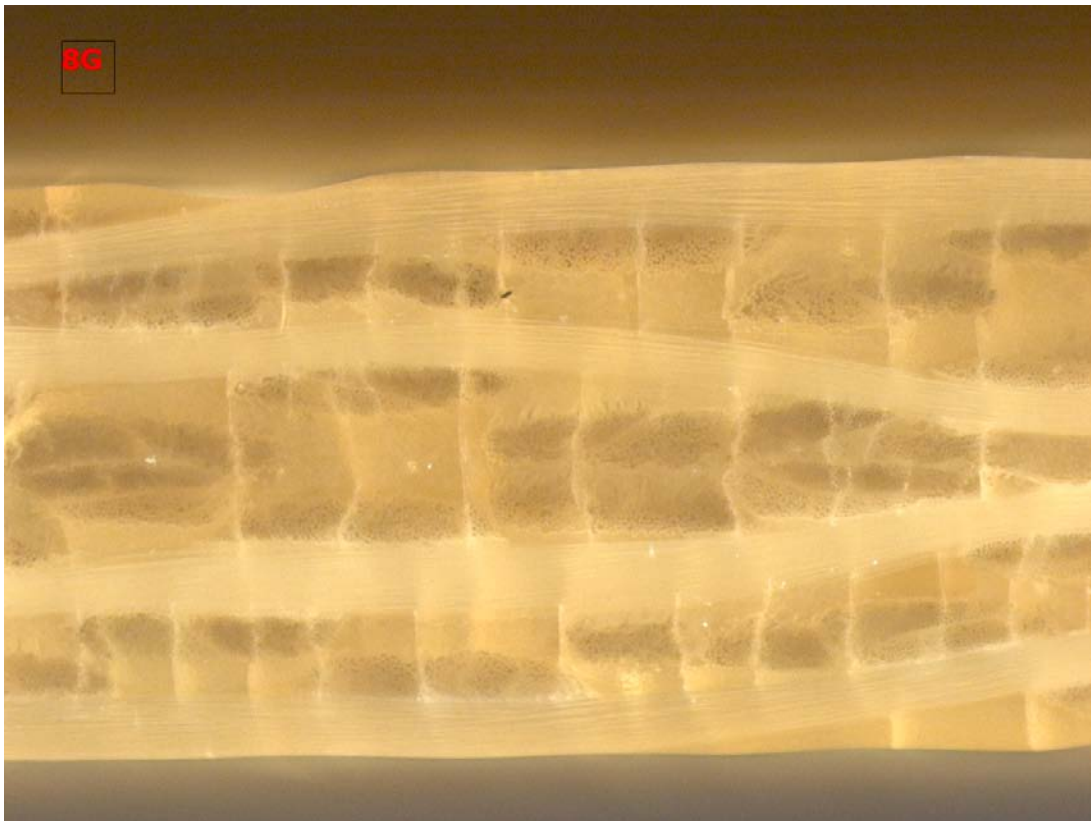


Figure 54. Vertical features of intact 8G at 60x

by using an SEM. The SEM images provided credible evidence that the vertical features were a by-product of the manufacturing process and not items of concern when determining and analyzing the failure mechanisms of each specimen.

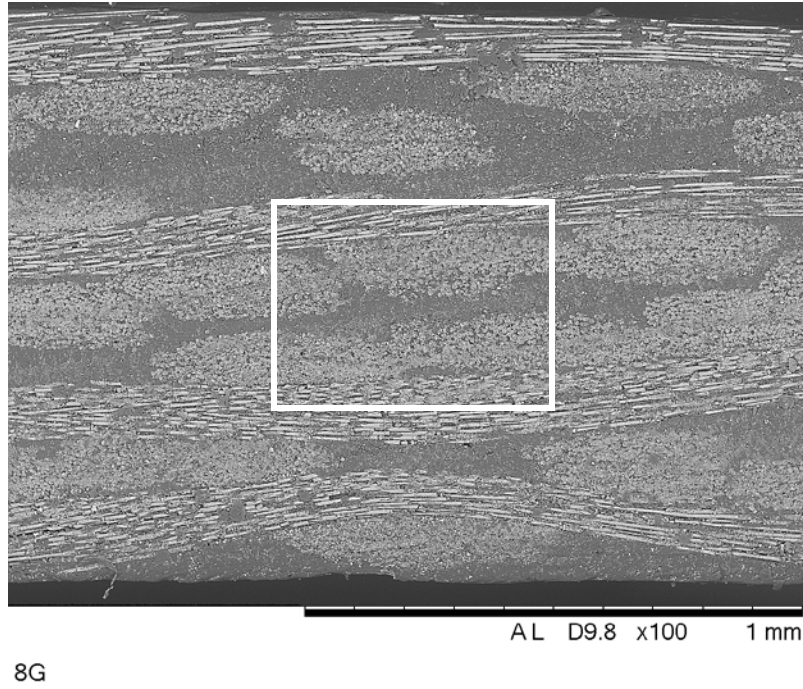


Figure 55. SEM image of intact 8G features at 100x

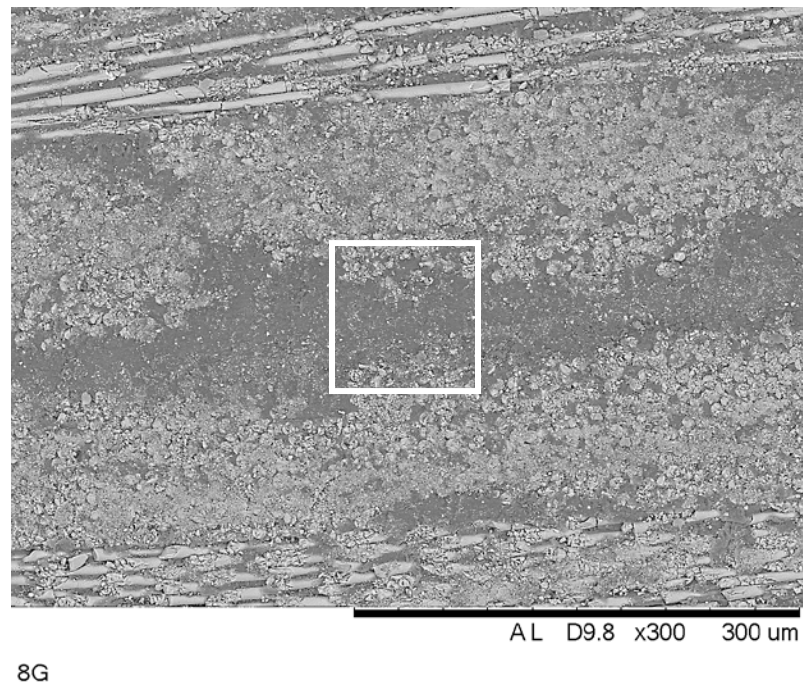
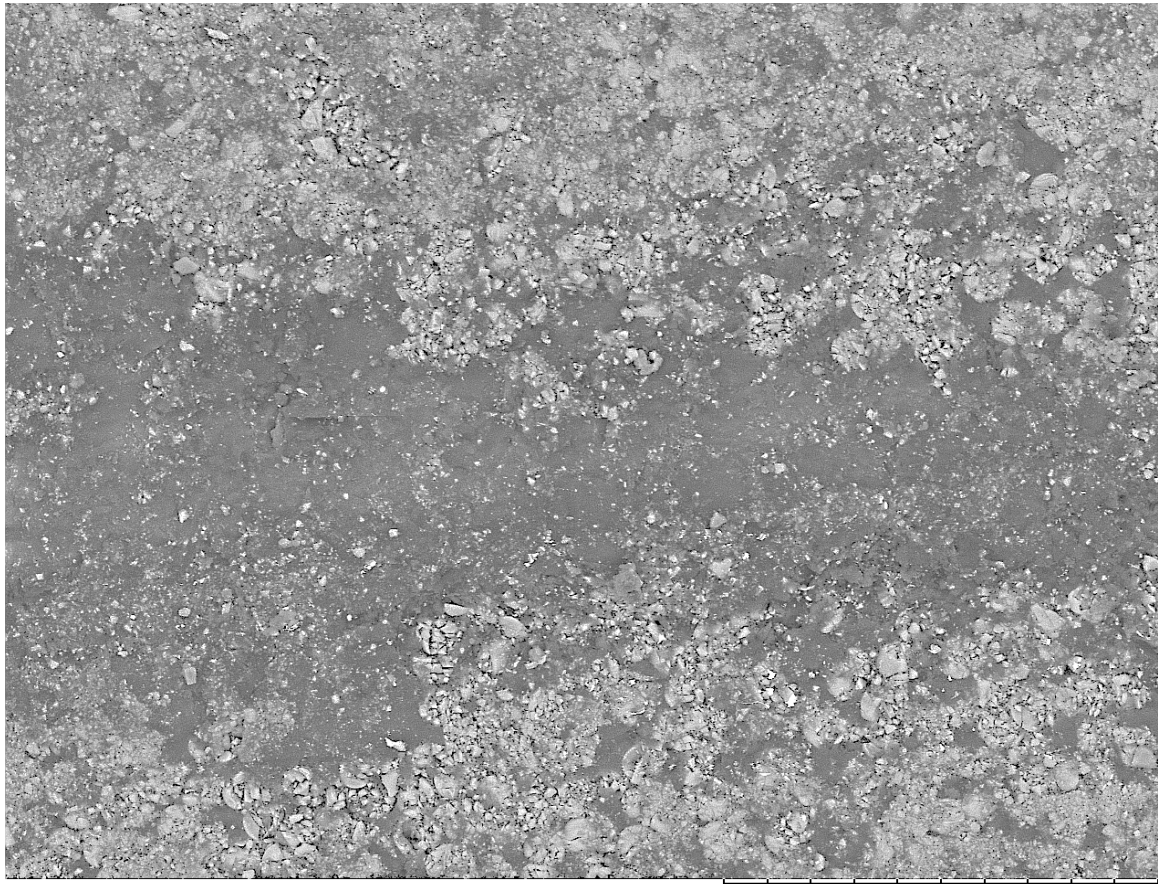


Figure 56. SEM image of intact 8G features at 300x: boxed region from Figure 55



AL D9.8 x600 100 um

8G

Figure 57. SEM image of intact 8G features at 600x: boxed region from Figure 56

V. Conclusions and Recommendations

This chapter presents a summary of the experiments performed for this study and the analysis of their results. Furthermore, the final conclusions of this study are expressed along with recommended topics for future studies.

5.1 Summary

The primary objective of this study was to characterize the EMI shielding properties of nanocomposites created with Cycom 5575-2 glass and MWNT plies while being subjected to monotonic tension tests and/or thermal cycling. The collected results would determine their ability to adequately defend against the wounding effects of EMI to the structural components of spacecraft. Employing these nanocomposites would radically downsize the dry weight of space vehicles while simultaneously eliminating the requirement to apply secondary EMI shielding materials. Reducing a spacecraft's dry weight and simplifying the manufacturing process both serve to drive down overall costs. Four distinct nanocomposite designs were tested for their EMI shielding properties before and after monotonic tension tests of increasing loads up to ultimate failure in order to ascertain the effects of tensile loading upon these four systems. In addition, these four nanocomposite designs were tested for their EMI shielding properties before and after thermal cycling. The four composite configurations are detailed in Figure 12 in section 3.2, and optical microscope images are provided in Figure 27 in section 4.1. All test equipment and procedures for this study are described in Chapter III.

5.2 Conclusions

The following conclusions are made from the analysis of the gathered results:

A. Effect of monotonic tensile loading on EMI SE

- The EMI SE behavior of the four specimens was moderately constant during the course of tensile loading increments up to ultimate failure. All three designs containing CNT plies experienced ~7% reduction in EMI SE performance for all methods of testing. The 2CNT/4G/2CNT specimens outperformed both the 4G/4CNT and (G/CNT)₄ designs and had an average EMI SE value of 73.19 times greater than the 8G (control) specimen. Of particular significance is that all three designs containing CNT plies did not demonstrate a catastrophic reduction in EMI SE performance post-fracture. The unaffected EMI SE behavior provides proof that the MWNTs remained intact after fracture and were able to provide continuing protection against EMI.

B. Effect of stacking sequence

- The best EMI SE performance belonged to the 2CNT/4G/2CNT design, which matches the results obtained from previous studies that found the exterior placement of conductive nanofibers as the most effective technique in shielding EMI.

C. Effect of thermal cycling on EMI SE

- The EMI SE behavior of the four specimens were extremely stable (3 ~ 7%) throughout the thermal cycling tests. The final recorded EMI

attenuation values for all four specimens were within 2% of the initial measurements taken prior to conducting the thermal cycling test sets.

D. Failure mechanisms

- The failure mechanisms for all four specimens were identical and not constrained to the stacking sequence. Transverse matrix cracks formed first leading to delamination, which then caused additional transverse matrix cracks. The compounding matrix cracks led to further delamination and fill strand debonding resulting in a significant reduction in strength and stiffness. An important observation made was that the CNT plies remained intact after fracture and the EMI SE measurements taken post-fracture verify that the MWNTs were undamaged.

5.2 Recommendations for Future Work

This research is a continuation of studies in the use of conductive nanocomposites for shielding against EMI. However, it is the first one to research the EMI shielding properties of nanocomposites created with Cycom 5575-2 glass and MWNT plies. In depth examination of these four systems should take place from initial failure to ultimate failure in order to fully comprehend the methods of stress transfer and failure progression. Measuring EMI attenuation levels while conducting fatigue testing would provide additional characterization for these four systems and could lead to design modification for improved performance. Constructing models that accurately predict the behavior of nanocomposites would provide a powerful tool in performing non-destructive evaluation, especially with the high cost associated with manufacturing nanocomposites.

Lastly, other nanofiber materials should be developed and researched for their potential use in EMI shielding and further applications.

Appendix A. EMI Shielding Theory

Electromagnetic waves incident upon a discontinuity will be partially reflected, and partly transmitted across the boundary and into the material (absorption). The effectiveness of the shielding material is the sum total of these two effects, plus a correction factor to account for reflections from the back surfaces of the shield. The overall expression for shielding effectiveness is written as:

$$S.E. = R + A + B \quad (1)$$

where

S.E. is the shielding effectiveness expressed in dB,

R is the reflection factor expressed in dB,

A is the absorption term expressed in dB, and

B is the correction factor due to reflections from the far boundary expressed in dB.

The reflection term is largely dependent upon the relative mismatch between the incoming wave and the surface impedance of the shield. Reflection terms and equations for electric, magnetic, and plane wave fields are given by the following expressions:

$$R_E = 353.6 + 10 \log_{10} \frac{Z_s}{Z_0} \quad (2)$$

$$R_H = 20 \log_{10} \left[\frac{Z_s}{Z_0} + 0.136r_1 \frac{Z_s}{Z_0} + 0.354 \right] \quad (3)$$

$$R_P = 108.2 + 10 \log_{10} \frac{Z_s}{Z_0} \quad (4)$$

where

R_E , R_H , and R_P are the reflection terms for the electric, magnetic, and plane wave fields expressed in dB.

G is the relative conductivity referred to copper,

f is the frequency in Hz,

μ_r is the relative permeability referred to free space,

r_1 is the distance from the source to the shield in inches.

The absorption term A is the same for all three waves and is given by the expression:

$$A = 3.338 \times 10^{-3} \times t \quad \text{---} \quad (5)$$

where

A is the absorption or penetration loss expressed in dB, and t is the thickness of the shield in mils.

The factor B can be mathematically positive or negative (in practice it is always negative), and becomes insignificant when $A > 6$ dB. It is usually only important when metals are thin, and at low frequencies (i.e., below approximately 20 kHz).

$$B \text{ (dB)} = 20 \log_{10} \quad \text{---} \quad (6)$$

where

A = absorption losses (dB)

$$= \quad = 1.3 \quad \text{---}$$

Z_S = shield impedance

Z_H = impedance of the incident magnetic field

Appendix B. Astroquartz II Glass Properties

Tensile Strength

Virgin Single Filament.....	6.0 GPa (870,000 PSI)
Impregnated Strand Tensile Test - ASTM D-2343 (on 20 end roving).....	3.6 GPa (530,000 PSI)
Young's Modulus.....	72 GPa (10 x 10 ⁶ PSI)
Poisson's Ratio.....	0.16
Density	2.2 g/cm ³
Silica Content (exclusive of yarn binder).....	99.99%

Mechanical

Density	2.2 g/cm ³ or 0.79lbm ³
Hardness (Mohs Scale).....	7

Electrical

Dielectric Constant (Dk)	
1 MHz.....	3.70
10 GHz.....	3.74
Dissipation Factor (Df)	
1 MHz	0.0001
10 GHz.....	0.0002

Thermal

Linear Expansion	
Coefficient kg.....	0.54 x 10 ⁻⁶
Specific Heat @ 20°C (J.kg -1k-1).....	7.5 x 10 ²
Heat conductivity @ 20°C (W.m-1.k-1).....	1.38
Strain Point (Log10 = 14.6).....	1070°C (1958°F)
Annealing Point (Log10n = 13).....	1220°C (2084°F)
Softening Point (Log10n = 7.6).....	1700°C (3092°F)

Optical

Refractive Index @ 15°C	1.4585
Dispersion.....	67
Field of Transparency (μm).....	0.2 to 4.0

Note: n=Viscosity in Poise

Bibliography

- [1] Aliev, A., Oh, Kozlov, Kuznetsov, Fang, Fonesca, Ovalle, Lima, Haque, Gartstein, Zhang, Zakhidov and Baughman. "Giant-Stroke Superelastic Carbon Nanotube Aerogel Muscles." *Science*, Vol. 323, No. 5921, pp. 1575-1578, Mar 2009.
- [2] Angelo, Joseph A. *Space Technology*, Greenwood Press, 88 Post Road West, Westport, CT 06881, 2003.
- [3] Ajayan, Pulickel M., Linda S. Schadler, Paul V. Braun. *Nanocomposite Science and Technology*, WILEY-VCH GmbH & Co. KGaA, Weinheim, 2003.
- [4] Banks, B. A., S. K. Rutledge, J. E. Merrow, and J. A. Brady, Atomic Oxygen Effects on Materials, *Proc. NASA/SDIO Joint Workshop on Space Environmental Effects*, Hampton, VA, 28-30 June, 1988.
- [5] Dzenis, Y. and Qian, J. "Analysis of Microdamage Evolution Histories in Composites," Faculty Publications from the Department of Engineering Mechanics, 2001.
- [6] Gay, Daniel, Suong V. Hoa, Stephen W. Tsai. *Composite Materials: Design and Applications*, CRC Press LLC, 2000 N. W. Corporate Blvd., Boca Raton, Florida 33431, 2003.
- [7] Harder, B. *Evaluation of Nanocomposites as Lightweight Electronic Enclosures for Satellites' Applications*. MS Thesis, AFIT/GMS/ENY/08-J01. Air Force Institute of Technology (AU), Wright-Patterson AFB OH, Jun 2008.
- [8] Hurang, Onyebueke, and Abatan. "Characterizing and Modeling Mechanical Properties of Nanocomposites- Review and Evaluation." *Journal of Minerals & Materials Characterization & Engineering*, Vol. 9, No. 4, pp.275-319, 2010.
- [9] JPS Composite Materials, URL: http://jpsglass.com/jps_databook.pdf [cited 31 August 2011].
- [10] Keydel, W. "Present and Future Airborne and Space-borne Systems," RTO-EN-SET-081, 2005.
- [11] Li, Q.F., Xu, Y., Yoon, J.S. "Dispersions of Carbon Nanotubes/Polyhedrol Oligomeric Silesquioxanes Hybrids in Polymer: The Mechanical, Electrical and EMI Shielding Properties." *Journal Material Science*, 46: 2324-2330, 2011.

- [12] Lyndon B. Johnson Space Center. "Understanding Space Radiation," FS-2002-10-080-JSC, October 2002.
- [13] Muolo, Michael J. *Space Handbook: A War Fighter's Guide to Space*, Air University Press, Maxwell Air Force Base, Alabama, Dec 1993.
- [14] Ning, L., Yi H., Feng D., Xiaobo H., Xiao L., Hongjun G., Yanfeng M., Feifei L., Yongsheng C., Eklund, P.C. *Nano Letters*, Vol. 6, No. 6, pp. 1141-1145, 2006.
- [15] Park, S.H., Theilmann, P.T., Asbeck, P.M., Bandaru, P.R. "Enhanced Electromagnetic Interference Shielding Through the Use of Functionalized Carbon-Nanotube-Reactive Polymer Composites." *Nanotechnology*, Vol. 9, Issue 4, pp. 464-469, July 2010.
- [16] Parker Chomerics: EMI Shielding and Thermal Management Solutions, URL: <http://www.chomerics.com/> [cited 31 August 2011].
- [17] Phillips, Alexander, Merryman and Gordon. "Effects of Outgassed Products from Spacecraft Materials on the Insulating Strength of the Space Vacuum," *Electrical Insulation and Dielectric Phenomena*, IEEE, pp.41-46, 1998.
- [18] Pilato, Louis A., Michael J. Michno. *Advanced Composite Materials*, Springer-Verlag Berlin Heidelberg, 1994.
- [19] Riga, Alan T., Lawrence Judovits. *Materials Characterization by Dynamic and Modulated Thermal Analytical Techniques*, AMERICAN SOCIETY FOR TESTING AND MATERIALS, West Conshohocken, PA, 2001.
- [20] Snedden, Robert. *Materials Technology*, Heinemann Library a Division of Reed Elsevier, Inc., Chicago, Illinois, 2001.
- [21] Tjong, Sie C. *Carbon Nanotube Reinforced Composites*, WILEY-VCH GmbH & Co. KGaA, Weinheim, 2009.
- [22] Yang, Y., Gupta, M.C., Dudley, K.L., Lawrence, R.W. "Electromagnetic interference shielding characteristics of carbon nanofiber-polymer composites." *Journal of Nanoscience and Nanotechnology*, Vol. 7, Issue 2, pp. 549-554, Feb 2007.

Vita

Lieutenant Commander Kenneth Y. Chong graduated from Falls Church High School in Falls Church, Virginia in June 1990. He enlisted upon graduating from high school and spent four years as a nuclear-trained electronics technician on a fast attack submarine. On July 1994, he entered undergraduate studies at the United States Naval Academy in Annapolis, Maryland where he received his commission and graduated with a Bachelor of Science degree in Nuclear Engineering in May 1998.

His first assignment commenced on August 2000 at Patrol Squadron FOUR SEVEN on Marine Corps Base Hawaii (MCBH), Oahu as an instructor Tactical Coordinator on the P-3C Orion. While assigned to Patrol Squadron FOUR SEVEN, he deployed overseas to both 5th and 7th FLEET Areas of Responsibility and conducted numerous missions in support of Operation Enduring Freedom. In September 2003, he was assigned to Commander, Patrol and Reconnaissance Force Pacific which later converted to Commander, Patrol and Reconnaissance Wing TWO where he served as a Weapons and Tactics Instructor and Officer-in-Charge of Wing TWO's Trainer Facility. In August 2006, he transferred to Fleet Support Unit TEN at Naval Air Station Whidbey Island, Washington where he served as a Tactics Officer and completed 58 combat sorties in support of Operation Iraqi Freedom. In August 2009, he entered the Graduate School of Engineering and Management, Air Force Institute of Technology. Upon graduation, he will be assigned as an acquisitions officer with the Air Force 303d Aeronautical Systems Group at Wright-Patterson AFB, Ohio.

REPORT DOCUMENTATION PAGE				Form Approved OMB No. 074-0188	
<p>The public reporting burden for this collection of information is estimated to average 1 hour per response, including the time for reviewing instructions, searching existing data sources, gathering and maintaining the data needed, and completing and reviewing the collection of information. Send comments regarding this burden estimate or any other aspect of the collection of information, including suggestions for reducing this burden to Department of Defense, Washington Headquarters Services, Directorate for Information Operations and Reports (0704-0188), 1215 Jefferson Davis Highway, Suite 1204, Arlington, VA 22202-4302. Respondents should be aware that notwithstanding any other provision of law, no person shall be subject to an penalty for failing to comply with a collection of information if it does not display a currently valid OMB control number.</p> <p>PLEASE DO NOT RETURN YOUR FORM TO THE ABOVE ADDRESS.</p>					
1. REPORT DATE (DD-MM-YYYY) 16-09-2011		2. REPORT TYPE Master's Thesis		3. DATES COVERED (From – To) Aug 2009 – Sep 2011	
4. TITLE AND SUBTITLE Evaluation of Nanocomposites for Shielding Electromagnetic Interference				5a. CONTRACT NUMBER	
				5b. GRANT NUMBER	
				5c. PROGRAM ELEMENT NUMBER	
6. AUTHOR(S) Chong, Kenneth Y., LCDR, USN				5d. PROJECT NUMBER	
				5e. TASK NUMBER	
				5f. WORK UNIT NUMBER	
7. PERFORMING ORGANIZATION NAMES(S) AND ADDRESS(S) Air Force Institute of Technology Graduate School of Engineering and Management (AFIT/EN) 2950 Hobson Way, Building 640 WPAFB OH 45433-8865				8. PERFORMING ORGANIZATION REPORT NUMBER AFIT/GAE/ENY/11-S01	
9. SPONSORING/MONITORING AGENCY NAME(S) AND ADDRESS(ES) Undisclosed sponsor				10. SPONSOR/MONITOR'S ACRONYM(S)	
				11. SPONSOR/MONITOR'S REPORT NUMBER(S)	
12. DISTRIBUTION/AVAILABILITY STATEMENT APPROVED FOR PUBLIC RELEASE; DISTRIBUTION UNLIMITED.					
13. SUPPLEMENTARY NOTES This material is declared a work of the U.S. Government and is not subject to copyright protection in the United States.					
14. ABSTRACT Numerous efforts are ongoing to research and develop nanocomposite materials for space applications. Current composite spacecraft materials are nonconductive and require costly shielding materials to be applied in order to protect spacecraft from the harmful effects caused by electromagnetic interference (EMI), which is a by-product of exposure to the space environment. Conductive fillers (nanofibers) are being employed in composites to produce nanocomposites to reduce the dry weight of space vehicles while providing sufficient protection against EMI. This eliminates the need to apply secondary shielding materials to spacecraft. This thesis studied a nanocomposite consisting of Cycom 5575-2 glass with multi-walled carbon nanotube (MWNT) plies. Four distinct configurations were tested for their EMI shielding effectiveness (SE) before and after thermal cycling and monotonic tension tests of increasing loads up to fracture. This study found that the EMI SE experienced minor reductions after thermal cycling and monotonic tensions tests, and failure mechanisms were consistent regardless of stacking sequence: transverse matrix cracks formed leading to delamination, which generated more matrix cracks and additional delamination resulting in ultimate failure. EMI SE measurements were performed post-fracture and demonstrated that the MWNTs remained intact and continued to provide sufficient EMI SE.					
15. SUBJECT TERMS nanocomposites, space environment protection, monotonic tension testing, thermal cycling, carbon nanotubes, multi-walled carbon nanotubes, electromagnetic interference protection					
16. SECURITY CLASSIFICATION OF:			17. LIMITATION OF ABSTRACT	18. NUMBER OF PAGES	19a. NAME OF RESPONSIBLE PERSON
a. REPORT	b. ABSTRACT	c. THIS PAGE			Shankar Mall, Ph.D.
U	U	U	UU	104	19b. TELEPHONE NUMBER (Include area code) (937) 255-3636, ext 4587 (shankar.mall@afit.edu)

